AN INVESTIGATION OF DUAL-BAND FABRY-PÉROT RESONANT CAVITY ANTENNAS

A Dissertation

Presented to

the Faculty of the Department of Electrical and Computer Engineering

University of Houston

In Partial Fulfillment

of the Requirements for the Degree

Doctor of Philosophy

in Electrical Engineering

by

Venkata Krishna Tulasi Kota

August 2016

AN INVESTIGATION OF DUAL-BAND FABRY-PÉROT RESONANT CAVITY ANTENNAS

Venkata Krishna Tulasi Kota

Approved:

Chair of the Committee
David R. Jackson, Professor,
Electrical and Computer Engineering

Committee Members:

Stuart A. Long, Professor,
Electrical and Computer Engineering

Donald R. Wilton, Professor,
Electrical and Computer Engineering

Lowell Wood, Professor,
Physics

Daniel Onofrei, Assistant Professor,
Mathematics

Suresh K. Khator, Associate Dean,
Cullen College of Engineering

Badrinath Roysam,
Professor and Chair,
Electrical and Computer Engineering

Acknowledgements

I would like to acknowledge and extend my heartfelt gratitude to my respected advisors, Dr. David R. Jackson and Dr. Stuart A. Long for their supervision, guidance and constant encouragement throughout my Ph. D. studies. I feel extremely fortunate for having had the opportunity to work with such eminent professors in the field of Applied Electromagnetics. Their invaluable inputs and contribution to this research work are greatly appreciated.

I would like to express my sincerest gratitude to Dr. Donald R. Wilton for patiently explaining any questions regarding the research. I am most appreciative for his time and cooperation. I would also like to thank the committee members of my dissertation, Dr. Lowell T. Wood and Dr. Daniel Onofrei for their helpful suggestions in shaping my dissertation.

Special thanks to Dr. Lotfollah Shafai (Distinguished Professor at the University of Manitoba) for so kindly agreeing to collaborate on this research project. His innovative ideas regarding the practical aspects of this work are most valued.

I would also like to thank my dear friends Dr. Sohini Sengupta, Xinyu Liu, Dr. Xiyao Xin, Mengna Yang and Nicholas Boggs for their unending support and insightful discussions related to the research.

Finally, I wish to thank my loving husband, parents, and parents-in-law. This academic journey would not have been possible without their moral support and cooperation. Words cannot express how tremendously grateful I am for their endless encouragement through all my endeavors.

AN INVESTIGATION OF DUAL-BAND FABRY-PÉROT RESONANT CAVITY ANTENNAS

An Abstract

of a

Dissertation

Presented to

the Faculty of the Department of Electrical and Computer Engineering

University of Houston

In Partial Fulfillment

of the Requirements for the Degree

Doctor of Philosophy

in Electrical Engineering

by

Venkata Krishna Tulasi Kota

August 2016

Abstract

In this dissertation, we examine a dual-band version of the Fabry-Pérot resonant cavity antenna that uses a frequency selective surface (FSS) patch layer over a ground plane to form a composite artificial ground plane that replaces the single metal ground plane of the conventional structure. The structure thus consists of an upper cavity region (between the FSS and the partially reflective surface, also known as the PRS) and a lower cavity region (between the ground plane and the FSS).

The conventional single-cavity Fabry-Pérot antenna is studied first, and the theory is then extended to the proposed dual-band structure. The 2-D arrays of metal patches that form the FSS and PRS layers in the proposed dual-band design are first considered to be suspended in air for simplicity. An iterative design procedure is given that determines the optimum resonance frequency of the PRS periodic structure as well as the optimum location of the FSS layer within the composite cavity and the optimum source locations. The PRS and FSS are then placed on 60 mil thick Arlon Diclad 527 boards and the structure is once again optimized for dual-band behavior.

The study is further extended to a practical truncated Fabry-Pérot antenna of size 6 in × 6 in. Results for this practical dual-band structure are shown and these results are compared with those obtained using the commercial simulation software Ansys Designer.

Table of Contents

List of Figures

List of Tables

Chapter 1

Introduction

1.1 Background

Leaky-wave antennas (LWAs) come under the category of traveling-wave antennas [1], [2] and have the ability to easily produce highly-directive beams [3]. Two common types are often seen in the literature. One is the uniform open waveguide structure, which radiates by virtue of the fact that the structure supports a fast wave. The other type uses a periodic structure so that radiation occurs from the $n = -1$ space harmonic (Floquet mode) [4]. Along with the distinction of either being uniform or periodic, these antennas can also be classified into two different categories based on their geometry. The first category is one-dimensional (1-D) leaky-wave antennas while the second is two-dimensional (2-D) leaky-wave antennas.

A 1-D leaky-wave antenna has a guiding structure which supports a wave traveling in a fixed direction [5]. These antennas can produce a conical or fan beam that is scannable with frequency. An array of such antennas is needed to produce a pencil beam [4]. An alternative method to produce a pencil beam is to use a 2-D LWA, in which the radiating cylindrical leaky wave propagates outward radially along a surface from the point of excitation [6]. One example of a 2-D LWA that is based on planar technology and offers a simply way to obtain high directivity with a small source is the Fabry-Pérot resonant cavity antenna, and will be studied in this dissertation.

1.2 The Fabry-Pérot Resonant Cavity Antenna

The Fabry-Pérot resonant cavity antenna (FPCA) is a type of two-dimensional (2-D) leaky-wave antenna that uses a radially-propagating leaky wave on a guiding structure as the main radiating mechanism to form the beam. Either pencil beams at broadside or conical beams may be produced, with broadside beams being the most common. The structure consists of a partially reflecting surface (PRS) over a ground plane, with a possible substrate between. The PRS is often in the form of a periodic frequency selective surface (FSS), such as a 2-D periodic array of metal patches or slots in a conducting plane. This structure however, operates as a quasi-uniform LWA rather than a periodic LWA since radiation occurs from the fundamental $(n = 0)$ space harmonic of the radially-propagating parallel-plate waveguide leaky mode [7]. Today, the structure goes by several different names, such as Fabry-Pérot resonant cavity antenna, EBG antenna and 2-D leaky wave antenna.

The first Fabry-Pérot resonant cavity antenna structure was introduced by von Trentini in 1956 [8] and consisted of a source on a ground plane with a PRS parallel to the ground plane at a distance l in front of it. In this structure, multiple reflections with decreasing amplitudes were introduced between the PRS and ground plane, and an expression for the resonance condition that yielded maximum radiated power at broadside was derived. The PRS consisted of an array of closely spaced parallel conducting wires oriented parallel to the electric field.

In [9], an improved version of the von Trentini antenna was developed using an optimized PRS in front of a waveguide aperture in a ground plane. The phase of the optimized PRS phase linearly increased with frequency leading to wideband performance of the antenna. Various PRSs loaded with several different element geometries, such as dipoles, crossed dipoles, patches, rings, and square loops were investigated. It was found that dipoles and square or circular patches (or their complementary structures) produced less variation of the beam with frequency as opposed to using cross-dipoles, square-loops, and rings where this slow variation was not found, even if the elements were packed closely together. For this reason, dipoles were chosen to be the preferred element for the PRS.

There have been recent advances in the study of these structures. Such advances include bandwidth enhancement for broadside applications, making the structure thinner, and multiband operation.

1.2.1 Bandwidth Enhancement

As mentioned, there have been recent advances in the area of bandwidth enhancement of these structures. Often, the bandwidth enhancement is achieved by use of a multilayer PRS structure [10]. For broadside optimization, the phase of the reflection coefficient should increase linearly with frequency to ensure high bandwidth [11].

In [10], a 2-D leaky wave antenna with a PRS consisting of two capacitive arrays of metallic square patches with dissimilar dimensions was used in order to achieve the resonance condition over a wide frequency range. The top array of square patches was of smaller dimension when compared to the bottom array. A parametric study was performed in terms of the size of the patches of both PRSs, and after optimization of the double-layer PRS, a 3 dB bandwidth of about 5.5% was obtained.

In [12], an EBG structure with a defect composed of two double-layer FSSs with a wavelength spacing between them was used. Due to the presence of the defect, an allowed frequency band was created within the EBG band gap. A resonator was formed between the double-layer FSS and a metallic ground, and the bandwidth was found to significantly improve.

Another method for bandwidth enhancement was studied in [13], where the PRS consisted of two metallic layers of orthogonal strips etched on PCB surfaces and was placed about a half-wavelength above a ground plane. Experimental results showed that bandwidth enhancement was obtained with comparison to a conventional one-layer PRS antenna. The 3-dB bandwidth was found to increase from 6.2% to 12.3% compared with a single-layer PRS, for the same gain. Other novel methods for bandwidth enhancement can be seen in [14]-[18].

1.2.2 Low Profile Antennas

Another popular area of study is low profile Fabry-Pérot resonant cavity antenna structures. In [19]-[21], a novel high gain antenna was presented which utilized an artificial magnetic conductor (AMC) ground plane instead of a conventional PEC ground plane to reduce the antenna profile. It was found that the resonance condition changed due to the presence of the AMC ground plane, and the thickness of the cavity was reduced to approximately half of the original value.

In [22], a subwavelength metamaterial-based resonant cavity antenna was presented. The cavity antenna was formed by a PEC ground plane and a metasurface PRS composed simultaneously of an inductive and capacitive grid. The antenna was feed by a 2×2 microstrip patch array acting as a multi-source. It was found that the multi-source fed cavity was highly directive with low sidelobe levels. Other metamaterial-based resonant cavity antennas are seen in [23]-[29].

To overcome the relative difficulty in integrating a patch antenna feed with an AMC on the same side of the substrate as seen in [19], a low-profile Fabry-Pérot resonant cavity antenna covered with a double-layered partially reflecting surface (PRS) and an easily integrated patch antenna feed was presented in [30]. This Fabry-Pérot resonant cavity antenna with a double-layered PRS was found to exhibit high gain and was much smaller than the cavity antenna of [19].

In [31], an ultrathin and high-gain resonant cavity antenna was studied. The structure was compared to the metamaterial based Fabry-Pérot structures of [21], [24], and [32], and it was shown that the presented structure had the advantage of being simple as the substrate of the feeding patch did not require a high impedance surface or artificial magnetic conductors. The controllable cavity thickness was realized by means of tuning the phase of the PRS. Other low profile FPCA structures are seen in [33]-[35].

1.2.3 Multiband Performance

Along with bandwidth enhancement and low profile antennas, there have also been recent advances in the area of multiband operation which is the research focus of this dissertation. In [36], a dual-band Fabry-Pérot resonant cavity antenna constructed from a double-layer partially reflective surface suspended above a metallic ground plane was presented. The structure formed two Fabry-Pérot cavities corresponding to two different resonance frequencies.

A simple dual-band Fabry-Pérot resonant cavity antenna consisting of an EBG superstrate structure formed using two plain unprinted identical slabs was studied in [37]. Using the secondary cavity formed between the two dielectric slabs, the gradient of the reflection phase versus frequency curve was engineered to satisfy the necessary conditions of directivity enhancement in two frequency bands. A method to obtain dual-band behavior with a small frequency separation ratio was proposed in [38], where the antenna consisted of a PRS superstrate and an artificial magnetic conductor ground plane.

In [39] a novel highly directive and dual-band low profile FPCA was proposed. The PRS of the FPCA structure was formed by a single substrate with double-sided metallization, unlike other structures which used two interleaved cavities where each one is tuned for its frequency. A few models tuned for Ka-band satellite frequencies, with different amplitude reflection responses, were presented, and a prototype was manufactured.

In [40], a PRS that can form a tri-band Fabry-Pérot cavity was proposed that provides strong reflections at the first and third frequency bands, resulting in the high gain at the first and third band and an appropriate gain level at the second band. The proposed PRS was a single dielectric layer coated with two identical periodic slot arrays on its two surfaces. Other dual-band and tri-band models can be seen in [41]-[43].

1.3 Dissertation Outline

This dissertation examines a dual-band version of the Fabry-Pérot resonant cavity antenna. The structure uses an FSS layer to form an equivalent reactive ground plane that replaces the single metal ground plane in its conventional counterpart.

In Chapter 2, we analyze an air-filled Fabry-Pérot resonant single cavity antenna. An overview of calculating the far-field using reciprocity and the Transverse Equivalent Network (TEN) is provided and the calculation of the shunt susceptances modelling the FSS layers is explained in detail using the Method of Moments (MoM). The antenna structure is then extended to a case where the PRS layer is placed on a substrate board, and the structure is again analyzed. The E-plane radiation patterns obtained using the spectral domain periodic moment method and the TEN model are presented for both the air-filled case as well as the substrate-board case.

In Chapter 3, we propose a dual-band version of the Fabry-Pérot resonant cavity antenna. A completely air-filled cavity dual-band design is first presented, and a systematic procedure to obtain dual-band behavior is explained. An iterative method to obtain optimum beam shapes and equal directivities at the two specified design frequencies is provided. The dual-band structure is then extended to one where the PRS and FSS layers are placed on substrate boards, and an optimized dual-band design is again obtained using the proposed iterative method.

In Chapter 4, a truncated model of the air-filled optimized dual-band design presented in Chapter 3 is analyzed using Ansys Designer. A study on patch length and broadside directivity is presented and a hybrid model is proposed. A truncated version of the optimized substrate-board design of Chapter 3 is also analyzed, and the results are presented.

In Chapter 5, we conclude the results presented in this dissertation. A brief description of possible future work is also included.

Chapter 2

Single Cavity Fabry-Pérot Resonant Cavity Antenna

The work presented in this chapter focuses on the analysis of an air-filled Fabry-Pérot single cavity antenna with a 2-D periodic array of metal patches as the PRS and a horizontal electric dipole as the source of excitation. Reciprocity along with a periodic spectral-domain moment method is used to calculate the far-field radiation characteristics. The antenna structure is then extended to a practical case, in which a substrate board is introduced as the support on which the periodic arrays of patches lie. The entire theory presented here is the basis for our proposed dual-band model that is introduced in Chapter 3.

We begin this chapter by introducing the Fabry-Pérot resonant single cavity antenna geometry in Section 2.1. Section 2.2 explains the calculation of the far-field using reciprocity and the spectral-domain periodic moment method. The Transverse Equivalent Network model (TEN) and the extraction of the shunt susceptance value modelling the PRS layer in the TEN model are also explained in this section. The E-plane radiation patterns of the antenna obtained from the spectral-domain periodic moment method and the TEN model are then provided. In Section 2.3, the antenna structure is reanalyzed with the introduction of a substrate board, and the resultant E-plane radiation patterns are provided. Section 2.4 provides conclusions for the entire analysis.

2.1 Introduction

As introduced in Chapter 1, Fabry-Pérot Cavity Antennas (FPCAs) are a class of 2-D leaky-wave antennas (LWAs), and are a promising solution to produce highly directive radiation from simple sources embedded in planar, partially open structures [44]. A top view as well as side view of a single cavity Fabry-Pérot cavity antenna is shown in Figure 2.1.

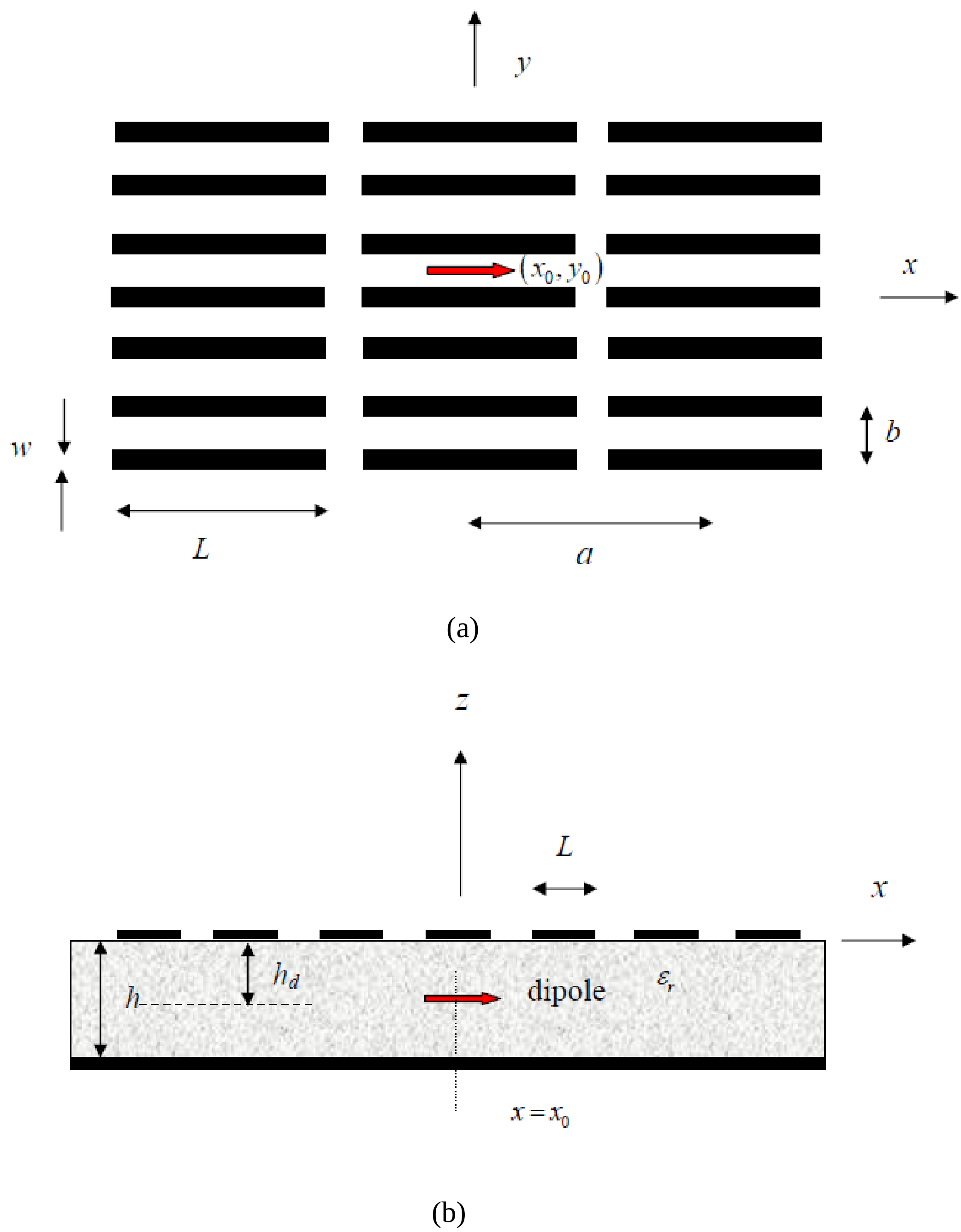

Figure 2.1. Geometry of a single cavity Fabry-Pérot cavity antenna (a) Top view (b) Side view [45].

Different types of partially-reflecting surfaces (PRSs) are seen in the literature [46]–[48]. As shown in Figure 2.1 (a), the PRS chosen for our design consists of a 2-D array of metal patches of a given length, width, and periodicity. The source of excitation is considered to be a horizontal infinitesimal electric dipole at (x_0, y_0, z_0) inside the grounded substrate of height h, as seen in Figure 2.1 (b). In our study, we shall consider the cavity region to be air.

2.2 Single Cavity: Air Case Design

2.2.1 Calculation of the Far-Field: Reciprocity

Reciprocity is used to calculate the far-field pattern. Figure 2.2 shows how reciprocity is applied.

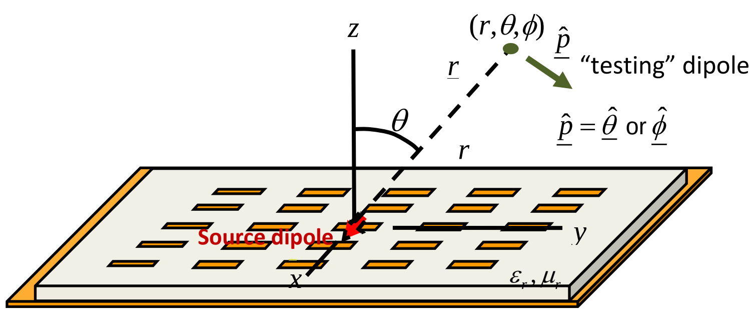

Figure 2.2. The geometry for the reciprocity calculation of the far-field of the Fabry-Pérot resonant cavity antenna, showing a testing dipole in the far field.

A "testing" dipole is placed at the observation point in the far-field in order to sample the electric field there. In Figure 2.2, the testing dipole is shown to be in the $\underline{\hat{p}}$ direction, where $\underline{\hat{p}}$ may be either $\underline{\hat{\theta}}$ or $\underline{\hat{\phi}}$, corresponding to TM_z or TE_z incidence, respectively. By reciprocity, the far-field at the observation point is equated to the field at the original dipole source location due to an incident wave emanating from the “testing” dipole, which is essentially a plane wave near the location of the source dipole [45]. Therefore, we may write

$$E^{inc}\left(\underline{r}\right) = E_0\, e^{j\left(k_x x + k_y y + k_z z\right)}, \tag{2.1}$$

where

$$E_0 = \left(\frac{-j\omega\mu_0}{4\pi r}\right) e^{-jk_0 r} \ . \tag{2.2}$$

From reciprocity,

$$\langle a,b\rangle = \langle b,a\rangle \ . \tag{2.3}$$

Hence,

$$E_p^{FF}\left(\underline{r}\right) = E_0 E_x^{PW}\left(\underline{r}_0\right) \ , \tag{2.4}$$

where

$E_p^{FF}\left(\underline{r}_0\right) =$ far-field at the observation point,

$E_x^{PW}\left(\underline{r}_0\right) = E_x$ field of unit-amplitude incident plane wave $\underline{E}^{inc}$ polarized in $\underline{\hat{p}}$ direction.

Therefore, the far-field pattern calculation reduces to a calculation of the field inside the substrate due to a plane-wave incidence [50].

2.2.2 Transverse Equivalent Network (TEN) Model

A simple transverse equivalent network (TEN) model is used to calculate the field E_x^{PW} inside the antenna due to a plane-wave incidence. Here, the field E_x^{PW} of the (0,0) Floquet harmonic inside the substrate due to plane wave incidence is calculated by finding the voltage on an equivalent transmission-line model, where voltage represents the transverse electric field. As previously mentioned, when the testing dipole is in the $\underline{\hat{\theta}}$ direction, we consider TM_z incidence and the incident voltage is given by

$$V^{inc} = E_x^{inc} = E_0 \cos\theta \cos\phi \ . \tag{2.5}$$

Similarly, when the testing dipole is in the $\underline{\hat{\phi}}$ direction, we have TE_z incidence, and the incident voltage is

$$V^{inc} = E_x^{inc} = E_0 \left(-\sin\phi\right) \ . \tag{2.6}$$

The general structure of a Fabry-Pérot resonant cavity antenna and its TEN model are given in Figure 2.3.

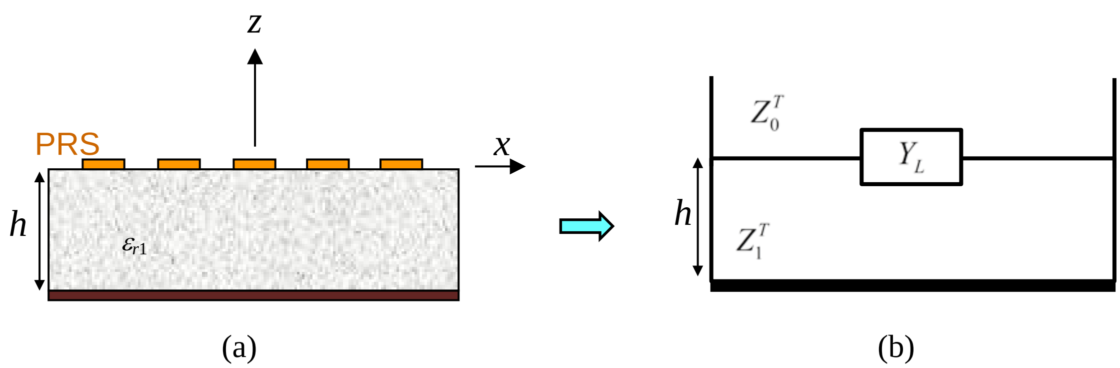

Figure 2.3. (a) The general structure of a Fabry-Pérot resonant cavity antenna and (b) its Transverse Equivalent Network (TEN) model.

In the TEN of Figure 2.3, a shunt load admittance Y_L is used to represent the 2-D periodic array of metal patches of the PRS above the grounded substrate. The superscript T denotes either TM or TE. The characteristic impedance of the substrate layer is given by

$$Z_1^{TM} = \frac{k_{z1}}{\omega\varepsilon_1} \tag{2.7}$$

and

$$Z_1^{TE} = \frac{\omega\mu_1}{k_{z1}} \ . \tag{2.8}$$

In our case, we will take the cavity region to be air.

2.2.3 Calculation of PRS Shunt Susceptance using Method of Moments

As previously mentioned, the PRS layer is modeled as a shunt load admittance Y_L in the TEN model. This admittance is calculated using a periodic spectral-domain Method of Moments (MoM). To perform this calculation, let us consider a single layer cavity with a given periodic patch screen as the PRS. First, the height of the cavity is elongated and made to be equal to an odd multiple of a quarter wavelengths. The cavity is made long enough to ensure the presence of the (0,0) Floquet mode only and to avoid contamination from higher-order modes at the source location. The source dipole is then placed at distance that is a multiple number of full wavelengths from the PRS. The elongated structure with a PRS, along with its TEN model, is shown in Figure 2.4.

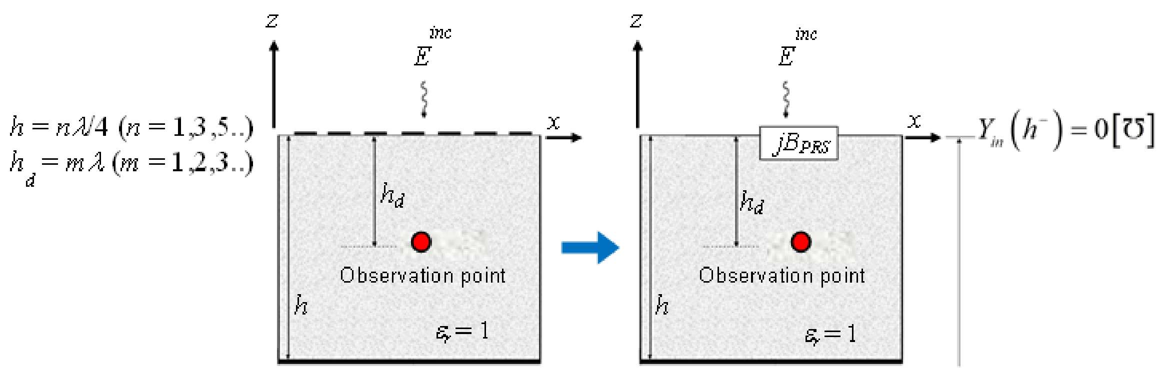

Figure 2.4. The elongated structure with a PRS (left), and its TEN model (right).

Since the screen is lossless, the load admittance of the PRS is pure imaginary, $Y_{PRS} = jB_{PRS}$. Since the cavity height is an odd multiple of a quarter wavelength, an input admittance $Y_{in}=0$ is observed at $z=h^{-}$ when looking down from the ground plane, which is modeled as a short circuit in the TEN. Hence the total load admittance at $z=0$ is Y_{PRS} only. Hence, if a plane wave incidence $E_x^{inc}=1\,[\mathrm{V/m}]$ is considered on the PRS, then the voltage obtained at the source dipole location in the TEN model is essentially the electric field E_x there. The voltage across the total load (which is just Y_{PRS} here) at $z=0$ is

$$V(0)=V^{inc}(1+\Gamma_L)\ , \tag{2.9}$$

where

$$\Gamma_L=\frac{Y_0-Y_L}{Y_0+Y_L};\quad Y_L=jB_{PRS},\ Y_0=\frac{1}{\eta_0}\ . \tag{2.10}$$

Since complex voltage repeats every complete wavelength, the voltage at the source dipole location is equal to that at $z=0$. Hence, we have

$$V_{obs}=V(-h_d)=V(0)=V^{inc}(1+\Gamma_L)\ . \tag{2.11}$$

From the above equation we may find the value of the susceptance B_{PRS},

$$B_{PRS}=\frac{Y_0(2-V_{obs}/V_{inc})}{jV_{obs}/V_{inc}}\ . \tag{2.12}$$

This gives us

$$B_{PRS}=\frac{Y_0\left(2-E_x^{(0,0)}(-h_d)/E^{inc}\right)}{jE_x^{(0,0)}(-h_d)/E^{inc}}\ , \tag{2.13}$$

where $E_x^{(0,0)}(-h_d)$ is the field at the source dipole location and is found as explained in the next section [50].

2.2.4 The Spectral-Domain Periodic Moment Method

A periodic spectral-domain moment method is used to calculate the field inside the substrate due to a plane-wave incidence. The total electric field inside the cavity due to a plane-wave incidence is expressed as the sum of a "layer" field and a "scattered" field, as

$$\underline{E}^{tot} = \underline{E}^{layer} + \underline{E}^{sca} . \tag{2.14}$$

The layer field is that which would exist without the metal patches, and accounts only for the reflection from the layered structure. The scattered field is due to the currents on the metal patches. The x-component of the layer field is

$$\underline{E}_x^{layer} = \underline{E}_x^{inc} \left(1+\Gamma\right) , \tag{2.15}$$

where the incident plane-wave field from the testing dipole is given in (2.1). The reflection coefficient Γ is calculated at the top of the layered structure, in the absence of the patches. The scattered field is given by

$$E_x^{sca} = \frac{1}{ab} \sum_{p=-\infty}^{\infty} \sum_{q=-\infty}^{\infty} \tilde{G}_{xx}\left(k_{xp}, k_{yq}\right) \cdot \tilde{J}_{sx}\left(k_{xp}, k_{yq}\right) \cdot e^{-j\left(k_{xp}x + k_{yq}y\right)} , \tag{2.16}$$

where G_{xx} is the xx component of the spectral-domain Green's function. The electric field integral equation (EFIE) on the (0,0) dipole requires that

$$\underline{E}^{tot} = \underline{E}^{layer} + \underline{E}^{sca} = 0 . \tag{2.17}$$

Galerkin's method is used to enforce the EFIE to find the unknown current distribution on the surface of the (0,0) patch. The basis functions are chosen as

$$J_{sx}\left(x,y\right) = \sum_{n=1}^{N} A_n \cdot B_n\left(x,y\right) = \sum_{n=1}^{N} A_n \cdot \frac{1/\pi}{\sqrt{\left(\frac{w}{2}\right)^2 - y^2}} \cdot \sin\left[\frac{n\pi}{L}\left(x + \frac{L}{2}\right)\right] . \tag{2.18}$$

The Fourier transform of the patch current in (2.18) is

$$
\begin{aligned}
\tilde{J}_{sx} &= \int_{-L/2}^{L/2}\int_{-w/2}^{w/2} J_{sx}(x,y)\, e^{j(k_x x + k_y y)} dxdy \\
&= \sum_{n=1}^{N} A_n \tilde{B}_n\left(k_x, k_y\right) \\
&= \sum_{n=1}^{N} A_n \tilde{f}_n(k_x)\, \tilde{g}\left(k_y\right),
\end{aligned}
\tag{2.19}
$$

where

$$
\tilde{g}\left(k_y\right) = J_0\left(k_y \frac{w}{2}\right), \tag{2.20}
$$

and

$$
\tilde{f}_n(k_x) = \frac{e^{-j(k_x L/2)}\left[-n\pi L + e^{jk_x L} L\left(n\pi \cos(n\pi)\right)\right]}{\left(k_x L\right)^2 - \left(n\pi\right)^2} \ . \tag{2.21}
$$

The matrix form of the discretized EFIE has the form

$$
\left[Z_{mn}\right]\left[A_n\right] = \left[R_m\right], \tag{2.22}
$$

where the right-hand side terms are given by

$$
R_m = -E_x^{inc}(0,0,0)(1+\Gamma)\, \tilde{B}_m\left(-k_{x0}, -k_{y0}\right) \tag{2.23}
$$

and

$$
Z_{mn} = \frac{1}{ab} \sum_{p=-\infty}^{\infty} \sum_{q=-\infty}^{\infty} \tilde{G}_{xx}\left(k_{xp}, k_{yq}\right) \tilde{B}_n\left(k_{xp}, k_{yq}\right) \tilde{B}_m\left(-k_{xp}, -k_{yq}\right) \ . \tag{2.24}
$$

After the coefficients $\left[A_n\right]$ for the current amplitudes are obtained by solving Equation (2.22), the field E_x at the source location $\left(x_0, y_0, -h_d\right)$ can be determined as

$$E_x\left(x_0, y_0, -h_d\right) = E_x^{inc}\left(1+\Gamma\right)\left[\frac{\sin\left(k_{z1}^{pw}\left(h-h_d\right)\right)}{\sin\left(k_{z1}^{pw}h\right)}\right]$$
$$+\frac{1}{ab}\sum_{n=1}^{N}A_n\sum_{p=-\infty}^{\infty}\sum_{q=-\infty}^{\infty}\tilde{G}_{xx}\left(k_{xp}, k_{yq}, -h_d\right)\cdot\tilde{B}_n\left(k_{xp}, k_{yq}\right)e^{-j\left(k_{xp}x_0+k_{yq}y_0\right)}. \tag{2.25}$$

Hence, from (2.25) we may find $E_x^{(0,0)}\left(0,0,-h_d\right)$ (which is the same as $E_x^{(0,0)}\left(-h_d\right)$) in (2.13). The spectral-domain Green's function $\tilde{G}_{xx}$ of Equation (2.16) is provided in the Appendix.

2.2.5 Calculation of Cavity Heights Using TRE

In order to calculate the cavity height, the Transverse Resonance Equation (TRE) is used. The process of calculating the cavity height is shown in Figure 2.5.

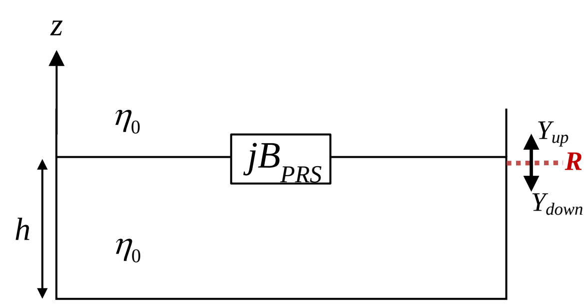

Figure 2.5. The TEN model for calculation of cavity height.

Considering the location of the PRS for our reference plane, and working with the imaginary part and ignoring the real part of the admittance for the purposes of using the TRE to calculate the resonance condition, we have

$$\mathrm{Im}\left(Y_{up}\right) = -\,\mathrm{Im}\left(Y_{down}\right). \tag{2.26}$$

From this equation we may obtain the cavity height *h*. The equation for obtaining the height of a cavity is given as

$$h = \frac{1}{k_0}\cot^{-1}\left(\eta_0 B_{PRS}\right) \ . \tag{2.27}$$

During the process of calculating the cavity height, a half-wavelength at the particular frequency of operation is added in order to avoid having the ground plane and PRS layer from being too close to one another, and hence avoiding higher-order Floquet mode interaction within the cavity.

2.2.6 Comparison of E-plane Radiation Patterns

We shall compare the E-plane patterns at 12 GHz and 18 GHz, using two different methods: the reciprocity/spectral-domain periodic moment method and the TEN network model. The frequencies of 12 GHz and 18 GHz are specifically chosen as they are the design frequencies of the dual-band Fabry-Pérot resonant cavity antenna discussed in Chapter 3. Figure 2.6 shows a comparison of the E-plane patterns at 12 GHz using the two methods for the single cavity FPCA structure. Here, the 2-D patch array dimensions are L = 1.25 cm, W = 0.1 cm, a = 1.35 cm and b = 0.3 cm. The air has a relative permittivity ε_r = 1 and the cavity height is $h = 1.333$ cm. The source dipole location is $h_d = h/2$ (the source dipole is in the middle of the substrate). The E-plane is defined along $\phi = 0^\circ$.

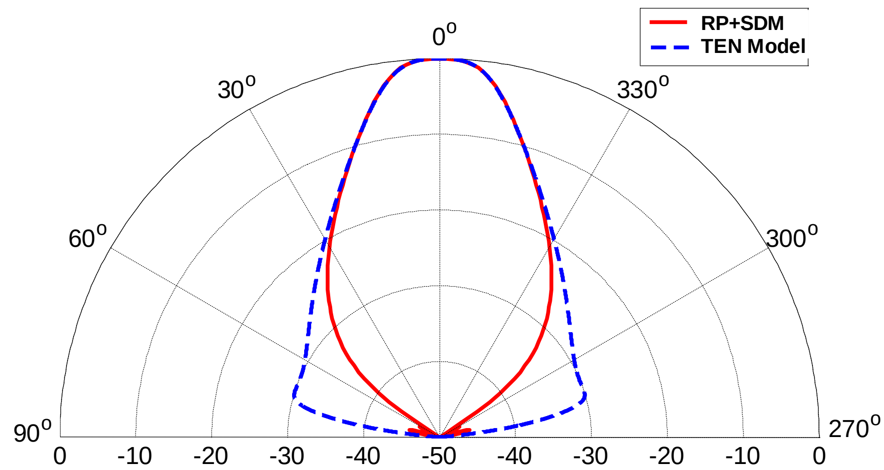

Figure 2.6. A comparison of the E-plane radiation patterns at 12 GHz by using two different methods: the reciprocity/spectral-domain periodic moment method and the TEN network model.

From Figure 2.6 we may see that the two patterns are in good agreement up to $\theta = 30^\circ$ (on either side) from broadside.

Figure 2.7 shows a comparison of the E-plane patterns for the same structure at 18 GHz. Here the cavity height is $h = 0.841\,\text{cm}$.

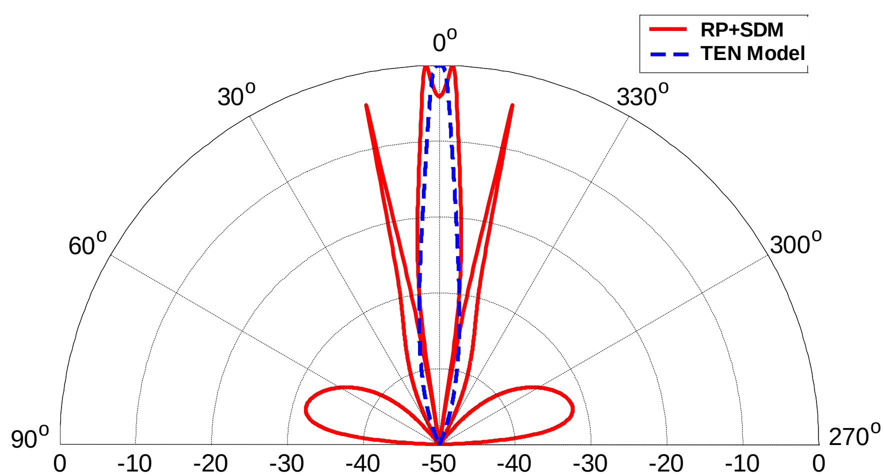

Figure 2.7. A comparison of the E-plane radiation patterns at 18 GHz by using two different methods: the reciprocity/spectral-domain periodic moment method and the TEN network model.

From Figure 2.7, we observe that the main beam of the E-plane radiation pattern obtained from the spectral domain periodic moment method is not in agreement with that of the pattern obtained from the TEN model. This is because at 18 GHz we are approaching the resonance frequency of the PRS layer (which was found to be 19 GHz). Due to this, sensitivity issues arise, as the PRS is approaching a short circuit, and the higher-order Floquet modes create disturbances (though they are not propagating) within the cavity. We may overcome this issue by adding an extra half-wavelength at 18 GHz to the air cavity. Figure 2.8 shows the E-plane radiation patterns when an extra half-wavelength at 18 GHz is added to the cavity height for either model. The cavity height is now $h = 1.673$ cm and $h_d = h/4$.

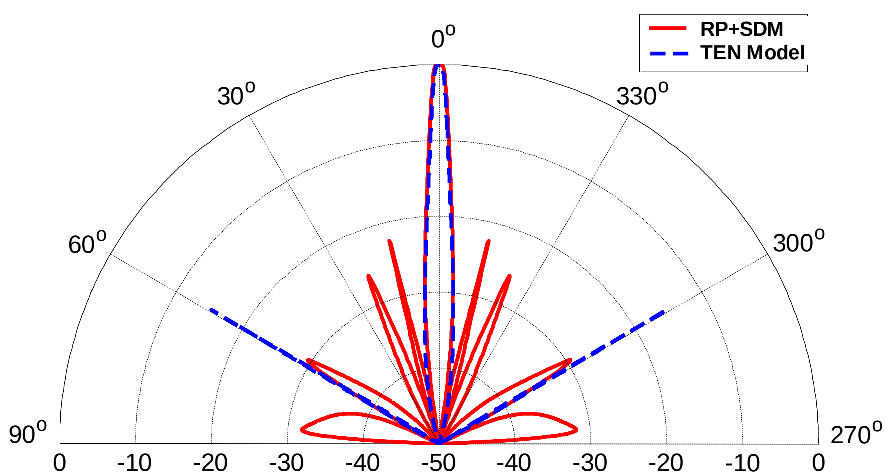

Figure 2.8. A comparison of the E-plane radiation patterns at 18 GHz by using two different methods: the reciprocity/spectral-domain periodic Moment method and the TEN network model. An extra half-wavelength is added to the air cavity in both models.

From Figure 2.8 we see that the main beams of the two patterns are now in good agreement.

2.3 Single Cavity: Substrate Board Design

In the previous section, we considered the 2-D arrays of metal patches that form the PRS in a theoretical design that is suspended in air. In this section, we introduce a substrate board design where the PRS consists of a periodic patch structure that is placed on a 60 mil thick Arlon Diclad 527 board. A board thickness t of 60 mils was chosen to provide a rigid support for the patch structure to avoid sagging. The method of analysis of this structure is given in the following section.

2.3.1 Spectral Domain Periodic MoM and Calculation of Shunt Susceptances

A side view of two different versions of a single cavity FPCA with a substrate board included is given Figure 2.9.

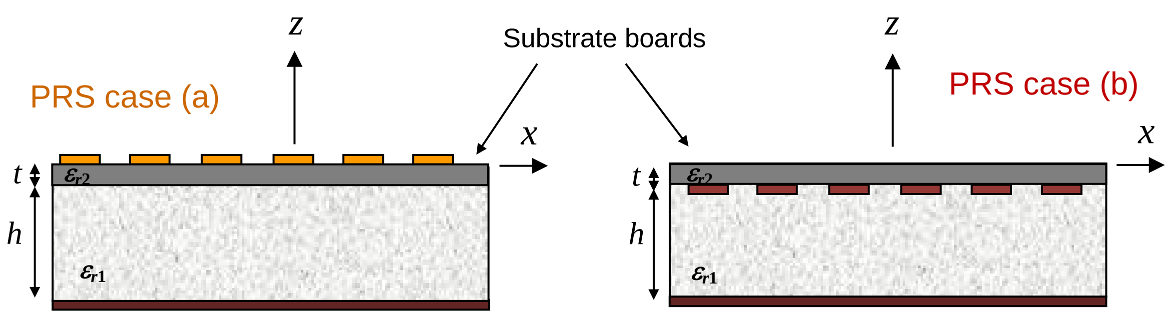

Figure 2.9. A side view of two different versions of a single cavity FPCA with substrate board included.

In Figure 2.9, we consider the cavity to be of height h with an arbitrary substrate permittivity, ε_{r1}. The substrate board is of thickness t = 60 mil (0.1524 cm) and has a permittivity of $\varepsilon_{r2} = 2.5$. For convenience, we shall consider the most general case where the 2-D array of metal patches may be placed either on the top or bottom surface of the substrate board to form the PRS. When the metal patch array is placed on the top of the substrate board, this case shall be referred to as case (a), and when the patch array is placed on the bottom surface of the board, this case shall be referred to as case (b). We define the patch embedding distance t_p such that, for case (a) when the patches are on the top of the substrate board, $t_p = 0$; for case (b) when the patches are on the bottom surface of the substrate board, $t_p = t$.

The field at the source location and hence the far-field (from reciprocity) may be obtained by following the same spectral domain periodic moment method of sub-section 2.2.4. However, here we must take into account the presence of the substrate board. Accordingly, we have

$$\underline{E}^{tot} = \underline{E}^{layer} + \underline{E}^{sca}, \tag{2.28}$$

where the x-component of the layer field as a function of embedding distance t_p ($z = -t_p$) is given as

$$\underline{E}_x^{layer}\left(t_p\right) = \frac{\underline{E}_x^{inc}\left(1+\Gamma^T\right)}{e^{jk_{z2}^{pw}t_p} + \Gamma_1^T e^{-jk_{z2}^{pw}t_p}}\left(1+\Gamma_1^T\right) \ . \tag{2.29}$$

The term E_x^{inc} is given in Equation (2.1). Here,

$$\Gamma^T = \frac{Z_{in}^T - Z_0^T}{Z_{in}^T + Z_0^T}, \tag{2.30}$$

where Z_{in}^T is given as

$$Z_{in}^T = Z_2^T\left[\frac{jZ_1^T \tan\left(k_{z1}^{pw}h\right) + jZ_2^T \tan\left(k_{z2}^{pw}t\right)}{Z_2^T - Z_1^T \tan\left(k_{z1}^{pw}h\right)\tan\left(k_{z2}^{pw}t\right)}\right]. \tag{2.31}$$

The subscript T stands for either the TM_z or TE_z incidence. The reflection coefficient Γ_1^T is given as

$$\Gamma_1^T = \frac{jZ_1^T \tan\left(k_{z1}^{pw} h\right) - Z_2^T}{jZ_1^T \tan\left(k_{z1}^{pw} h\right) + Z_2^T}. \tag{2.32}$$

The scattered field E_x^{sca} and the field at the source location, $E_x\left(x_0, y_0, -h_d\right)$, are of the same form as Equations (2.16) and (2.25), respectively. The spectral-domain Green's function component G_{xx} that accounts for the substrate board for this practical design is provided in the Appendix.

Similar to the hypothetical air case, we once again use the spectral-domain periodic moment method to calculate the shunt susceptance modelling the 2-D patch array in both case (a) (t_p = 0) and case (b) (t_p = t). Again, the height of the cavity is elongated and made to be equal to an odd multiple of a quarter wavelength in order to ensure the presence of the (0,0) Floquet mode only and to avoid contamination from higher-order modes. Here we shall directly provide the expressions for the equivalent shunt susceptances for the both cases. These expressions are obtained when considering broadside incidence. Detailed derivations for the shunt susceptance expressions of Equations (2.33) and (2.37) are provided in the Appendix.

The TEN model for case (a) where the patch structure is replaced by a shunt admittance jB_s is given in Figure 2.10.

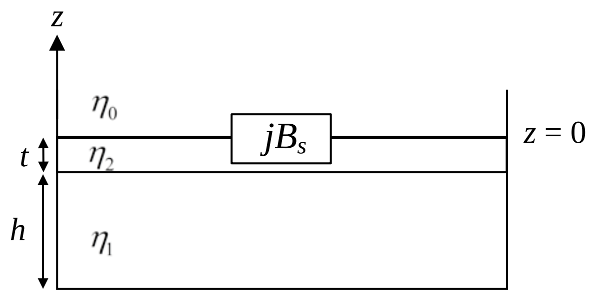

Figure 2.10. The TEN model for the PRS case (a), where the PRS layer is on the top surface of the substrate board.

The shunt susceptance B_s is given as

$$B_s = -jY_0 \left(\frac{1-\Gamma_L}{1+\Gamma_L} \right) + jY_{in} , \tag{2.33}$$

where

$$Y_0 = \frac{1}{\eta_0} \text{ and } Z_{in} = \frac{1}{Y_{in}} = \eta_2 \left[\frac{j\eta_1 \tan(k_1 h) + j\eta_2 \tan(k_2 t)}{\eta_2 - \eta_1 \tan(k_1 h) \tan(k_2 t)} \right] , \tag{2.34}$$

and

$$\Gamma_L = V(0) - 1. \tag{2.35}$$

Here $V(0)$ (with voltage modelling E_x) is the voltage at $z = 0$, and is given as

$$V(0) = E_x^{inc}(1+\Gamma) + \frac{1}{ab} \sum_{n=1}^{N} A_n \tilde{G}_{xx}(k_{x0}, k_{y0}) \tilde{B}_n(k_{x0}, k_{y0}) e^{-j(k_{x0}x + k_{y0}y)} . \tag{2.36}$$

The term Γ of Equation (2.36) is the same as that given in Equation (2.30), but is calculated for broadside incidence. The TEN for case (b) is given in Figure 2.11.

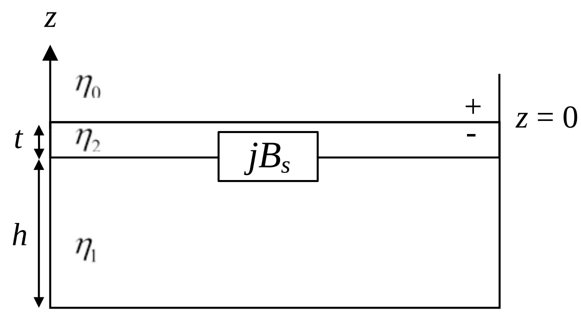

Figure 2.11. The TEN model for the PRS case (b), where the PRS layer is on the bottom surface of the substrate board.

The shunt susceptance B_s is given as

$$B_s = -jY_2\left[\frac{1-\Gamma_L}{1-\Gamma_L}\right] + Y_1 \cot\left(k_1 h\right), \tag{2.37}$$

where

$$Y_1 = \frac{1}{\eta_1} \text{ and } Y_2 = \frac{1}{\eta_2} \tag{2.38}$$

and

$$\Gamma_L = \frac{Z_{in} - \eta_2}{Z_{in} + \eta_2} e^{j2k_2 t} \;. \tag{2.39}$$

The term Z_{in} in Equation (2.39) is given as

$$Z_{in} = Z_0\left[\frac{1+\Gamma^+}{1-\Gamma^+}\right], \tag{2.40}$$

where

$$\Gamma^+ = V\left(0\right) - 1 \;. \tag{2.41}$$

The term $V(0)$ is the voltage at $z=0$ and is in the same form as Equation (2.36). It is found that for a given design frequency, the values of the shunt susceptance B_s is the same for either case (a) or case (b). It must also be noted the extraction of B_s is shown here for an arbitrary substrate permittivity of the antenna cavity. As previously mentioned, in our study, the cavity is air filled, and hence, when calculating the shunt susceptances for our case, in the above derivation η_1 is replaced by η_0 and k_1 is replaced by k_0.

2.3.2 Calculation of Cavity Height for Practical Design using TRE

Once the shunt susceptance modelling the periodic structure in either case (a) or case (b) are found, we may calculate the respective heights of the air cavities using the TRE. Let us first consider case (a) where the patch structure is on the top layer of the substrate board. The TEN model of this case is shown in Figure 2.12.

Placing the reference plane (marked as *R* in Figure 2.12) just below the patch structure, we may apply the TRE of Equation (2.26) to obtain the air cavity height h. From this equation, we find the cavity height to be

$$h=\frac{1}{k_1}\cot^{-1}\left[-\frac{Y_2}{Y_1}\left(\frac{B_s+Y_2\tan\left(k_2t\right)}{B_s\tan\left(k_2t\right)-Y_2}\right)\right], \tag{2.42}$$

where Y_1 and Y_2 are given in Equation (2.38). Similar to the theoretical air case, during the process of calculating the cavity heights for case (a) as well as case (b), a half-wavelength at the particular dual-band frequency of operation is added in order to avoid higher-order Floquet modes within the cavities.

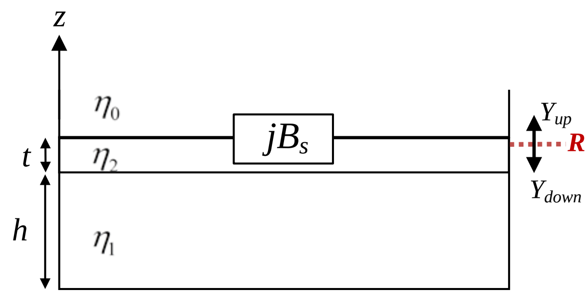

Figure 2.12. The TEN model for calculation of cavity height for PRS case (a).

The TEN for case (b) is given in Figure 2.13.

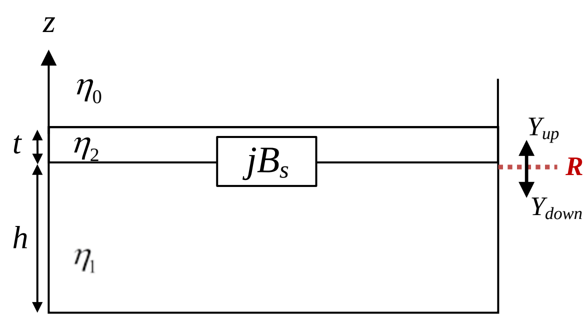

Figure 2.13. The TEN model for calculation of cavity height for PRS case (b).

The reference plane (marked as R in Figure 2.13) is placed just below the location of the patch structure and the TRE is

$$\mathrm{Im}\left(Y_{up}\right) = -\mathrm{Im}\left(Y_{down}\right). \tag{2.43}$$

Here,

$$Y_{up} = jB_s + Y_2\left[\frac{Y_0 + jY_2\tan\left(k_2 t\right)}{Y_2 + jY_0\tan\left(k_2 t\right)}\right]. \tag{2.44}$$

From Equations (2.43) and (2.44), we find the cavity height h to be

$$h = \frac{1}{k_1}\cot^{-1}\left[\frac{\mathrm{Im}\left(Y_{up}\right)}{Y_1}\right]. \tag{2.45}$$

Again it must be noted that since we are considering air cavities, Y_1 must be replaced by Y_0 and k_1 by k_0 in Equations (2.42) and (2.45).

2.3.3 Comparison of E-plane Radiation Patterns

Figure 2.14 shows a comparison of the E-plane pattern at 12 GHz using the two different methods. Figure 2.14 (a) is for case (a) and Figure 2.14 (b) is for case (b). Here, the 2-D patch array dimensions are *L* = 1.25 cm, *W* = 0.1 cm, *a* = 1.35 cm and *b* = 0.3 cm. In our analysis, we consider the cavity to be air and hence its relative permittivity, $\varepsilon_{r1} = 1$. The cavity height for case (a) is $h = 1.123$ cm and for case (b), the cavity height $h = 1.285$ cm. The source dipole location $h_d = h/2$ (the source dipole is in the middle of the air cavity). The substrate board has a thickness *t* = 0.1524 cm and has a relative permittivity of $\varepsilon_{r2} = 2.5$.

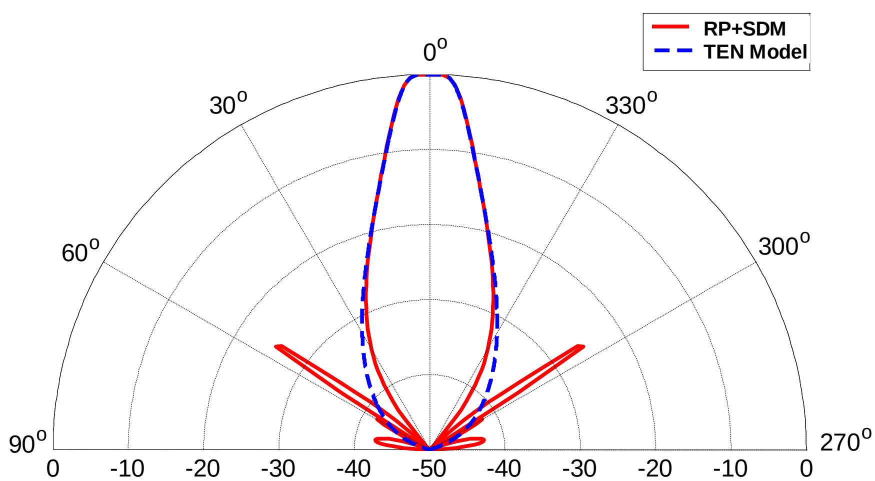

(a) PRS case (a)

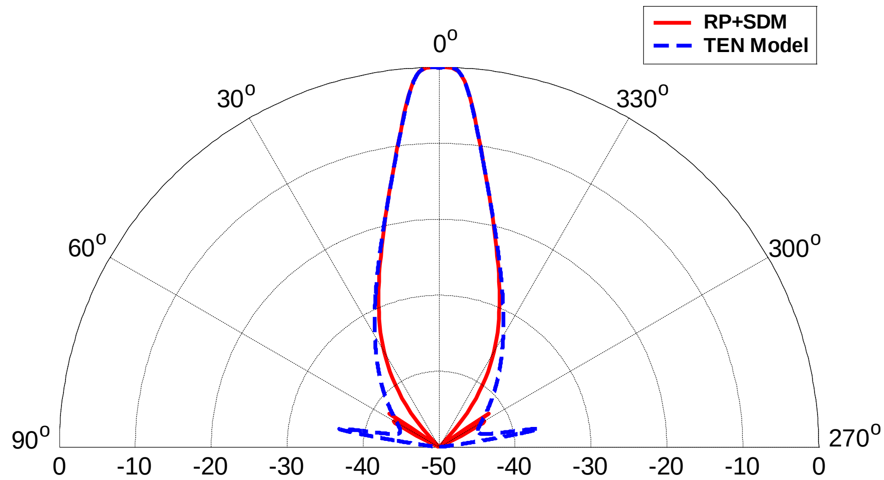

(b) PRS case (b)

Figure 2.14. A comparison of the E-plane radiation patterns at 12 GHz by using two different methods: the reciprocity/spectral-domain periodic moment method and the TEN network model. (a) PRS case (a), where $h = 1.123$ cm. (b) PRS case (b), where $h = 1.285$ cm.

From Figure 2.14 we see that there is good agreement between the two methods for the main beam E-plane radiation patterns in both cases at 12 GHz. In Figure 2.14 (a), both E-plane patterns were found to have a 3-dB beamwidth of 10°. In Figure 2.14 (b), both E-plane patterns were found to have a 3-dB beamwidth of 9.4°.

Figure 2.15 shows a comparison of the E-plane pattern at 18 GHz, using the two different methods. Figure 2.15 (a) is for PRS case (a) and Figure 2.15 (b) is for the PRS case (b). The 2-D patch array dimensions are unaltered from the 12 GHz case. The air has a relative permittivity $\varepsilon_r = 1$ and the cavity height for case (a) is $h = 0.613$ cm while for case (b), the cavity height $h = 0.814$ cm. The source dipole location is $h_d = h/2$ (the source dipole is in the middle of the air cavity).

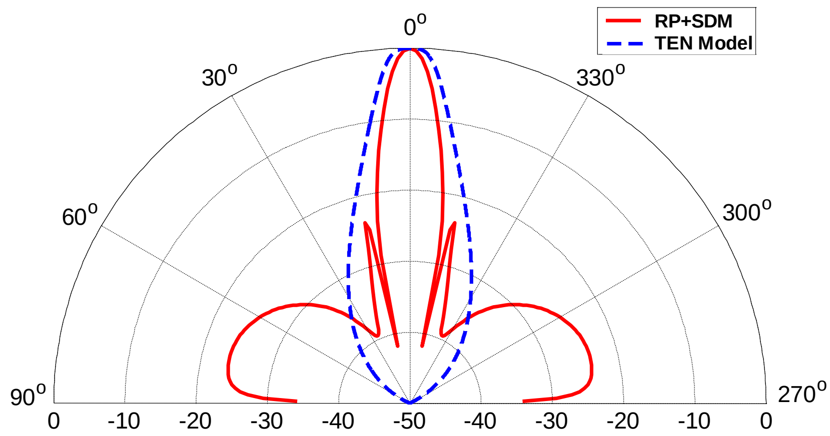

(a) PRS case (a)

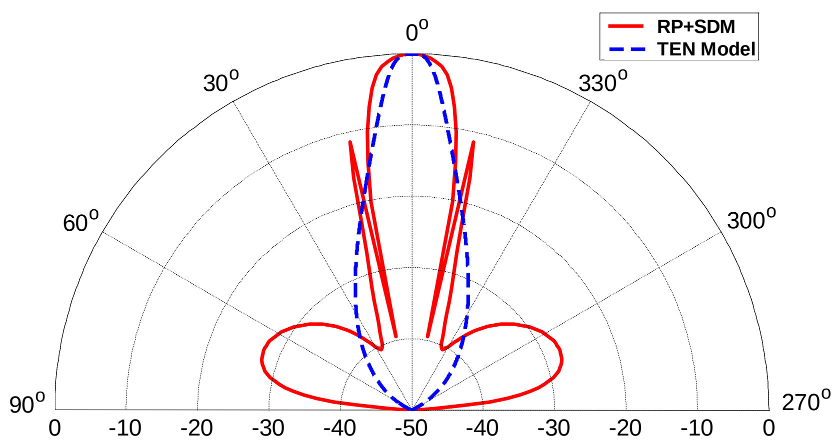

(b) PRS case (b)

Figure 2.15. A comparison of the E-plane radiation patterns at 18 GHz by using two different methods: the reciprocity/spectral-domain periodic moment method and the TEN network model. (a) PRS case (a), where $h = 0.613\,\text{cm}$. (b) PRS case (b), where $h = 0.814\,\text{cm}$.

In case (a) of Figure 2.15 (a), we observe a discrepancy in the two E-plane radiation patterns. The 3-dB beamwidth of the pattern obtained from reciprocity/spectral-domain periodic moment method is 5.8° while that obtained from the TEN model is 8.9°. We observe a similar disagreement in the patterns of case (b) of Figure 2.15 (b) as well. For case (b), the 3-dB beamwidth of the pattern obtained from the spectral-domain moment method is 12.4° while that from the TEN model is 8°. In an attempt to overcome this discrepancy, an extra half-wavelength is added to the air cavity at 18 GHz as was done in the air case design of sub-section 2.2.6. However, this attempt did not successfully overcome the problem. The discrepancy in the E-plane patterns at 18 GHz is speculated to be a result of the value of the shunt susceptance modelling the periodic patch layer at 18 GHz. It must be noted that the values of B_s used in the TEN model are considered to be independent of the incident angle and are calculated only once for broadside incidence. At 12 GHz, for either case (a) or case (b), it was found that the using the appropriate shunt susceptance value that is independent of incident angle in the TEN model was sufficient to obtain good agreement with the patterns obtained from the spectral-domain periodic moment method. However, when using a B_s value that is independent of incident angle in the TEN model at 18 GHz, it was found that the magnitudes of the E_x field at the source location (and hence the far-field due reciprocity) vary largely in comparison to those obtained from the method of moments. It is hence speculated that for better agreement between the patterns, the values of the shunt susceptance used in the TEN model in either case (a) or case (b) at 18 GHz must depend on the incident angle. Of course, the result from the periodic moment method is the more accurate of the two.

2.4 Conclusion

In this chapter, a Fabry-Pérot single cavity antenna is studied. An air substrate case is considered first, and the method to calculate the far-field using reciprocity and the spectral-domain periodic moment method was explained. The calculation of the shunt susceptance modelling the periodic patch structure and its role in the Transverse

Equivalent Network (TEN) model was discussed. The calculation of the cavity height using the Transverse Resonance Equation (TRE) was explained, and an expression for the cavity height *h* was provided. The E-plane radiation patterns obtained from the spectral-domain periodic moment method and the TEN model were compared. The E-plane patterns at 12 GHz were found to be in good agreement. At 18 GHz, however, the patterns were not found to be in good agreement, and the discrepancy was overcome by adding an extra half-wavelength to the air cavity height.

The substrate board structure was presented next, in which the periodic patch structure was placed on either the top or bottom surface of the substrate board. The necessary modification in the analysis of the spectral-domain periodic moment method along with the extraction of the equivalent shunt susceptance was explained. The expression for the air cavity height was again provided by the TRE. The E-plane patterns obtained from the two methods were compared at both 12 GHz and 18 GHz. The patterns were found to be in good agreement at 12 GHz, but a discrepancy in the patterns was again found at 18 GHz, which was not overcome by adding an extra half wavelength to the cavity height. It was speculated that using shunt susceptance values that are dependent on incident angle would overcome this discrepancy.

Chapter 3

Dual-Band Fabry-Pérot Resonant Cavity Antennas

Chapter 3 examines a dual-band version of the Fabry-Pérot resonant cavity antenna. We begin this chapter with a brief introduction in Section 3.1. In Section 3.2, a theoretical dual-band design is proposed, and a systematic procedure to obtain dual-band behavior is explained. Section 3.3 provides an iterative method to obtain optimum beam shapes and equal directivities at the two specified design frequencies. In Section 3.4, a dual-band design with the inclusion of substrate boards is studied, and an optimization of its radiation patterns is discussed in Section 3.5. Section 3.6 provides some conclusions and comments on the proposed models.

3.1 Introduction

In the literature, it is found that for dual-band operation, many structures use dual-layer PRSs; however, it is the intention of this research to examine a dual-band version of the Fabry-Pérot resonant cavity antenna that uses a frequency selective surface (FSS) layer above a ground plane to form an composite reactive ground plane that replaces the single metal ground plane in a conventional Fabry-Pérot resonant cavity antenna. The composite ground plane is in the form of a capacitive FSS screen, composed of a rectangular metal patch array, suspended above a PEC ground plane. This composite ground plane is chosen to have the desired frequency response to enable dual-band operation, so that the overall cavity, i.e., the region between the top PRS and the ground plane, is resonant at two frequencies. The FSS layer has a resonance frequency at which it acts as a short circuit (a reflection coefficient of -1) and hence behaves as a "virtual ground plane" at that frequency. Using an FSS layer allows for two resonance frequencies of the composite cavity, and this in turn allows for establishing two frequencies at which the structure is resonant and hence radiates a beam at broadside.

3.2 Dual-Band Design: Air Case

3.2.1 Dual-Band Antenna Geometry

The geometry of the proposed dual-band antenna is shown in Figure 3.1.

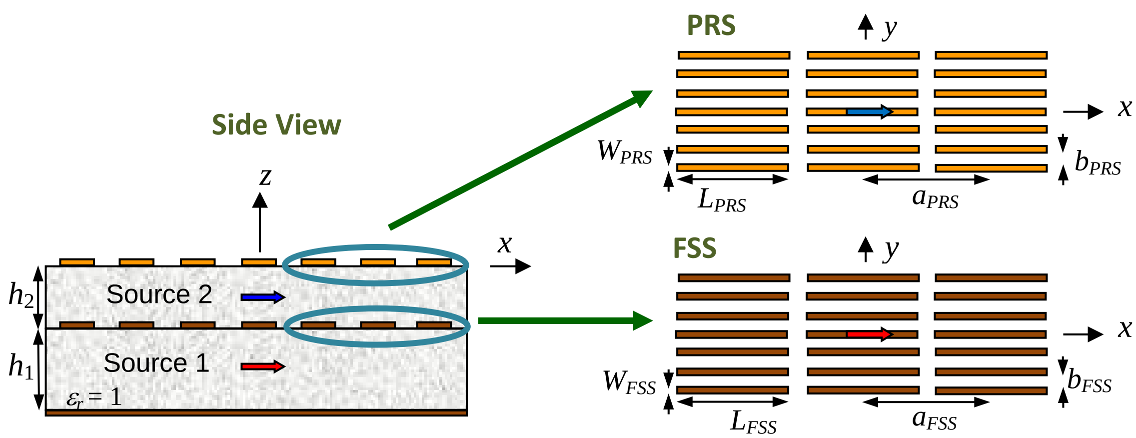

Figure 3.1. Side view of the dual-band antenna geometry, along with a top view of the PRS and FSS layers.

The top layer of the antenna consists of a 2-D array of metal patches of given length, width and periodicity which forms the PRS. The FSS layer within the composite cavity may be chosen as a frequency scaled version of the PRS (though this is not a requirement). In this hypothetical design, both layers are suspended in air. The two sources of excitation are unit-amplitude horizontal electric dipoles (HEDs). They are placed in the upper and lower cavity regions (above and below the FSS) and are intended to operate at the higher and lower specified resonances, respectively. Here, we consider all cavity regions to be air.

3.2.2 Calculation of the Far-Field

Once again, as in Chapter 2, reciprocity is used to calculate the far-field pattern. A "testing" dipole is placed at the observation point in the far field in order to sample the electric field there. The far field at the observation point is equated to the field E_x at the original source location due to an incident plane wave from the "testing" dipole. The calculation thus reduces to a calculation of the field inside the substrate due to a plane wave incidence as explained in Chapter 2 [50].

A simple Transverse Equivalent Network (TEN) model is also used to calculate the field E_x inside the antenna due to a plane-wave incidence. Here, the field E_x of the (0,0) Floquet harmonic inside the substrate due to a plane wave incidence is calculated by finding the voltage on an equivalent transmission-line model, where the voltage represents the transverse electric field component E_x. This method neglects the higher-order Floquet modes at the dipole location. The general structure of a multi-layer Fabry-Pérot resonant cavity antenna and its TEN model are given in Figure 3.2.

In the TEN of Figure 3.2, shunt admittances are used to represent the 2D periodic array of metal patches of the PRS as well as the FSS layers above the grounded substrate. The superscript T denotes either TM or TE. The characteristic impedances of the substrate layers are given by

$$Z_i^{TM} = \frac{k_{zi}}{\omega \varepsilon_i} \tag{3.1}$$

and

$$Z_i^{TE} = \frac{\omega\mu_i}{k_{zi}} \ . \tag{3.2}$$

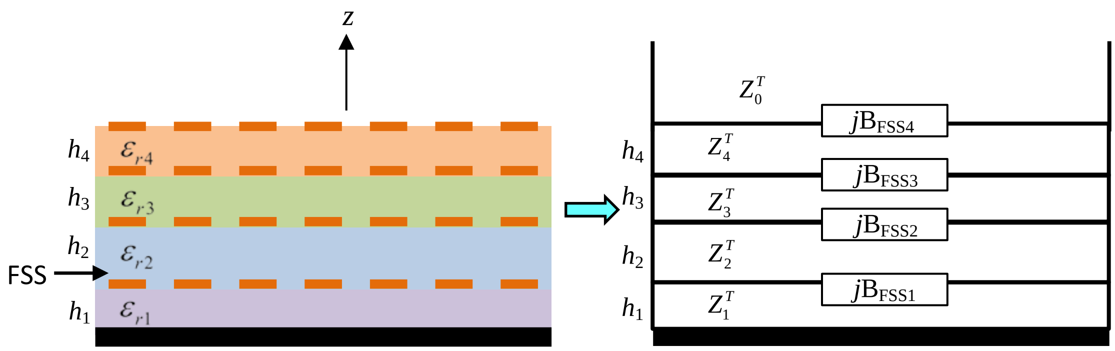

(a) (b)

Figure 3.2. (a) The general structure of a multi-layer Fabry-Pérot resonant cavity antenna and (b) its transverse equivalent network (TEN) model.

In our case, we will take all cavity regions to be air. The shunt admittances used to represent the PRS and FSS layers are calculated using the periodic spectral-domain Moment Method (MoM) as described in sub-section 2.2.3 of Chapter 2.

3.2.3 Design Principles for Dual-Band Structure

A design example of the proposed dual-band Fabry-Pérot resonant cavity antenna is given in Figure 3.3. The main design principle of this structure is that at an FSS resonance frequency, the patch FSS behaves as a short circuit. At the upper-band frequency f_2, the FSS behaves as a short circuit, and so the upper cavity of thickness (height) h_2 operates at this frequency. At the lower band frequency f_1, the lower cavity thickness h_1 is chosen so that the composite cavity structure of thickness (height) $h_1 + h_2$

operates at this frequency. The heights of the two cavities, h_1 and h_2, are calculated using the Transverse Resonance Equation (TRE).

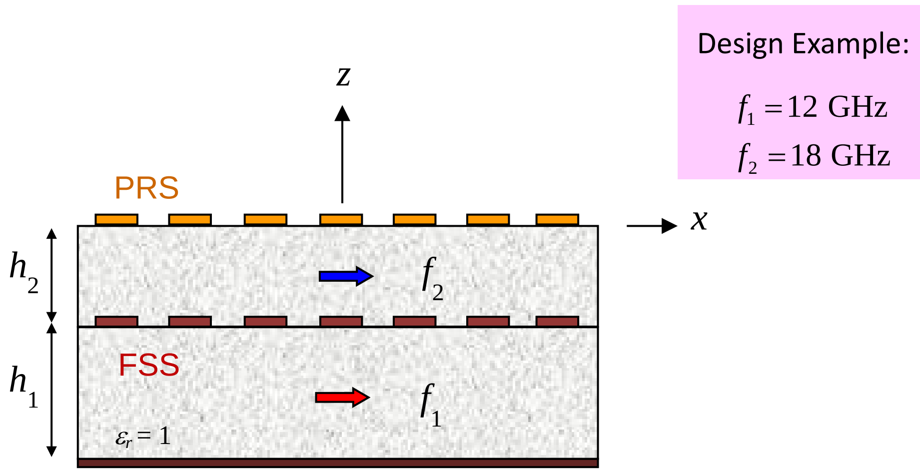

Figure 3.3. Design example for the proposed air-cavity case dual-band structure.

3.2.4 Calculation of Cavity Heights Using TRE

The cavity heights h_1 and h_2 for any two given design frequencies are initially calculated using the transverse resonance equation (TRE) to achieve resonance. The TEN model of the design example of Figure 3.3 is shown in Figure 3.4.

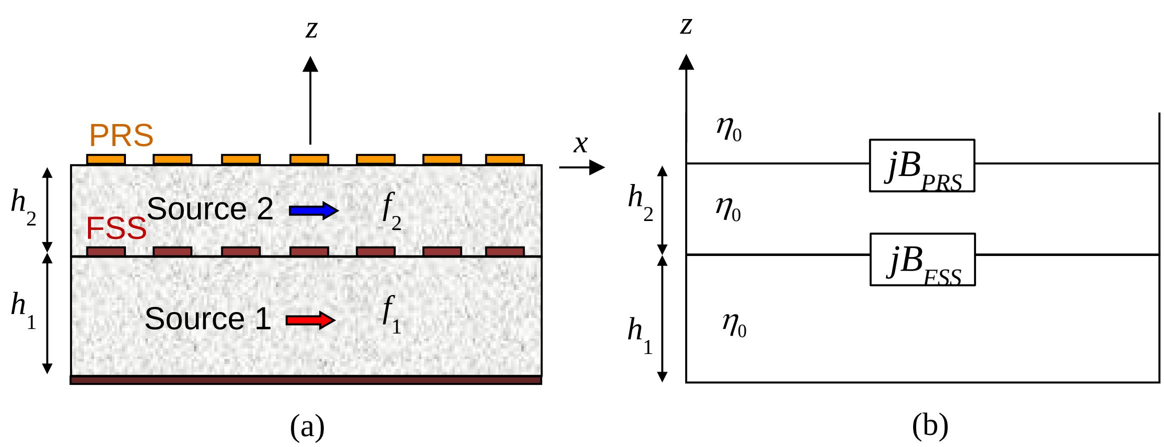

Figure 3.4. (a) Dual-band design example. (b) TEN model.

We calculate the cavity heights starting from the location of the PRS and work our way down to the ground plane of the structure. The TEN models for the calculation of the cavity heights are given in Figure 3.5.

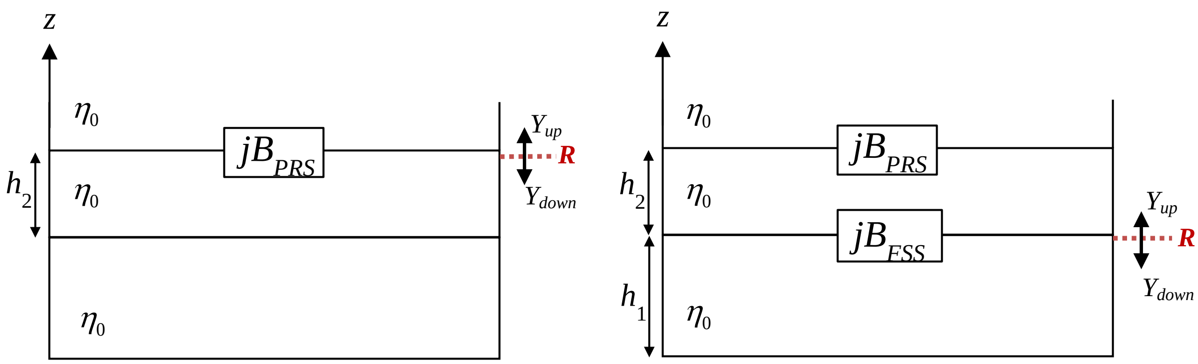

(a) (b)

Figure 3.5. The TEN model for calculation of the cavity heights. (a) Model for calculating h_2 at $f_2 = 18$ GHz. (b) Model for calculating h_1 at $f_1 = 12$ GHz.

Since both the PRS and FSS screens are lossless, the load admittances modelling them in the TEN are pure imaginary as seen in Figure 3.5. At the upper-band frequency f_2, the FSS behaves as a short circuit. Putting the reference plane (marked as *R* in Figure 3.5 (a)) just below the PRS and applying the imaginary part of the TRE, we have

$$\mathrm{Im}\left(Y_{up}\right) = -\mathrm{Im}\left(Y_{down}\right). \tag{3.3}$$

Here, Y_{up} is the admittance looking upwards and Y_{down} is the admittance looking downwards. From Equation (3.3), we may obtain the cavity height h_2, which is given by

$$h_2 = \frac{1}{k_0}\cot^{-1}\left(\eta_0 B_{PRS}\right) . \tag{3.4}$$

At the lower-band frequency f_1, the FSS is modeled by its appropriate load admittance, as seen in Figure 3.5 (b). By applying the imaginary part of the TRE with the reference plane just below the FSS, we may obtain the cavity height h_1 using the same Equation (3.4) with h_2 replaced by h_1.

During the process of calculating the cavity heights, a half-wavelength at the particular dual-band frequency of operation is added. This is to avoid having the two patch layers from being too close to one another, and hence avoiding higher-order Floquet mode interaction within the cavities.

3.3 Results for Air Case

3.3.1 Dual-Band Model: Initial Design

A plot of the broadside directivity versus frequency for the initial design of the dual-band model is given in Figure 3.6 for a structure designed for $f_1 = 12\,\text{GHz}$ and $f_2 = 18\,\text{GHz}$. Here, the PRS patch array dimensions are L_{PRS} = 1.25 cm, W_{PRS} = 0.1 cm, a_{PRS} = 1.35 cm and b_{PRS} = 0.3 cm. The FSS patch array dimensions are L_{FSS} = 1.319 cm, W_{FSS} = 0.106 cm, a_{FSS} = 1.425 cm and b_{FSS} = 0.317 cm. Both cavities have a relative permittivity ε_r = 1 and the cavity heights are h_1 = 1.324 cm and h_2 = 0.841 cm. The rapid oscillation observed in the plots is due to numerical noise in calculating the directivity.

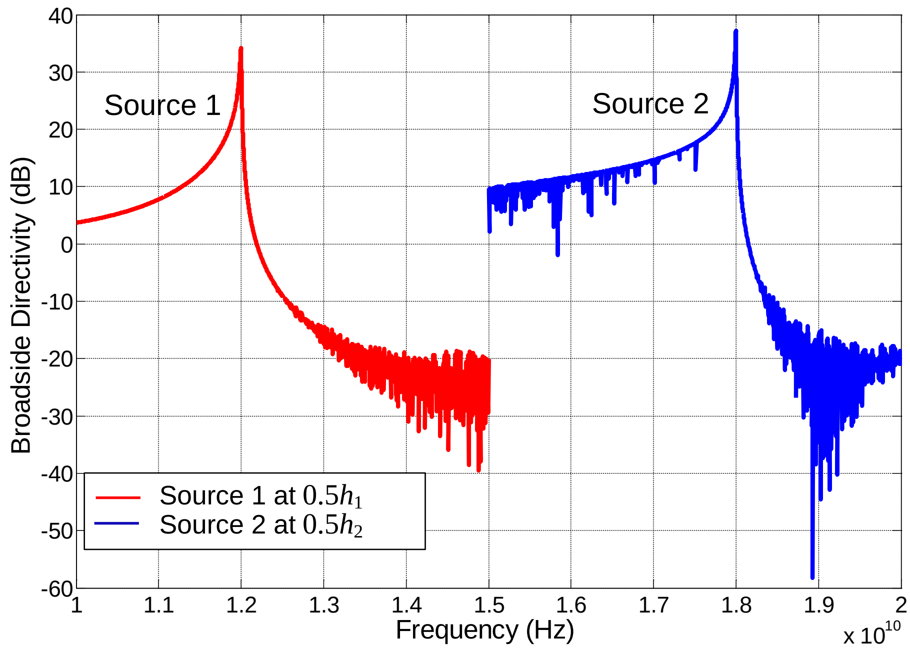

Figure 3.6. Broadside directivity versus frequency for the air-cavity initial dual-band design.

Table 3.1 gives the values of the maximum broadside directivity as well as the power density radiated at broadside at the respective frequencies where the directivities are maximum.

Table 3.1. Broadside directivity and broadside power density for the air-cavity initial dual-band design.

Source	Frequency f_n (GHz) (n =1,2)	Directivity D_n^{max} (dB) (n =1,2)	Power density P_n^{rad} (W/m^2) (n =1,2)
1	12	34.14	4.73
2	18	37.18	10.37

From Table 3.1, it is observed that the maximum directivities as well as the radiated broadside power densities obtained at f_1 and f_2 are not equal. The E-plane radiation patterns at the two dual-band frequencies are shown in Figure 3.7.

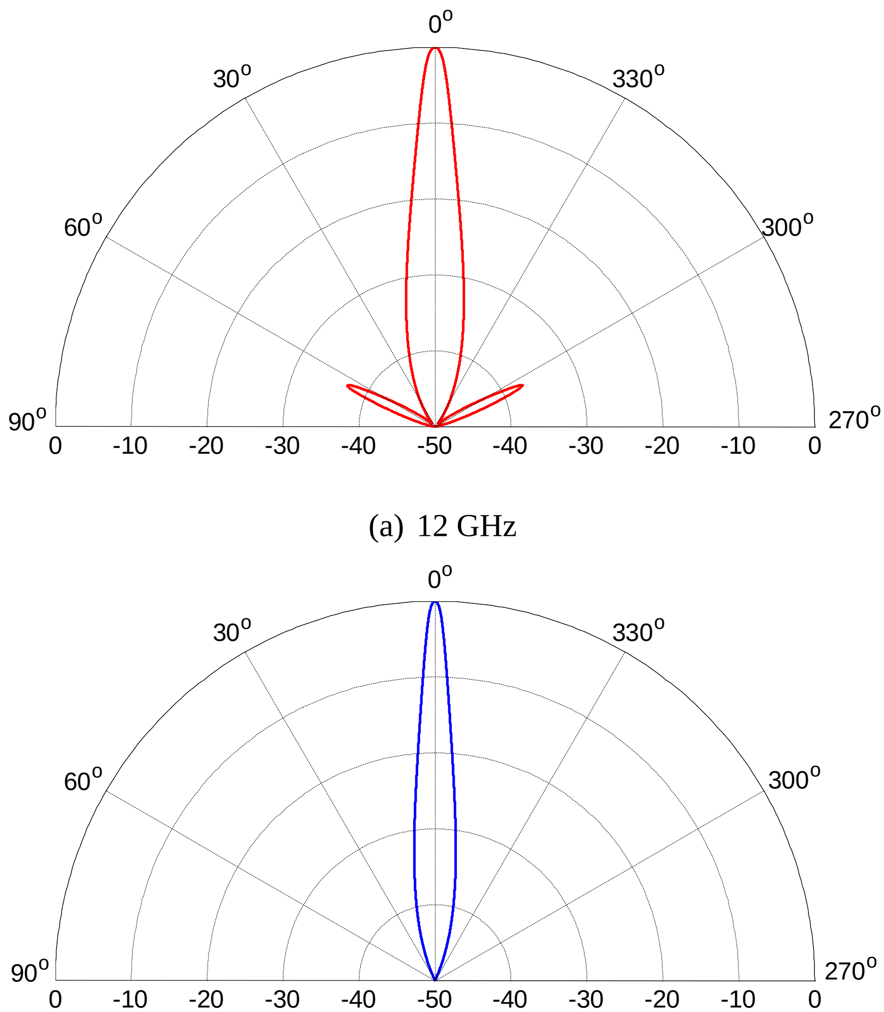

(a) 12 GHz

(b) 18 GHz

Figure 3.7. E-plane radiation patterns for the air-cavity initial dual-band design.

From Figure 3.7, it is observed that the beamwidths of these two patterns are not the same, in accordance with the different directivities in Table 3.1. The goal here is to obtain equalized directivities and power densities at the two dual-band frequencies, and in order to do so, an iterative method is implemented, as explained in the next section. It must be noted that the goal to equalize the broadside directivities at the two dual-band frequencies is somewhat arbitrary; we could also choose to have a ratio of directivities that is different from unity. For the power densities at broadside, equalizing them is even more arbitrary and not very practical; it is simply to show that we have this flexibility. In a practical design with actual feeds, having an input match is quite often the most important aspect.

3.3.2 Iterative Design Method

Since the TRE calculates the cavity heights that will give peak power density at the design frequencies f_1 and f_2, we can consider the cavity heights h_1 and h_2 as functions of the PRS resonance frequency f_0. If we denote the directivity as $D\left(f, f_0, h_1\left(f_0\right), h_2\left(f_0\right)\right)$, then in equation form, our directivity equalization problem is thus

$$D\left(f_1, f_0, h_1\left(f_0\right), h_2\left(f_0\right)\right) = D\left(f_2, f_0, h_1\left(f_0\right), h_2\left(f_0\right)\right) \tag{3.5}$$

or

$$D\left(f_1, f_0, h_1\left(f_0\right), h_2\left(f_0\right)\right) - D\left(f_2, f_0, h_1\left(f_0\right), h_2\left(f_0\right)\right) = 0\,. \tag{3.6}$$

Hence, the problem reduces to solving an equation of the form

$$F\left(f_0\right) = 0\ . \tag{3.7}$$

In order to solve Equation (3.7), any root finding method may be used. Here we use the secant method where we require two initial guesses for the PRS resonance frequency f_0. Calling these initial guesses $f_{0_{i-1}}$ and f_{0_i}, we may then obtain the next value $f_{0_{i+1}}$ from the equation

$$f_{0_{i+1}} = f_{0_i} - \frac{F\left(f_{0_i}\right)\left(f_{0_i} - f_{0_{i-1}}\right)}{F\left(f_{0_i}\right) - F\left(f_{0_{i-1}}\right)} \ . \tag{3.8}$$

Once $f_{0_{i+1}}$ is calculated, we check to see if it satisfies Equation (3.7). We continue the iterative process of Equation (3.8) until the appropriate PRS resonance frequency f_0 that solves Equation (3.7) is found. A final design in which the broadside directivities and power densities at the dual-band frequencies are equalized is then obtained from the iterative flow chart of Figure 3.8.

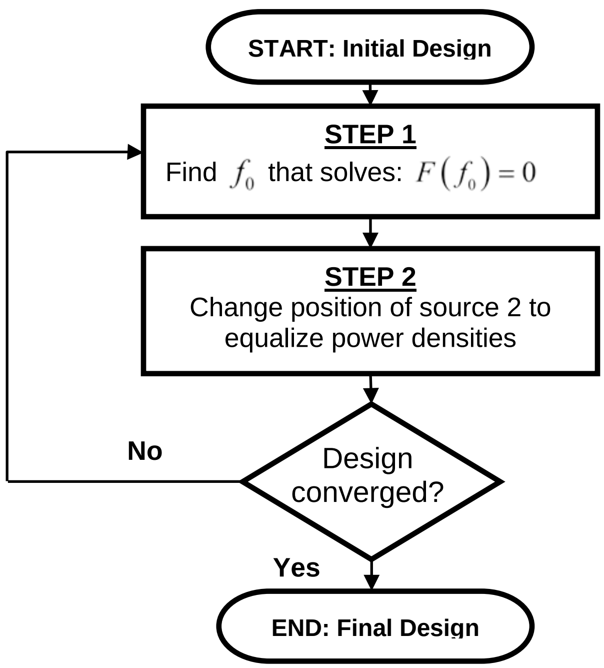

Figure 3.8. Iterative flow chart to obtain optimized radiation patterns for the air-cavity dual-band design.

3.3.3 Dual-Band Model: Final Design

After applying the iterative method of Section 3.3.2 to the initial design, a final design in which the radiation patterns are optimized at the two specified design frequencies is obtained (narrow beams with equal directivity and power density at broadside at the two frequencies). The PRS patch array dimensions are L_{PRS} = 1.391 cm, W_{PRS} = 0.111 cm, a_{PRS} = 1.503 cm and b_{PRS} = 0.334 cm. The FSS patch array dimensions are L_{FSS} = 1.319 cm, W_{FSS} = 0.106 cm, a_{FSS} = 1.425 cm and b_{FSS} = 0.317 cm. Both cavities have a relative permittivity $\varepsilon_r = 1$ and the cavity heights are h_1 = 1.324 cm and h_2 = 0.824 cm. A plot of the broadside directivity versus frequency for the final design is shown in Figure 3.9.

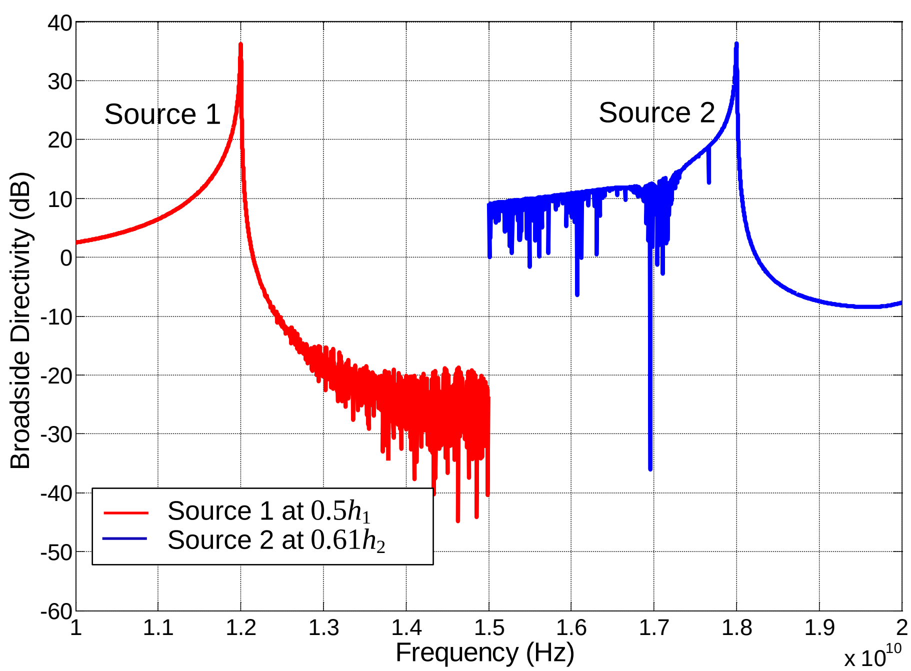

Figure 3.9. Broadside directivity versus frequency for the air-cavity final dual-band design.

The tolerances for the difference in broadside directivities, as well as broadside power densities, are

$$\left|D\left(f_1, f_0, h_1\left(f_0\right), h_2\left(f_0\right)\right) - D\left(f_2, f_0, h_1\left(f_0\right), h_2\left(f_0\right)\right)\right| \leq 0.15\,\mathrm{dB} \tag{3.9}$$

and

$$\left|P_{rad}\left(f_1, f_0, h_1\left(f_0\right), h_2\left(f_0\right)\right) - P_{rad}\left(f_2, f_0, h_1\left(f_0\right), h_2\left(f_0\right)\right)\right| \leq 0.1\left[\mathrm{W/m^2}\right]. \tag{3.10}$$

Table 3.2 shows that the directivities as well as broadside power densities obtained at the given dual-band frequencies for the final design are within the specified tolerances.

Table 3.2 Broadside directivity and power density for the final dual-band air-cavity design.

Source	Frequency f_n (GHz) (n =1,2)	Directivity $D_n^{\max}$ (dB) (n =1,2)	Power density P_n^{rad} (W/m^2) (n =1,2)
1	12	36.23	7.87
2	18	36.28	7.83

The E-plane radiation patterns at the two dual-band frequencies are given in Figure 3.10.

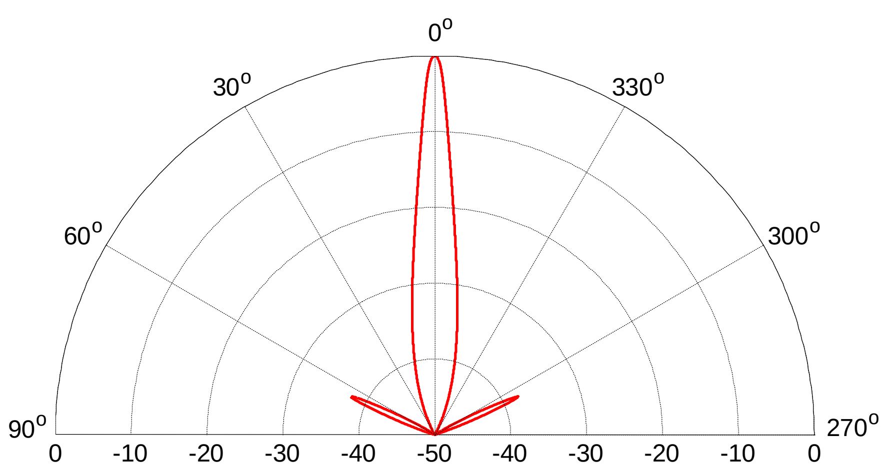

(a) 12 GHz

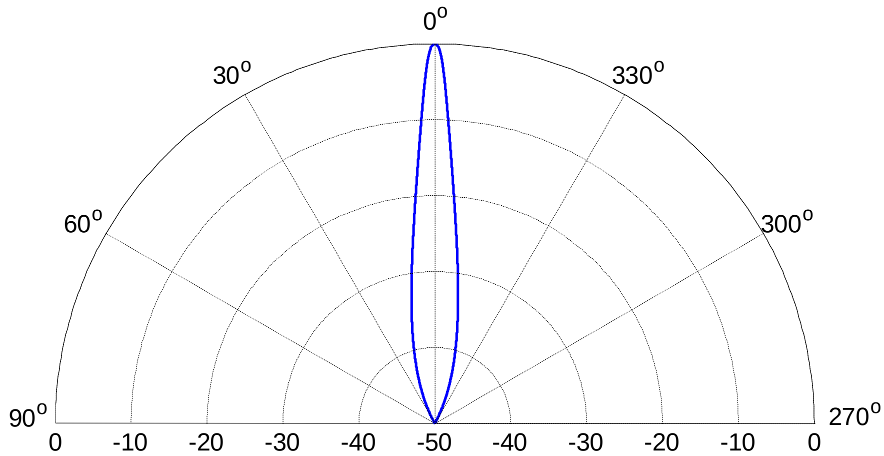

(b) 18 GHz

Figure 3.10. E-plane radiation patterns for the final dual-band air-cavity design.

From Figure 3.10, it can be observed that nearly equal optimized radiation patterns at the specified dual-band frequencies are now obtained.

3.3.4 Figure of Merit

An important property of Fabry-Pérot structures that is often studied is the figure of merit (FoM) which is defined as the product of the maximum broadside directivity $D^{\max}$ and the 3-dB pattern (broadside power density) bandwidth. For a regular-single cavity PRS structure, the maximum broadside directivity $D^{\max}$ and bandwidth BW are given as [51]

$$D^{\max} \approx \frac{9.87}{\Delta\theta_{3dB}\big|_E \, \Delta\theta_{3dB}\big|_H} \tag{3.11}$$

and

$$BW = \frac{2\sqrt{\varepsilon_r}}{\pi \bar{B}_{PRS}^2} \; . \tag{3.12}$$

Here, $\Delta\theta_{3dB}$ is the 3-dB beamwidth, which is given as

$$\Delta\theta_{3dB} \approx \frac{2}{\left|\overline{B}_{PRS}\right|}\sqrt{\frac{2\varepsilon_r^{3/2}}{\pi}} \quad , \tag{3.13}$$

where $\overline{B}_{PRS}$ is the normalized PRS shunt susceptance, which is given as

$$\overline{B}_{PRS} = B_{PRS}/\eta_0 \; . \tag{3.14}$$

From Equations (3.11) and (3.12), the figure of merit for a single cavity structure is found to be

$$\text{FoM} = D^{\max} \cdot BW = \frac{2.48}{\varepsilon_r} . \tag{3.15}$$

Since we are considering an air cavity, $\varepsilon_r = 1$ and the FoM for a single cavity structure would be 2.48. The figures of merit at 12 GHz and 18 GHz of the optimized dual-band design were calculated and a comparison with the figures of merit of the single cavity structure is provided in Table 3.3.

Table 3.3. A comparison of the figure of merits for the single cavity and dual-band air-cavity structures at 12 GHz and 18 GHz.

Source	Frequency f_n (GHz) (n =1,2)	Figure of Merit (single cavity)	Figure of Merit (dual-band)
1	12	2.48	3.34
2	18	2.48	3.27

From Table 3.3, it is observed that the figure of merit for the dual-band structure at both frequencies is higher than what the CAD formula of (3.15) predicts for the single cavity structure.

3.4 Dual-Band Design: Substrate Board Case

3.4.1 Inclusion of Substrate Boards

As we have seen in the previous section, in the dual-band air-cavity design, the PRS and FSS are suspended in air. In order to fabricate a practical structure, the layers must be placed on supporting substrate boards. The practical dual-band design example with such boards is shown in Figure 3.11.

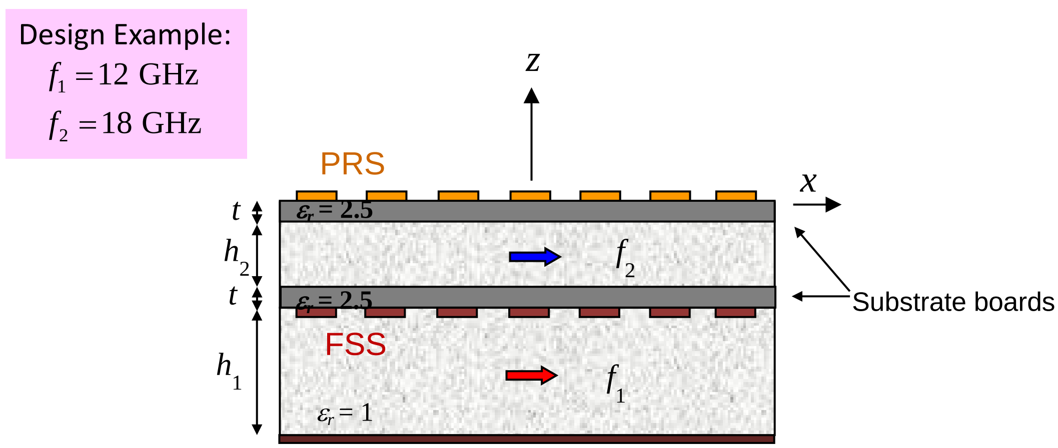

Figure 3.11. Design example for the proposed dual-band structure with substrate boards.

Here two identical Arlon Diclad 527 boards are used, each of which supports the PRS and FSS layers. From Figure 3.11, it can be observed that the PRS layer is placed on the upper surface of its supporting substrate board while the FSS is placed on the lower surface of its board. The FSS is chosen to be placed on the bottom of the substrate board as a practical aspect in light of future fabrication of this dual-band structure. With the FSS placed on the bottom of the substrate board, in a practical fabricated design, a planar-dipole could be placed on the top surface of the same board as a feeding structure. Once again, the two design frequencies are chosen to be 12 and 18 GHz. It must be noted that since the layers are now placed on substrate boards, the concept of frequency scaling the FSS with respect to the PRS is no longer valid. Instead, an appropriate scaling factor is numerically found such that the FSS is resonant at 18 GHz and hence, acts as a ground plane at this frequency. The cavity regions are again considered to be air.

3.4.2 Calculation of Shunt Susceptances and Cavity Heights

The shunt susceptance values that model the PRS and FSS layers in the TEN model of the practical design are calculated using the method described in Section 2.3.2 of Chapter 2. For the PRS layer, the shunt susceptance value B_{PRS} is obtained based on Equation (2.33) while the FSS layer shunt susceptance value B_{FSS} is calculated from Equation (2.37). Once they are calculated, they are placed in the TEN model of the practical design. Figure 3.12 shows the TEN models used to calculate the cavity heights h_1 and h_2 of the practical design given in Figure 3.11.

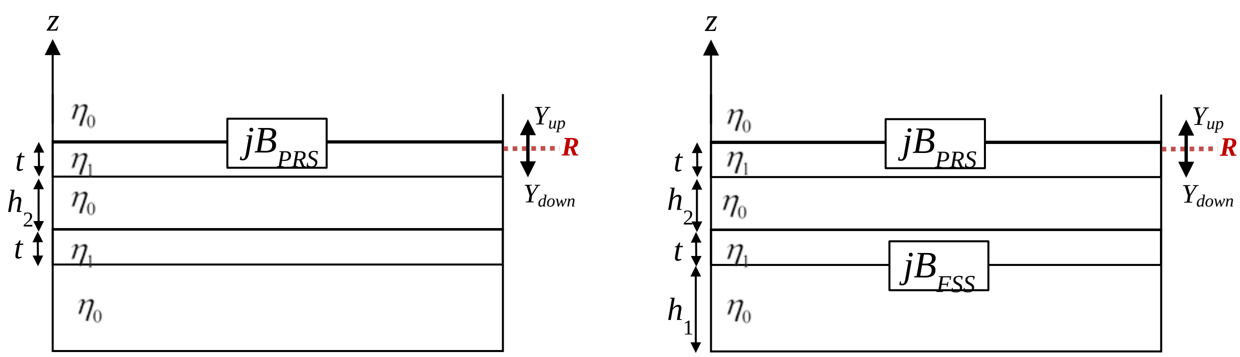

(a) (b)

Figure 3.12. The TEN model for calculation of cavity height. (a) Model for calculating h_2 at $f_2 = 18$ GHz. (b) Model for calculating h_1 at $f_1 = 12$ GHz.

As previously explained, at the upper-band frequency f_2, the FSS behaves as a short circuit. Putting the reference plane (marked as R in Figure 3.12 (a)) just below the

PRS, and using the imaginary part of the TRE, we find the cavity height h_2, which is given by

$$h_2 = \frac{1}{k_0}\tan^{-1}\left[\frac{\left(\frac{-Y_1^2\tan(k_1 t) - B_{PRS}Y_1}{-B_{PRS}\tan(k_1 t) + Y_1}\right) + Y_1\cot(k_1 t)}{Y_0 - \frac{Y_1\cot(k_1 t)}{Y_0}\left(\frac{-Y_1^2\tan(k_1 t) - B_{PRS}Y_1}{-B_{PRS}\tan(k_1 t) + Y_1}\right)}\right], \tag{3.16}$$

where,

$$Y_0 = \frac{1}{\eta_0} \text{ and } Y_1 = \frac{1}{\eta_1} . \tag{3.17}$$

At the lower-band frequency f_1, the FSS is modeled by its appropriate load admittance, as seen in Figure 3.12 (b). Again, placing the reference plane for the TRE just below the PRS, we find the cavity height h_1, and it is given by

$$h_1 = \frac{1}{k_0}\cot^{-1}\left[\frac{1}{Y_0}\left(\frac{-Y_1 b + Y_1^2\tan(k_1 t)}{Y_1 + b\tan(k_1 t)} + B_{FSS}\right)\right], \tag{3.18}$$

where the term b is given by

$$b = \frac{Y_0 a - Y_0^2\tan(k_0 h_2)}{Y_0 + \tan(k_0 h_2)a} , \tag{3.19}$$

and the term a is given by

$$a = \frac{Y_1^2\tan(k_1 t) + B_{PRS}Y_1}{B_{PRS}\tan(k_1 t) - Y_1} . \tag{3.20}$$

As was done in the air-cavity case, during the process of calculating the cavity heights, a half-wavelength at the particular dual-band frequency of operation is added in order to avoid having the two FSS layers be too close to one another, and hence avoiding higher-order Floquet mode interaction within the cavities.

3.5 Results for the Dual-Band Substrate Board Design

3.5.1 Initial Design

Table 3.4 gives the values of the broadside directivity as well as the power density radiated at broadside at the respective design frequencies for the initial dual-band substrate board design. Here, the PRS patch array dimensions are L_{PRS} = 1.25 cm, W_{PRS} = 0.1 cm, a_{PRS} = 1.35 cm and b_{PRS} = 0.3 cm. The FSS patch array dimensions are L_{FSS} = 1.056 cm, W_{FSS} = 0.084 cm, a_{FSS} = 1.140 cm and b_{FSS} = 0.253 cm. Both cavities have a relative permittivity ε_r = 1 and the cavity heights are h_1 = 1.30 cm and h_2 = 0.444 cm. Each substrate board has a thickness t = 0.1524 cm and has a relative permittivity of ε_r = 2.5.

Table 3.4. Broadside directivity and power density for the initial dual-band structure.

Source	Frequency f_n (GHz) (n =1,2)	Directivity $D_n^{\max}$ (dB) (n =1,2)	Power density P_n^{rad} (W/m^2) (n =1,2)
1	12	30.98	0.11
2	18	25.74	1.30

From Table 3.4 it is observed that the broadside directivities at the two design frequencies are not equal, but differ by about 5 dB. The broadside power densities at the two design frequencies are also not equal. The E-plane radiation patterns of the initial design are given in Figure 3.13 and it can be seen that the beamwidths at the two design frequencies are not equal.

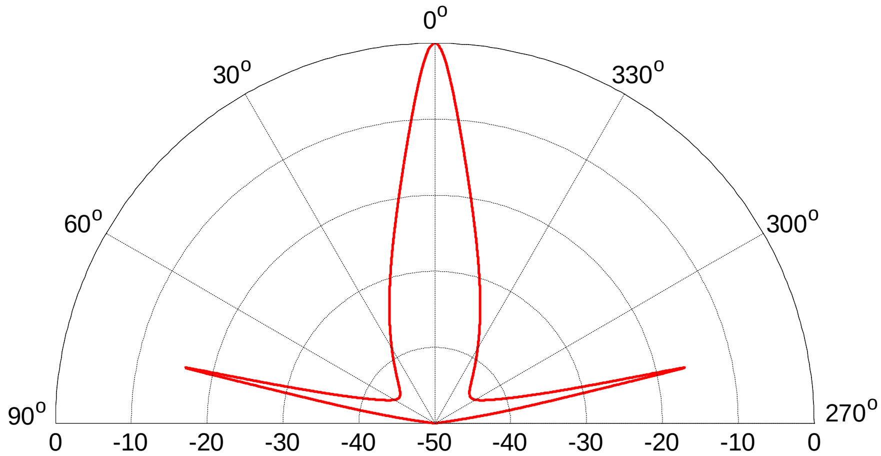

(a) 12 GHz

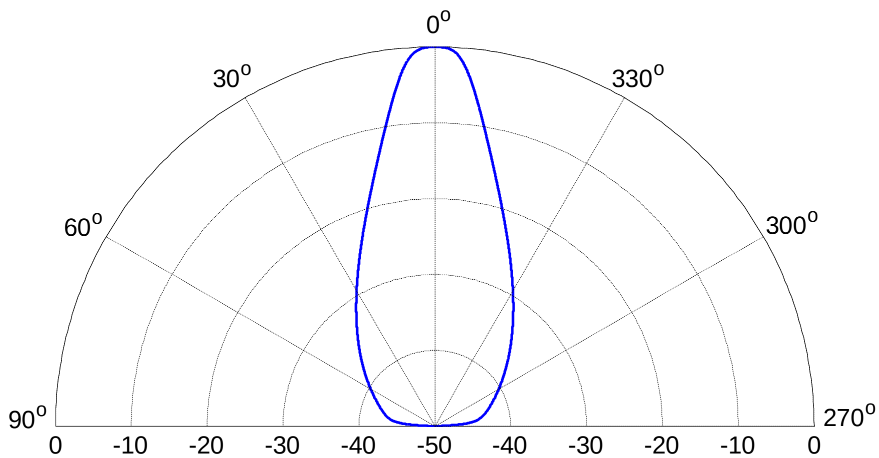

(b) 18 GHz

Figure 3.13. E-plane radiation patterns for the initial dual-band design with substrate boards.

3.5.2 Final Design

Using the iterative design process explained in sub-section 3.3.2, a final design for the practical structure in which the directivities as well as the broadside power densities are equal at the two specified design frequencies is obtained. Table 3.5 gives the values of the maximum broadside directivity as well as the power density radiated at broadside at the respective design frequencies for the final dual-band design with substrate boards. The PRS patch array dimensions are L_{PRS} = 1.160 cm, W_{PRS} = 0.928 cm, a_{PRS} = 1.253 cm and b_{PRS} = 0.278 cm. The FSS patch array dimensions are unaltered. The cavity heights are h_1 = 1.299 cm and h_2 = 0.439 cm.

Table 3.5. Broadside directivity and power density for the final dual-band structure.

Source	Frequency f_n (GHz) (n =1,2)	Directivity D_n^{max} (dB) (n =1,2)	Power density P_n^{rad} (W/m^2) (n =1,2)
1	12	31.53	0.19
2	18	31.51	0.19

The E-plane radiation patterns of the final design are given in Figure 3.14.

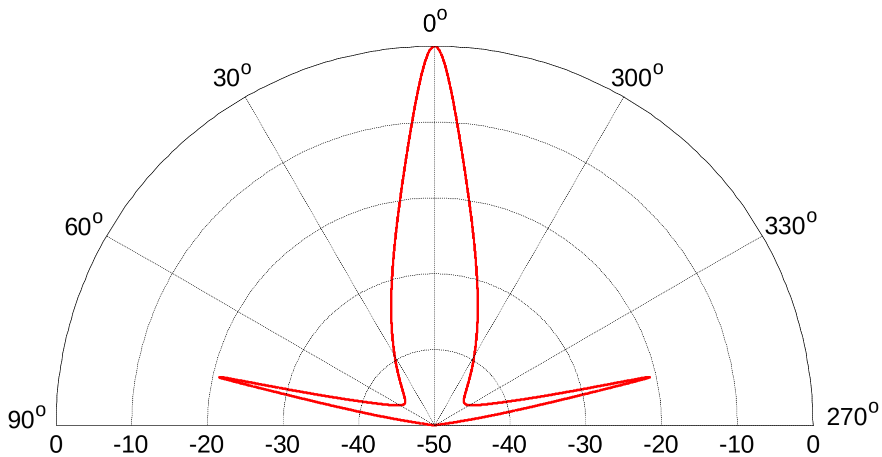

(a) 12 GHz

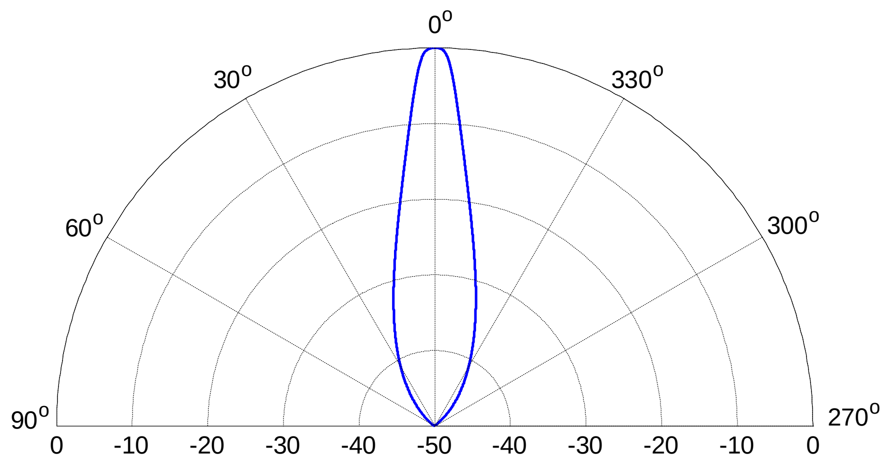

(b) 18 GHz

Figure 3.14. E-plane radiation patterns for the final dual-band design with substrate boards.

Though equal directivities at the two design frequencies are obtained in the final design, it is observed from Figure 3.14 that the E-plane pattern beamwidths are not equal. It is believed that this may be an effect of the presence of the substrate boards supporting the PRS and FSS layers.

3.6 Conclusion

In this chapter, a dual-band Fabry-Pérot resonant cavity antenna using an FSS layer inside the cavity was introduced. The first case that was considered was one where the PRS and FSS layers were suspended in air. A systematic design procedure based on the Transverse Resonance Equation (TRE) using the TEN model of the structure was proposed. From the initial results, it was found that the broadside directivities and power densities at the two chosen design frequencies were not equal. It was also seen that the E-plane patterns did not have equal beamwidths. An iterative method to optimize the design was given. The final design was seen to have equal broadside directivities and broadside power densities at the two specified frequencies. Optimized E-plane radiation patterns with equal beamwidths were also obtained. It was also found that the figure of merit at the two design frequencies for the dual-band structure were higher than those predicted by the CAD formula for a single air cavity PRS structure.

The second case studied was a dual-band structure in which the PRS and FSS layers were each placed on a 60 mil thick Arlon Diclad board. The PRS layer was chosen to be placed on the top surface of its substrate board while the FSS layer was placed on the bottom surface of its substrate board to facilitate the feeding of the upper cavity in future designs that will incorporate a practical printed dipole feed for the upper cavity. The design procedure based on the TRE and TEN model of the structure was again used to obtain an initial dual-band structure. The proposed iterative method was applied to the structure to obtain an optimized design in which the broadside directivities and power densities were equal. Radiation patterns with nearly equal directivities at the two design frequencies were obtained. A slight discrepancy between the beam shapes near the broadside region was found, and this is believed to be an effect of the substrate boards.

Chapter 4

Analysis of Truncated Dual-Band Structures

In this chapter, truncated versions of the dual-band structures proposed in Chapter 3 are studied using the EM software tool, Ansys Designer. A brief introduction is provided in Section 4.1. Section 4.2 deals with the various truncated structures for the dual-band air-cavity case where the PRS and FSS layers are suspended in air. The results obtained from Ansys Designer are compared to the previously obtained theoretical results. In Section 4.3, a practical truncated structure is studied where the PRS and FSS layers are each placed on substrate boards. Methods that attempt to improve the radiation pattern at the upper-dual band frequency are proposed. Section 4.4 provides some conclusions and comments on the proposed models.

4.1 Introduction

In the work presented in Chapter 3, we considered the 2-D arrays of metal patches that form the FSS and PRS layers to be infinitely large. However, for fabrication purposes, the structure would be required to be of finite size. In this chapter, we analyze truncated versions of the hypothetical dual-band air-cavity structure presented Section 3.2 of Chapter 3, along with the substrate-board case of Section 3.4. Here, truncated structures are designed to be 6 in × 6 in (15.24 cm x 15.24 cm) in size. This particular size for the truncated structures was considered as the goal since fabricating the truncated substrate-board dual-band design would be performed on a numerically controlled machine which has a vacuum table of size 6 in × 6 in.

4.2 Air-cavity Case: Truncated Structure

4.2.1 Decreasing PRS patch length

In order to choose an appropriate truncated dual-band structure to analyze in Ansys Designer, the final design of the air-cavity case structure discussed in Section 3.3.3 of Chapter 3 was first considered. This final design was found to have a directivity of about 36 dB at both design frequencies (12 and 18 GHz). For some practical applications, this directivity may be too high. So, in order to lower the directivity, the lengths of the original PRS patches were decreased by a certain percentage while the width and periodicity of the 2-D metal patch array were unaltered. The FSS was then designed to be a frequency scaled version of the shortened patches PRS such that it is resonant at the upper design frequency, 18 GHz. The iterative design method explained in Chapter 3 was then applied to the shortened PRS patch length structure, resulting in a final design with equalized directivities at both design frequencies.

Table 4.1 shows results for various directivities obtained by decreasing the PRS patch lengths by a certain percentage. The final design of the air-cavity case from Chapter 3 is also included and is denoted as the 0% decrease in PRS patch length case. The figure of merit is also calculated for each of these cases. It is observed that the figure of merit at either design frequency for all the cases is higher than that of an air filled single cavity Fabry-Pérot resonant cavity antenna.

Table 4.1. Broadside directivities and figures of merit at the two design frequencies for different PRS patch length cases.

Decrease in PRS patch length	Directivity at 12 GHz	Directivity at 18 GHz	Figure of merit at 12 GHz	Figure of merit at 18 GHz
0%	36.23	36.28	3.34	3.27
5%	30.84	30.80	3.69	3.17
15%	25.81	25.75	3.38	2.86
25%	21.28	21.38	3.03	2.51

4.2.2 Truncated Models

The results in Table 4.1 are for theoretically infinite structures. In order to simulate these structures in Ansys Designer version 15, they are truncated to a size of 6 in × 6 in. The general dual-band structure comprises of an infinite ground, a truncated FSS layer, and a truncated PRS layer, with air cavity regions between the layers. In Designer, the source excitations at the two design frequencies are modeled as strip dipoles. Each dipole is modeled to be a half-wavelength at its operating frequency. For the Designer simulations, the source dipoles are placed in the middle of their respective cavities.

Truncated versions of each of the cases of Table 4.1 were simulated in Designer, and their directive gain patterns at 12 GHz and 18 GHz were plotted. Figure 4.1 shows the E-plane directive gain patterns at the two design frequencies for the case where the PRS patch lengths are not altered (0% case). Here, the PRS is of size 13.42 cm × 14.81 cm, and its patch array dimensions are L_{PRS} = 1.391 cm, W_{PRS} = 0.111 cm, a_{PRS} = 1.503 cm and b_{PRS} = 0.334 cm. The FSS is of size 12.719 cm × 14.688 cm, and its patch array dimensions are L_{FSS} = 1.319 cm, W_{FSS} = 0.106 cm, a_{FSS} = 1.425 cm and b_{FSS} = 0.317 cm. Both cavities have a relative permittivity ε_r = 1, and the cavity heights are h_1 = 1.324 cm and h_2 = 0.824 cm.

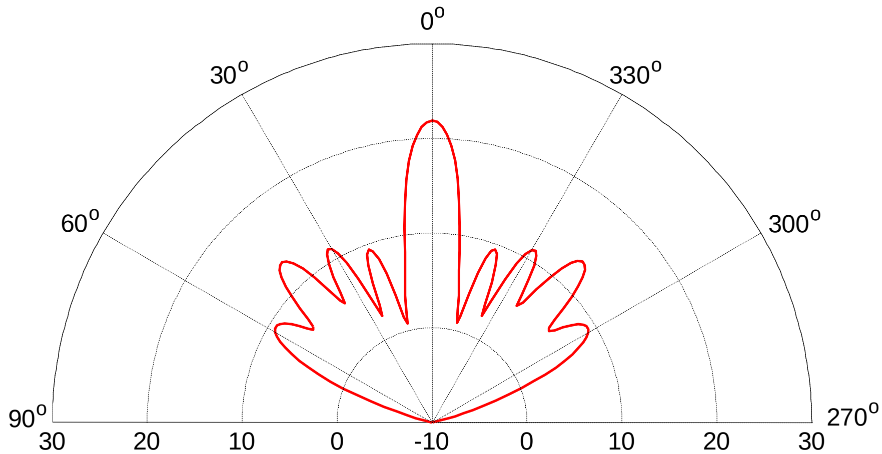

(a) 12 GHz

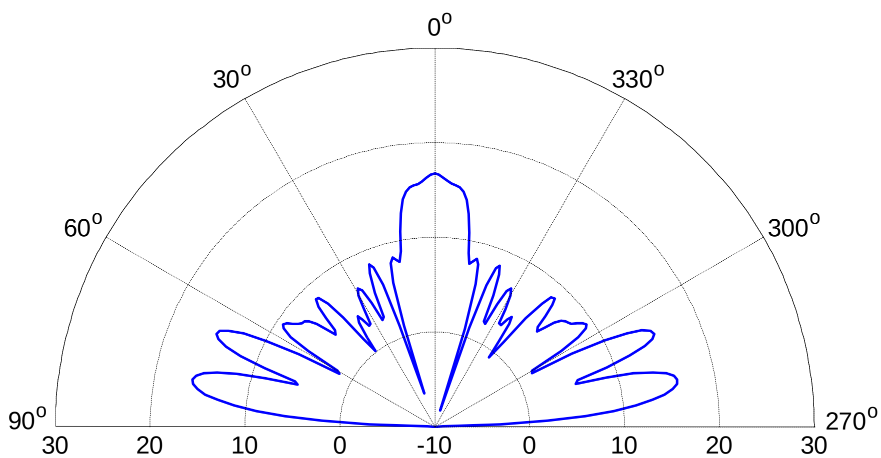

(b) 18 GHz

Figure 4.1. E-plane directive gain patterns obtained from Ansys Designer for the dual-band design case where the PRS patch lengths are not altered (0% case). The radial scale shows directivity (with respect to isotropic) in dB.

The broadside directive gain at 12 GHz is found to be 21.89 dB, and at 18 GHz it is 16.71 dB. From Figure 4.1, we may observe the presence of sidelobes in the directive gain pattern at both design frequencies, which is an effect of truncating the structure. Truncation of the structure is also the cause of the broadside directivities being much lower than what are obtained theoretically for the infinite structure, as given in Table 4.1.

The E-plane directive gain patterns for the 5% decrease in PRS patch length are given in Figure 4.2. The PRS is of size 14.51 cm × 14.92 cm, and its patch array dimensions are L_{PRS} = 1.173 cm, W_{PRS} = 0.099 cm, a_{PRS} = 1.334 cm and b_{PRS} = 0.296 cm. The FSS is of size 13.03 cm × 15.109 cm, and its patch array dimensions are L_{FSS} = 1.291 cm, W_{FSS} = 0.109 cm, a_{FSS} = 1.467 cm and b_{FSS} = 0.326 cm. Both cavities have a relative permittivity $\varepsilon_r = 1$, and the cavity heights are h_1 = 1.337 cm and h_2 = 0.849 cm.

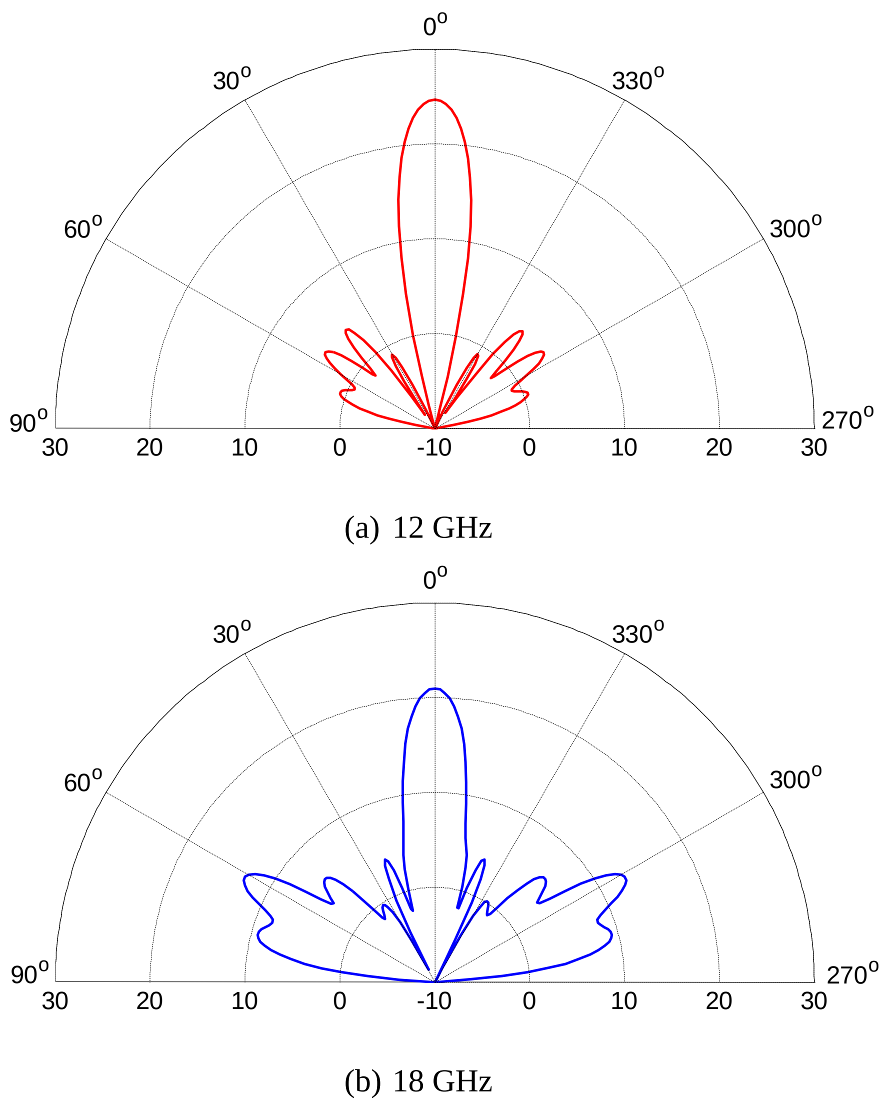

Figure 4.2. E-plane directive gain patterns obtained from Ansys Designer for the dual-band design case where the PRS patch length is decreased by 5%. The radial scale shows directivity (with respect to isotropic) in dB.

The broadside directive gains from the truncated structure were found to be 24.58 dB and 20.97 dB at 12 GHz and 18 GHz respectively, as opposed to its theoretically infinite counterpart, having a broadside directivity value of about 30.8 dB at both design frequencies.

The E-plane directive gain patterns for the 15% decrease in PRS patch length are given in Figure 4.3. The PRS is of size 14.68 cm × 15.22 cm, and its patch array dimensions are L_{PRS} = 1.071 cm, W_{PRS} = 0.101 cm, a_{PRS} = 1.361 cm and b_{PRS} = 0.302 cm. The FSS is of size 13.52 cm × 15.16 cm, and its patch array dimensions are L_{FSS} = 1.211 cm, W_{FSS} = 0.114 cm, a_{FSS} = 1.539 cm and b_{FSS} = 0.342 cm. Both cavities have a relative permittivity $\varepsilon_r = 1$, and the cavity heights are h_1 = 1.368 cm and h_2 = 0.861 cm.

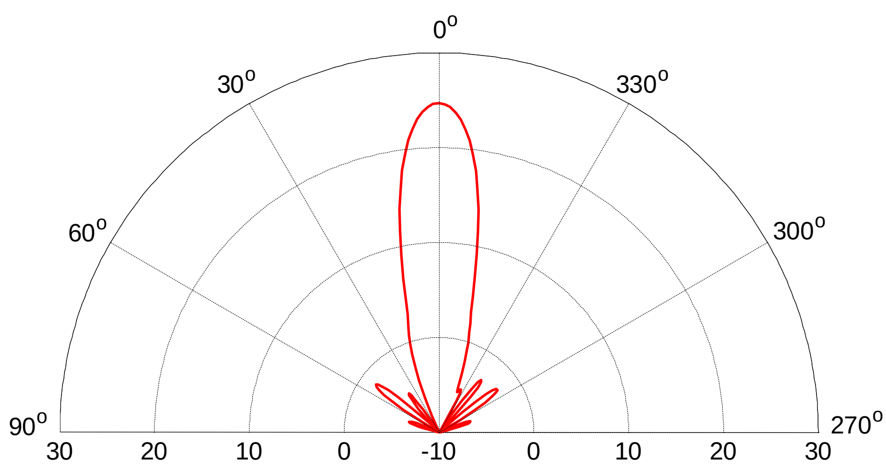

(a) 12 GHz

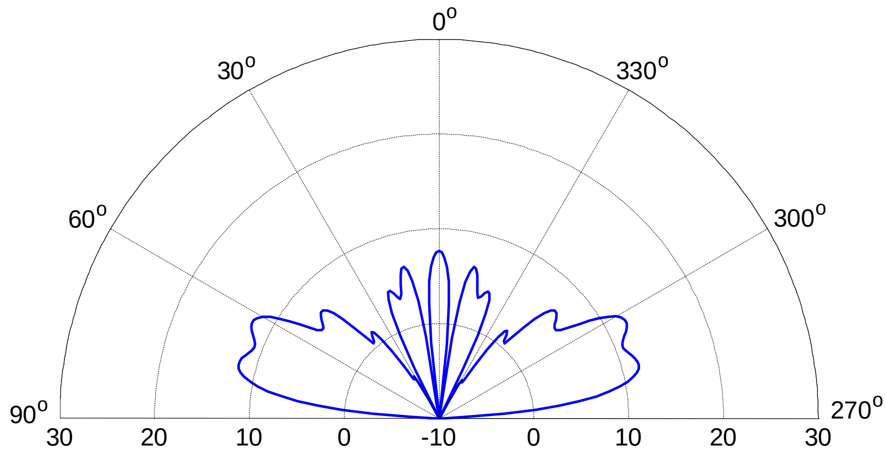

(b) 18 GHz

Figure 4.3. E-plane directive gain patterns obtained from Ansys Designer for the dual-band design case where the PRS patch length is decreased by 15%. The radial scale shows directivity (with respect to isotropic) in dB.

The broadside directive gains from the truncated structure were found to be 24.71 dB and 7.68 dB at 12 GHz and 18 GHz respectively.

In the 0% patch decrease case, we observe that there is a difference of about 5 dB in the directive gain at 12 GHz and 18 GHz. The difference in gain between that predicted for the infinite structure and that observed for the truncated structure (taking an average of the gains at 12 and 18 GHz) is about 17 dB.

In the 5% patch decrease case, we observe that there is a difference of about 3.5 dB in the directive gain at 12 GHz and 18 GHz. The difference in gain between that predicted for the infinite structure and that observed for the truncated structure (taking an average of the gains at 12 and 18 GHz) is about 8 dB. It is understandable that the directive gain obtained from the simulations at the dual-band frequencies of the truncated design is not as high as that obtained from the theoretically infinite model, since the radiating leaky wave that forms the directive beam is being truncated. Evidently the difference between the gains of the infinite and truncated structures is less for the 5% decrease case compared to the 0% decrease case because the leaky wave is attenuated more rapidly in the 5% decrease case, so that truncation effects are less important.

For the 15% patch length decrease case, we observe that a good pattern is obtained at 12 GHz, and the gain of the truncated case is only 1.1 dB lower than the gain of the corresponding infinite case. However, the pattern at 18 GHz is not reasonable and is nowhere close to what has been predicted theoretically in Table 4.1. As the FSS patch length is decreased (with unaltered periodicity), the sensitivity of the reflection coefficient at 18 GHz with respect to frequency increases, since the FSS only behaves as a short circuit for a frequency very near 18 GHz. This means that the FSS layer with the smaller patch lengths may not be behaving as a proper ground plane at the specified resonance frequency in Designer, due to numerical meshing errors. In order to overcome this issue, a hybrid model is proposed and its structure is explained in the next sub-section.

4.2.3 Hybrid Model

In order to overcome the frequency sensitivity issue of the FSS, a "hybrid" dual-band model is proposed. For the initial design of this model, the original PRS patch length is decreased by 15%, and the FSS is a frequency scaled version of the original PRS with patch length decrease of only 5%. The iterative design method then is applied to this hybrid design to equalize the directivities at the two design frequencies, and a plot of the broadside directivities versus frequency for the final design is given in Figure 4.4. The patch array dimensions are L_{PRS} = 1.114 cm, W_{PRS} = 0.105 cm, a_{PRS} = 1.415 cm and b_{PRS} = 0.314 cm. The FSS patch array dimensions are L_{FSS} = 1.291 cm, W_{FSS} = 0.109 cm,

a_{FSS} = 1.467 cm and b_{FSS} = 0.326 cm. Both cavities have a relative permittivity ε_r = 1, and the cavity heights are h_1 = 1.338 cm and h_2 = 0.853 cm.

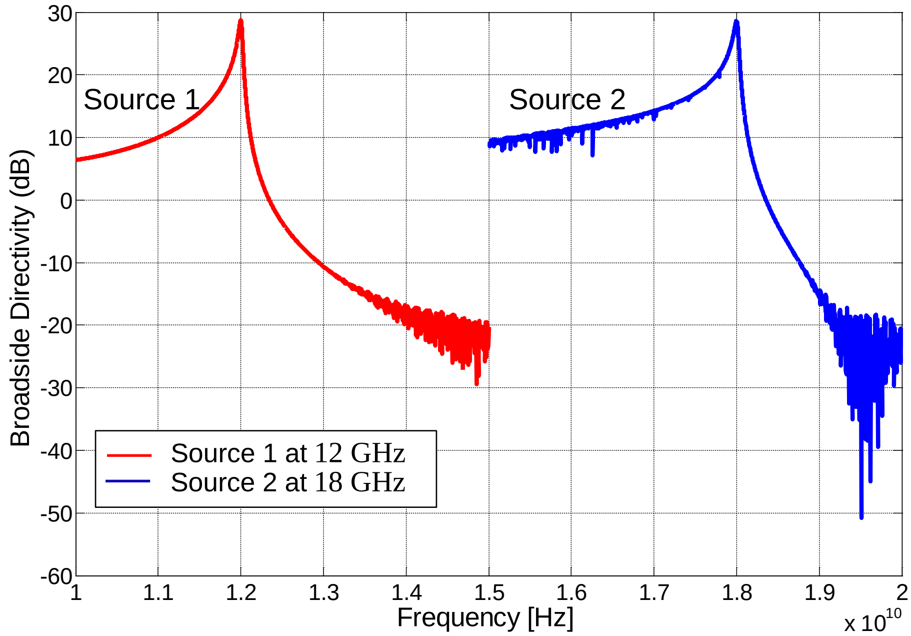

Figure 4.4. Broadside directivity vs. frequency for the infinite air-cavity hybrid dual-band design.

Table 4.2 gives the broadside directivities at 12 GHz and 18 GHz along with the figures of merit for the final design of the hybrid model.

Table 4.2 Broadside directivity and figure of merit for the final air-cavity dual-band hybrid design.

Source	Frequency f_n (GHz) (n =1,2)	Directivity $D_n^{\max}$ (dB) (n =1,2)	Figure of Merit
1	12	28.71	3.65
2	18	28.66	3.02

The E-plane patterns at the dual-band frequencies for the final design of the hybrid model are shown in Figure 4.5.

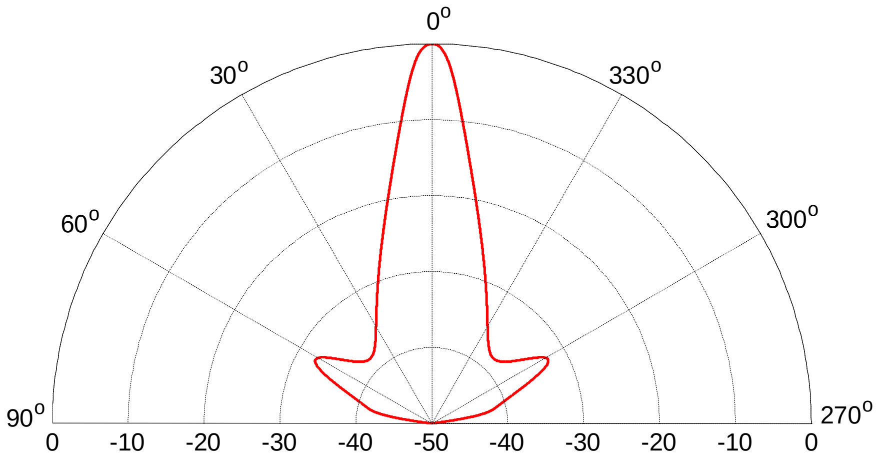

(a) 12 GHz

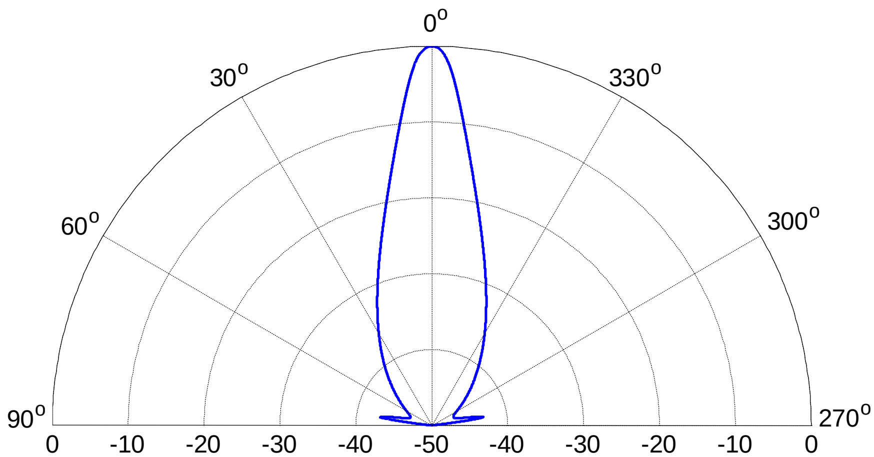

(b) 18 GHz

Figure 4.5. E-plane radiation patterns for the infinite air-cavity hybrid dual-band design.

From Figure 4.5, it is seen that equal beamwidths are obtained at the two design frequencies.

A truncated version of the final design of the hybrid model is simulated in Ansys Designer. The size of the PRS layer is of size 12.44 cm × 15.10 cm, and the FSS is of size

13.03 cm × 15.11 cm. Figure 4.6 shows the directive gain patterns obtained at 12 and 18 GHz.

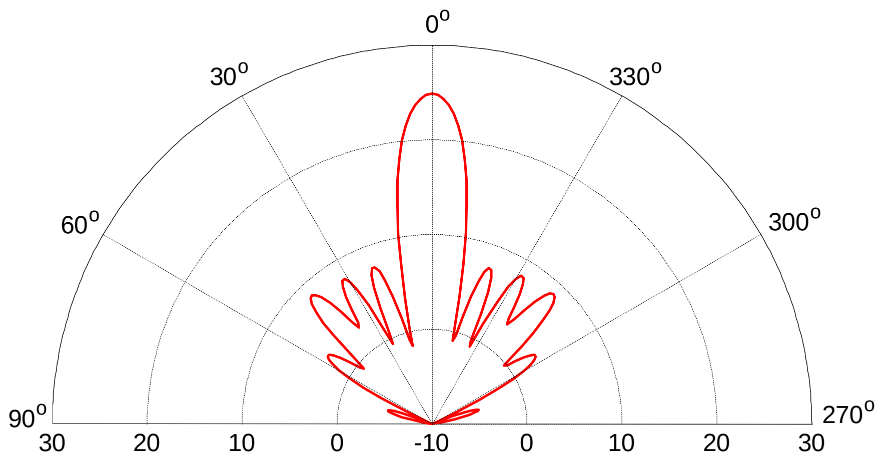

(a) 12 GHz

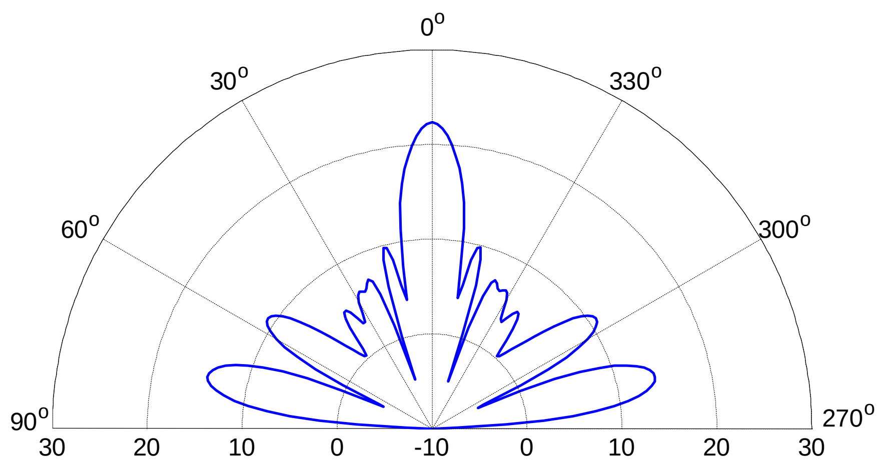

(b) 18 GHz

Figure 4.6. E-plane directive gain patterns obtained from Ansys Designer for the truncated hybrid dual-band design.

The directive gains were found to be 24.90 dB and 22.34 dB at 12 GHz and 18 GHz, respectively. It is also observed that there is approximately a 2.5 dB difference between the directive gains at 12 GHz and 18 GHz. Furthermore, the difference in gain between the infinite hybrid case and the truncated hybrid case (taking the average of the gains at the two frequencies) is about 5.1 dB.

It is believed that the difference in directivities at the two design frequencies is partly due to the fact that the PRS patch length obtained theoretically from the method of moments (used in the iterative design method) may be slightly different than what Designer recognizes as the appropriate resonant PRS patch length. In order to overcome this, a study that involves a tweaking of the PRS patch length was performed.

Figure 4.7 gives a plot of the difference in directivity ΔD at the two design frequencies versus the PRS patch length, for the truncated hybrid structure, obtained by Ansys Designer.

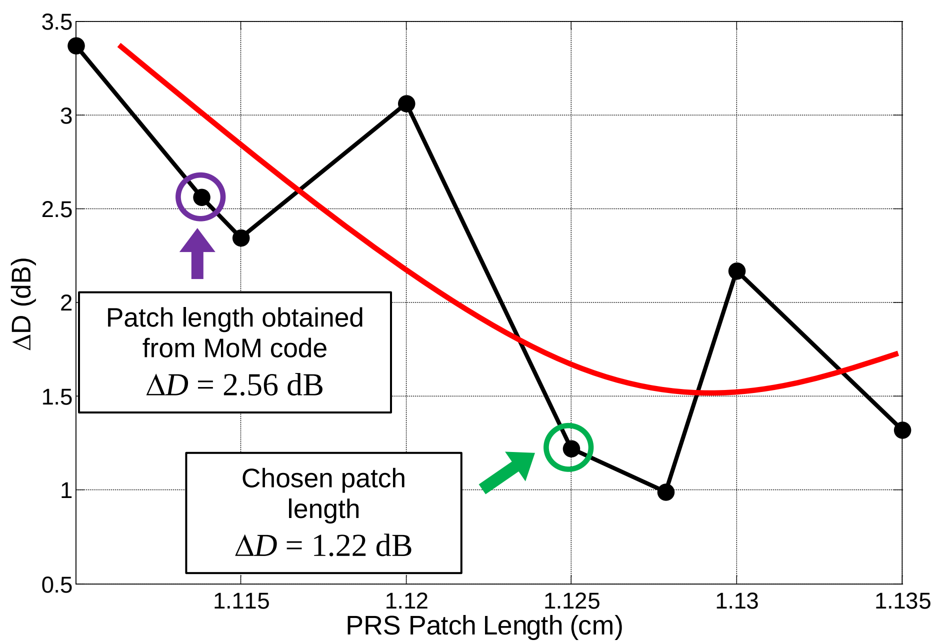

Figure 4.7. Difference in the directive gain (ΔD) at the two design frequencies vs. the PRS patch length for the truncated air-cavity hybrid dual-band design.

In Figure 4.7 the patch length that is obtained from MoM and the iterative method is circled in purple. This is the patch length that was used to obtain the theoretical results of Figure 4.5. A red curve is also included in the plot of Figure 4.7. This curve averages out the oscillations that are presumably due to numerical meshing noise. The location where the red curve has a minimum would roughly give the PRS patch length where we would expect the best solution. From the plotted points and red curve of Figure 4.8, a patch length of 1.125 cm is chosen as the PRS patch length, which gives us a difference of 1.22 dB in directive gain at the two design frequencies. The chosen PRS patch length is circled in green in the plot.

The directive gain plots at 12 GHz and 18 GHz obtained using the chosen PRS patch length of 1.125 cm in the truncated hybrid structure are given in Figure 4.8. All other dimensions of the PRS 2-D patch array are unaltered.

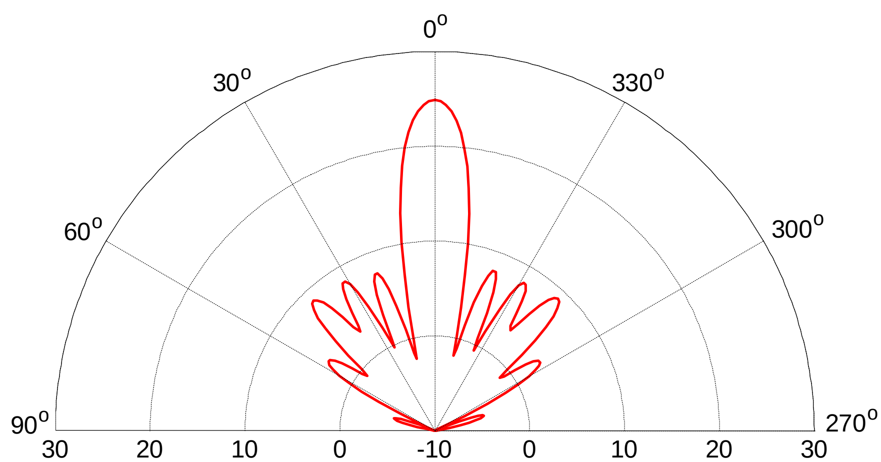

(a) 12 GHz

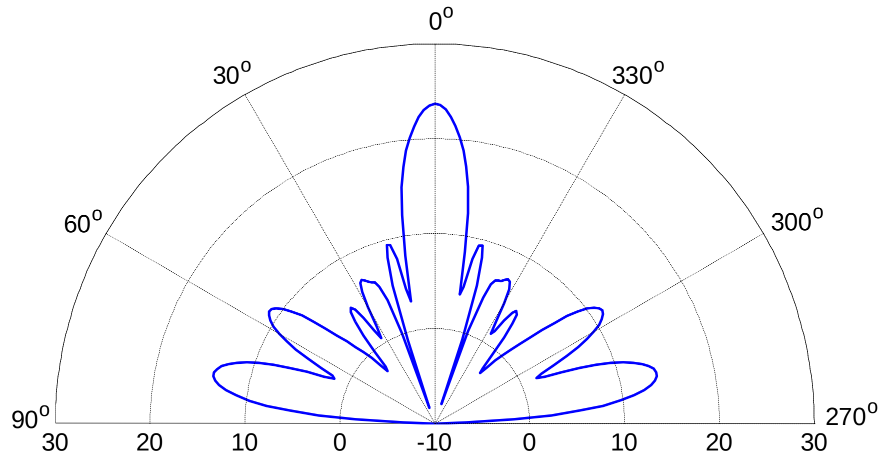

(b) 18 GHz

Figure 4.8. E-plane directive gain patterns obtained from Ansys Designer for the truncated air-cavity hybrid dual-band design with the length of the patches adjusted to L_{PRS} = 1.125 cm.

The directive gain at 12 GHz is 24.90 dB and at 18 GHz is 23.68 dB. Hence, the difference in the directive gain at the two design frequencies is lowered to about 1.2 dB with the new chosen PRS patch length. The difference in gain between the infinite hybrid case and the truncated hybrid case (taking the average of the gains at the two frequencies) is about 4.4 dB.

4.3 Substrate-Board Dual-Band Design: Truncated Structure

4.3.1 Ansys Designer Results

A truncated version of the substrate-board dual-band final design of sub-section 3.5.2 of Chapter 3 was simulated in Ansys Designer. In the truncated model the PRS and FSS structures are of finite size, while the substrate layers are infinite. The E-plane directive gain patterns at the two dual-band frequencies are given in Figure 4.9. The PRS is of size 13.69 cm × 15.13 cm, and its patch array dimensions are L_{PRS} = 1.160 cm, W_{PRS} = 0.093 cm, a_{PRS} = 1.253 cm and b_{PRS} = 0.279 cm. The FSS is of size 14.74 cm × 14.78

cm, and its patch array dimensions are L_{FSS} = 1.056 cm, W_{FSS} = 0.084 cm, a_{FSS} = 1.140 cm and b_{FSS} = 0.253 cm. Both cavities have a relative permittivity ε_r = 1, and the cavity heights are h_1 = 1.249 cm and h_2 = 0.439 cm. The thickness of the substrate boards are t = 0.157 cm, and the relative permittivity is $\varepsilon_r = 2.5$.

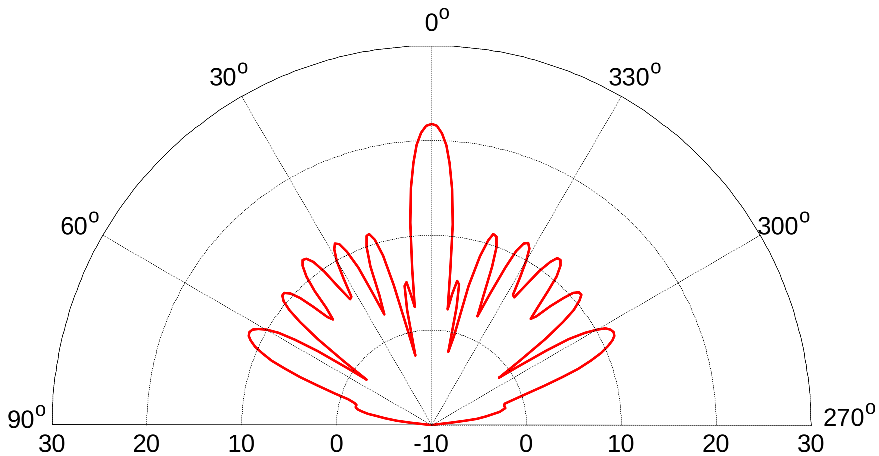

(a) 12 GHz

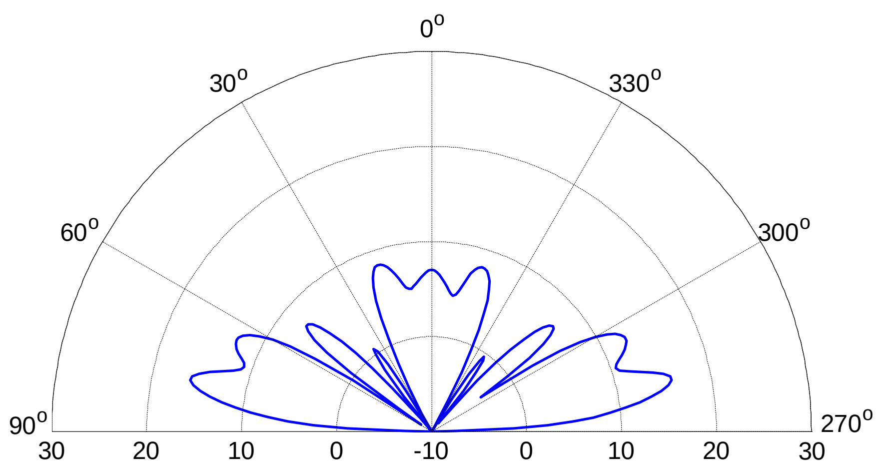

(b) 18 GHz

Figure 4.9. E-plane directive gain patterns obtained from Ansys Designer for the truncated substrate-board design.

From Figure 4.9 it can be observed that similar to the 15% PRS patch length decrease case shown in Figure 4.4, we obtain a good directive pattern at 12 GHz, but not one at 18 GHz. Here, the directive gain at 12 GHz is 21.77 dB and at 18 GHz it is 7.00 dB. In an attempt to increase the directive gain as well as improve the pattern at 18 GHz, a study on the FSS and PRS layers is conducted as described in the following sub-sections.

4.3.2 Optimization of the FSS Layer

The first concern that arises is that the FSS layer may not be optimized to have a resonance frequency at exactly 18 GHz, and in turn does not behave as a proper ground plane at this frequency. (This concern is what motivated the introduction of the hybrid model for the air-cavity case.) In order to ensure that the FSS has a resonance frequency of 18 GHz, a single FPCA is modeled in Designer having an infinite dielectric layer for the PRS that is a quarter-wavelength thick (wavelength meaning dielectric wavelength) at 18 GHz. At the bottom of the cavity, the substrate board is placed with the FSS on the bottom. Everything is therefore infinite except for the FSS, which is truncated and of size 14.74 cm × 14.78 cm. The thickness of the air cavity is chosen as explained below. For this structure it is known that the maximum radiated power density at broadside will occur when the lengths of the FSS patches are adjusted to get the best possible beam at 18 GHz. This in turn will give the best FSS design possible.

To choose the superstrate permittivity in the above mentioned single FPCA with an infinite dielectric layer (superstrate) PRS, we first start with an air-filled single FPCA having a given 2-D metal patch array PRS and conventional ground plane. The PRS chosen here is that of the hybrid model case of sub-section 4.2.3 as it is shown to work well in Designer. From this single cavity structure, the half-power beamwidth θ_w is found. From [52], we have

$$\theta_w = \frac{2}{\sqrt{a_1}} \ , \tag{4.1}$$

where

$$a_1 = \pi \frac{n_1 h}{\lambda_0} \left(\frac{\varepsilon_{r2}}{\varepsilon_{r1}} \right) \left(\frac{1}{n_1 \mu_{r2}} \right) \ , \tag{4.2}$$

$$n_1 = \sqrt{\varepsilon_{r1} \mu_{r1}} \ , \tag{4.3}$$

and

$$n_2 = \sqrt{\varepsilon_{r2} \mu_{r2}} \ . \tag{4.4}$$

Here ε_{r1} and μ_{r2} are the relative permittivity and relative permeability, respectively, of the air cavity. Similarly, ε_{r2} and μ_{r2} are the relative permittivity and relative permeability, respectively, of the superstrate layer. Hence, from θ_w, we may find the relative permittivity of the superstrate equivalent modelling the PRS of the conventional single FPCA design using Equations (4.1) and (4.2). As previously mentioned, the PRS superstrate layer is a quarter-wavelength thick at 18 GHz.

Before analyzing the new single FPCA design with a superstrate PRS and a substrate-backed FSS, the height of the air cavity must be calculated using the TRE to give an optimum beam at 18 GHz. Figure 4.10 shows the TEN of this design. At 18 GHz, we assume the FSS on the bottom side of the substrate board to be a short circuit. Here t_1 is the thickness of the substrate board, and t_2 is the thickness of the superstrate PRS. The air cavity height h is chosen from the TRE. Placing the reference plane R just below the superstrate, the TRE is

$$Y_{up} = -Y_{down}\,. \tag{4.5}$$

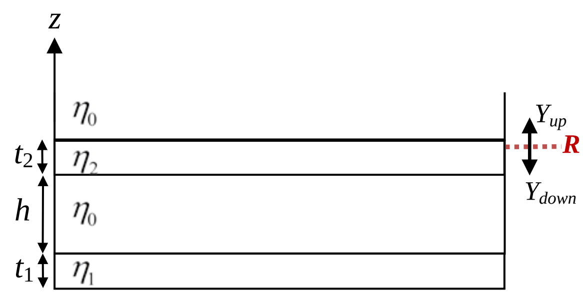

Figure 4.10. The TEN model to calculate the cavity height *h* at 18 GHz for the single FPCA design with a superstrate PRS and a substrate-backed FSS.

Since the superstrate is a quarter-wavelength thick, Y_{up} is purely real, and hence the imaginary part is zero. Working with the imaginary part and ignoring the real part of the admittance for the purposes of using the TRE to calculate the resonance condition, this implies that there is a short circuit at the reference plane location. We then shift the reference plane location to just below the air cavity as seen in Figure 4.11.

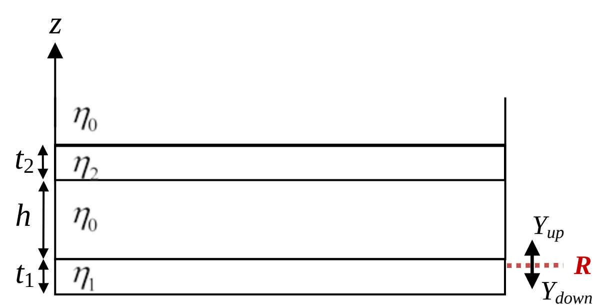

Figure 4.11. The TEN model with the TRE reference plane shifted in order to calculate the cavity height *h* at 18 GHz for the single FPCA design with a superstrate PRS and a substrate-backed FSS.

We then have

$$Y_{up} = -j\left(\frac{1}{\eta_0}\right)\cot\left(k_0 h\right) \tag{4.6}$$

and

$$Y_{down} = -j\left(\frac{1}{\eta_1}\right)\cot\left(k_1 t_1\right) \ . \tag{4.7}$$

From Equations (4.5), (4.6) and (4.7), the expression for the air cavity height h is found to be

$$h = \frac{1}{k_0}\cot^{-1}\left(-\frac{\eta_0}{\eta_1}\cot\left(k_1 t_1\right)\right) \ . \tag{4.8}$$

During the process of calculating the air cavity height, a half-wavelength at 18 GHz is added to the height of the air cavity to avoid higher-order Floquet mode interaction within the cavities.

Once the air cavity height is calculated, the single-cavity FPCA design with a superstrate PRS and a substrate-backed FSS is modeled in Designer, and the cavity is excited with a dipole in the middle. Figure 4.12 shows the E-plane directive gain pattern of this structure at 18 GHz prior to adjusting the lengths of the FSS patches. Here the FSS is of size 14.74 cm × 14.74 cm, and its patch array dimensions are L_{FSS} = 1.056 cm, W_{FSS} = 0.084 cm, a_{FSS} = 1.140 cm and b_{FSS} = 0.253 cm. The thickness of the substrate board is t_1 = 0.157 cm, and its relative permittivity $\varepsilon_{r2} = 2.5$. The height of the air cavity h = 0.644 cm, and its relative permittivity $\varepsilon_r = 1$. The thickness of the superstrate PRS is t_2 = 0.028 cm, and its relative permittivity $\varepsilon_{r2} = 221.75$.

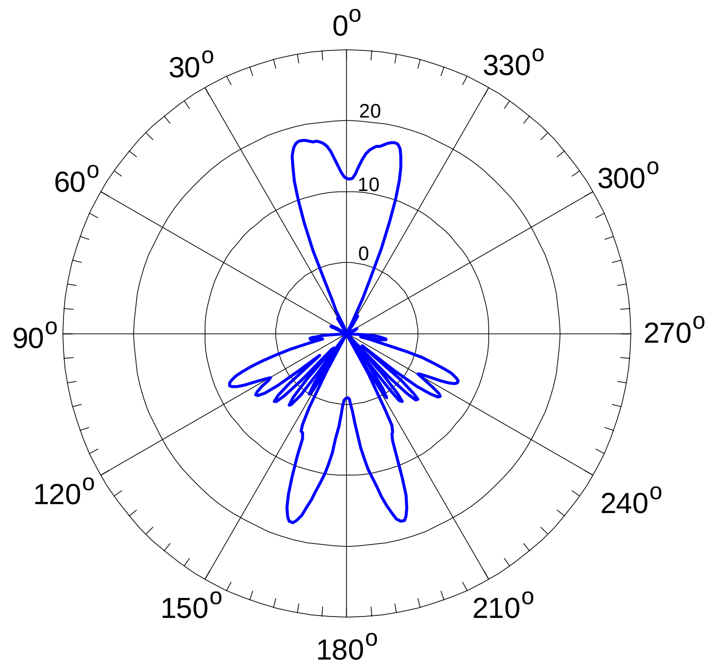

Figure 4.12. E-plane directive gain pattern at 18 GHz obtained from Designer for a single cavity FPCA with a superstrate PRS. L_{FSS} = 1.056 cm.

In Figure 4.12, we observe that the FPCA structure does not produce a broadside directive beam at 18 GHz. This implies that the FSS layer does not behave as a proper ground plane, and hence does not have a resonance frequency at 18 GHz as it should. In order to ensure a good ground plane behavior at 18 GHz, the lengths of the FSS patches are slightly altered. Through trial and error, it was found that by decreasing the FSS patch lengths by 5%, an optimum beam shape and a high directive gain is obtained as shown in Figure 4.13. Here, L_{FSS} = 1.003 cm while all other dimensions are unaltered.

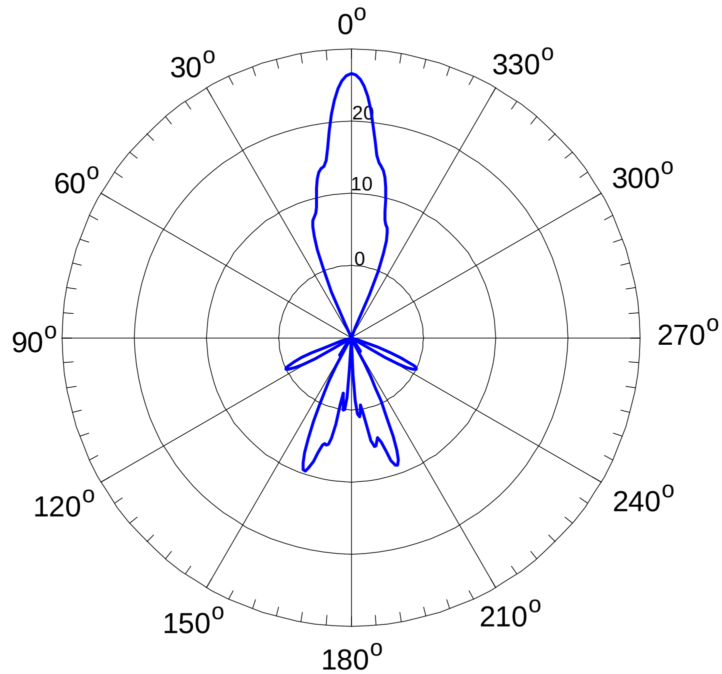

Figure 4.13. E-plane directive gain pattern at 18 GHz obtained from Designer for a single cavity FPCA with a superstrate PRS. L_{FSS} = 1.003 cm.

The optimized FSS layer is then placed in the truncated substrate-board dual-band design, and the E-plane directive gain patterns at the dual-band frequencies are shown in Figure 4.14.

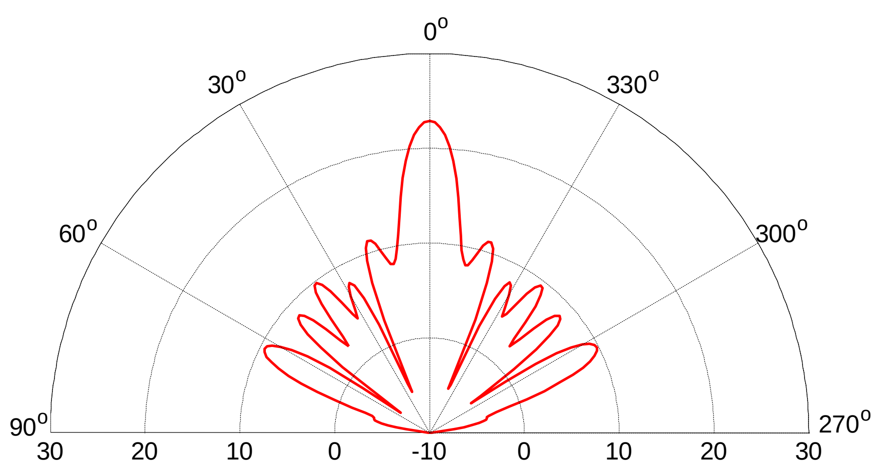

(a) 12 GHz

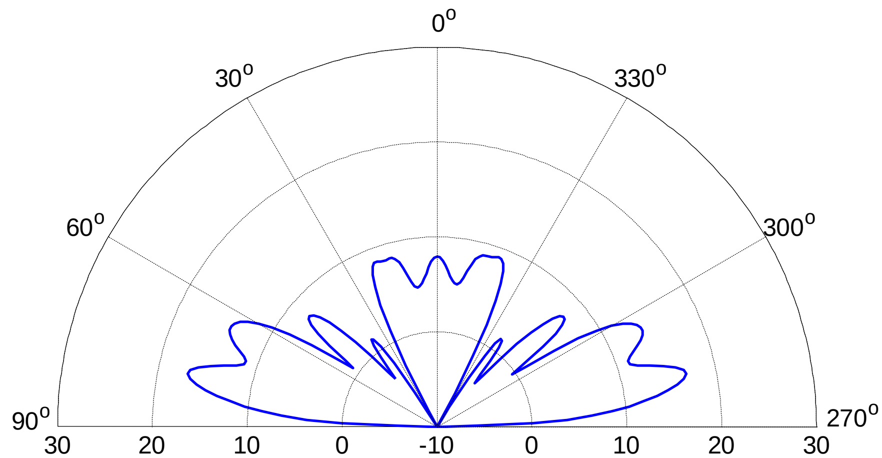

(b) 18 GHz

Figure 4.14. E-plane directive gain patterns obtained from Ansys Designer for the truncated substrate-board design with an optimized FSS layer. L_{FSS} = 1.003 cm.

With the optimization of the FSS layer, the directive gain at 12 GHz is now 22.92 dB and at 18 GHz, it is 7.95 dB. It is observed that with the optimized FSS layer, though there is a slight enhancement in the directive gain at both design frequencies, we still do not obtain an improvement in the pattern at 18 GHz. Evidently then, the frequency sensitivity of the FSS layer is not the only source of trouble in the substrate-board truncated design at 18 GHz.

4.3.3 Optimization of the PRS Layer

Since no significant improvement was found with the optimization of the FSS layer alone, the optimization of the 2-D metal patch array PRS layer of the truncated substrate-board dual-band design is considered next. The procedure to optimize the PRS layer is identical to that used for the FSS, but the procedure is now performed at the resonance frequency of the PRS. From the spectral-domain MoM and the calculation of the B_s of the PRS, the resonance frequency of the PRS layer was found to be 16.54 GHz. The single FPCA with a superstrate PRS is designed at this resonance frequency using the TRE. The superstrate PRS is now a quarter-wavelength thick at 16.54 GHz, but has the same relative permittivity as that calculated in the previous subsection. It is important to note that the 2-D metal patch array PRS replaces the FSS layer on the bottom side of the substrate board in the previous FSS optimization study, to act as a finite ground plane at its resonance frequency. The lengths of the PRS patches are adjusted to get the best possible beam at 16.54 GHz.

The E-plane directive gain pattern obtained in Designer of the single-cavity FPCA design before the PRS patch lengths are adjusted is shown in Figure 4.15. Here the finite ground plane PRS is of size 13.69 cm × 15.13 cm, and its patch array dimensions are L_{PRS} = 1.160 cm, W_{PRS} = 0.093 cm, a_{PRS} = 1.253 cm and b_{PRS} = 0.279 cm. The thickness of the substrate board is t_1 = 0.157 cm, and its relative permittivity $\varepsilon_{r_1} = 2.5$. The height of the air cavity h = 0.906 cm, and its relative permittivity $\varepsilon_r = 1$. The thickness of the superstrate PRS is t_2 = 0.030 cm, and its relative permittivity $\varepsilon_{r_2} = 221.75$.

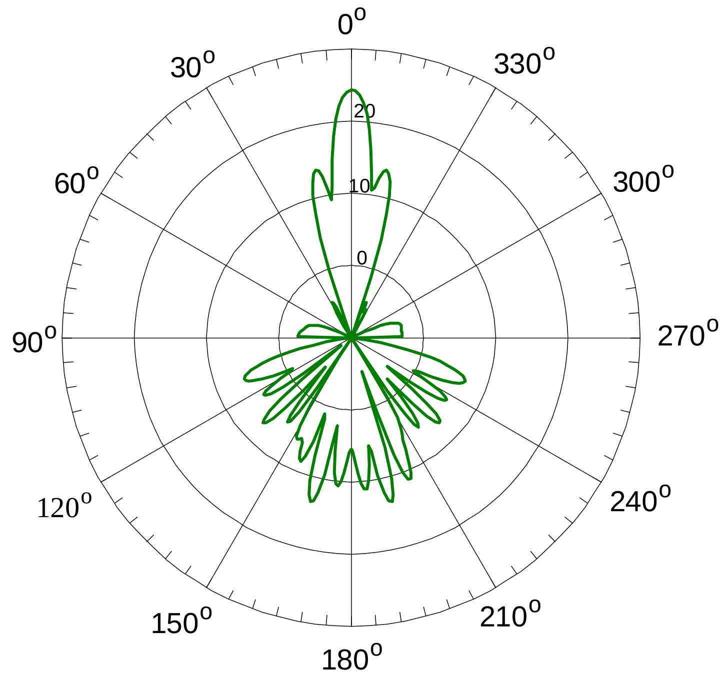

Figure 4.15. E-plane directive gain pattern at 16.54 GHz obtained from Designer for a single cavity FPCA with a superstrate PRS and a finite 2-D patch array PRS as the ground plane. L_{PRS} = 1.160 cm.

From Figure 4.15, we see that a reasonably good pattern is obtained with a directivity of 24.39 dB. However, we may observe that the main beam has quite large “shoulder” lobes. In an effort to obtain a better broadside beam with smaller shoulder lobes, a systematic trial and error approach adjusting the PRS patch length size is performed. It is found that decreasing the PRS patch length by 5% results in a more optimum beam shape. The E-plane directive gain pattern at 16.54 GHz after the patch length adjustment is shown in Figure 4.16. Here L_{PRS} = 1.102 cm while all other dimensions are unaltered.

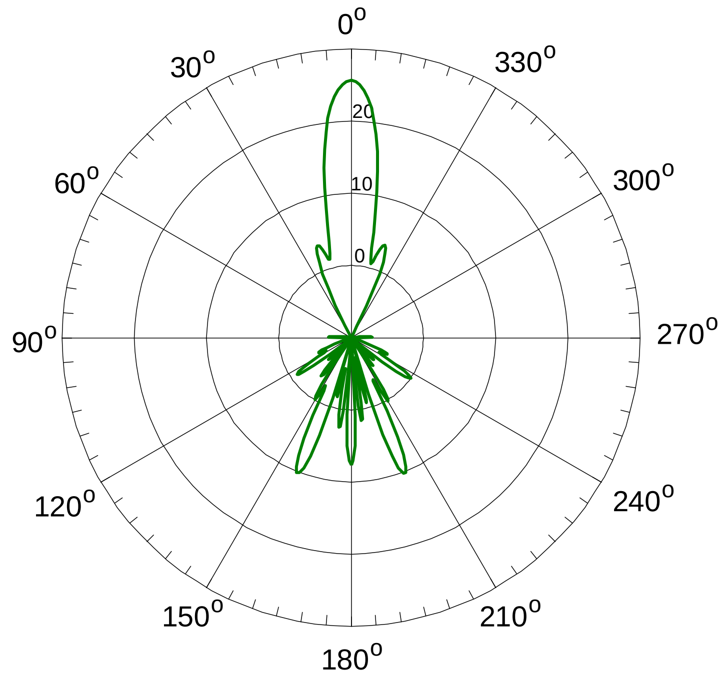

Figure 4.16. E-plane directive gain pattern at 16.54 GHz obtained from Designer for a single cavity FPCA with a superstrate PRS and a finite 2-D patch array PRS as the ground plane. L_{PRS} = 1.102 cm.

From Figure 4.16, we see that the main beam is improved with lower shoulder lobes. The directive gain is 25.66 dB. The optimized FSS and PRS layers are placed in the truncated substrate-board structure, and the E-plane patterns at the dual-band frequencies are shown in Figure 4.17.

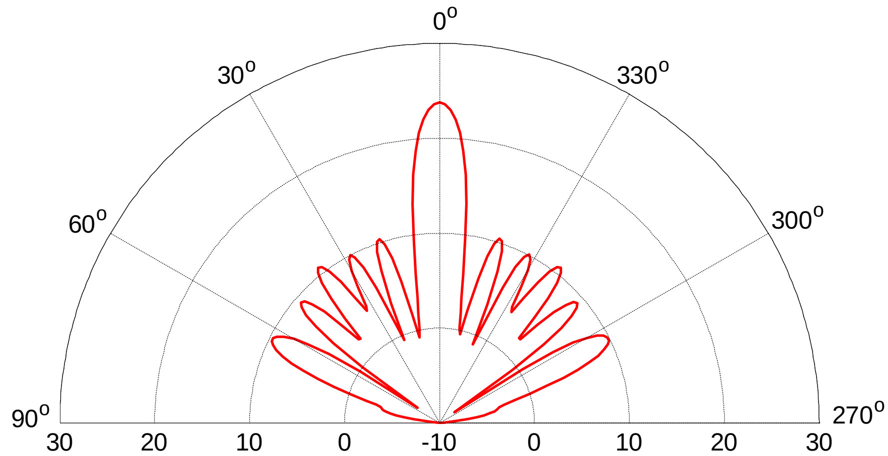

(a) 12 GHz

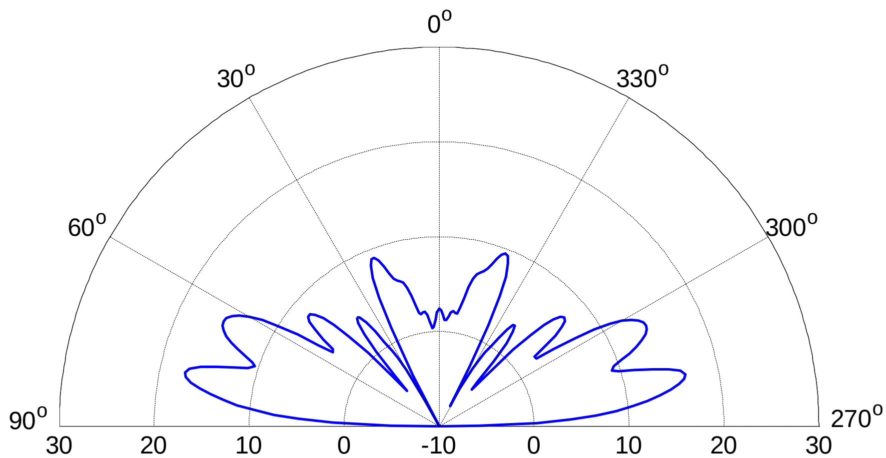

(b) 18 GHz

Figure 4.17. E-plane directive gain patterns obtained from Ansys Designer for the truncated substrate-board design with optimized FSS and PRS layers. L_{FSS} = 1.003 cm and L_{PRS} = 1.102 cm.

From Figure 4.17 we may see that though both the FSS and PRS layers are now optimized, there is still no significant improvement in the pattern at 18 GHz.

4.3.4 Increasing Upper Air Cavity Height

Since it was found that optimization of the FSS and PRS layers alone did not improve the directive gain pattern at 18 GHz, a study on the cavity height was performed. As previously mentioned, the height of the upper air cavity is h_2 = 0.439 cm. It was thought that this cavity height may be too small and may be causing higher order Floquet mode interaction to occur, resulting in a distorted pattern at 18 GHz. Hence, increasing the upper cavity height h_2 may overcome this problem and improve the directive gain pattern. Hence, an extra half-wavelength at 18 GHz was added to the upper cavity height of the structure (with optimized FSS and PRS layers) and the planar dipole source in the cavity was placed at a distance of a quarter wavelength (at 18 GHz) from the FSS layer. The E-plane directive gain patterns at the two design frequencies are given in Figure 4.18. Here L_{PRS} = 1.102 cm, L_{FSS} = 1.003 cm and h_2 = 1.277 cm, while all other dimensions are unaltered.

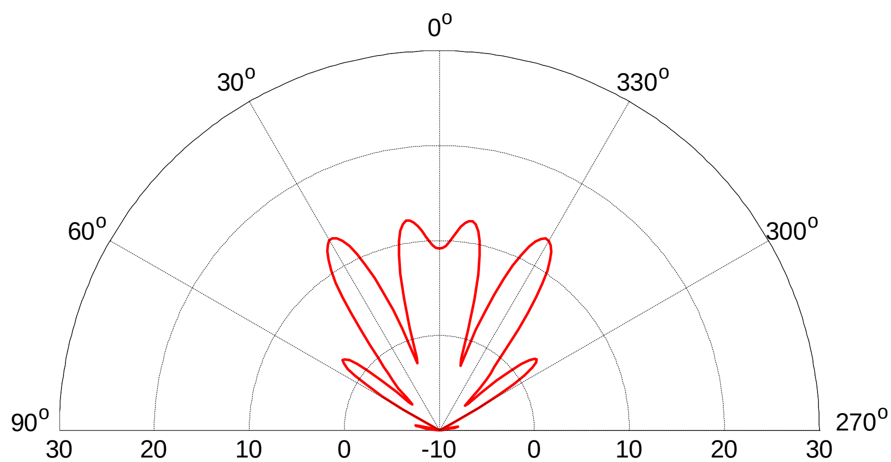

(a) 12 GHz

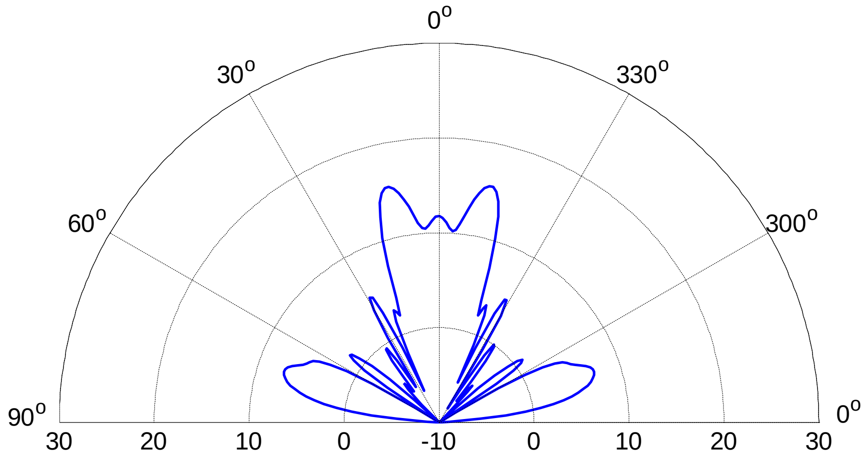

(b) 18 GHz

Figure 4.18. E-plane directive gain patterns obtained from Ansys Designer for the truncated substrate-board design with optimized FSS and PRS layers and an increased upper cavity height. L_{FSS} = 1.003 cm, L_{PRS} = 1.102 cm and h_2 = 1.277 cm.

From Figure 4.18, the broadside directive gain at 18 GHz is found to be 11.80 dB, which is a slight improvement from the previously obtained value. However, an optimum broadside beam shape is still not achieved. Also, it is observed that the 12 GHz directive gain pattern is adversely affected by the increase in the height of the upper cavity and the broadside directive gain is lowered to a value of 9.25 dB. Since an increase in the upper cavity height does help to obtain optimum equalized directive gain patterns at the two design frequencies, it can be concluded that the presence of higher order Floquet wave interaction was not responsible for the trouble with the truncated substrate-board design.

4.3.5 Presence of Surface Waves

After performing the tests of the previous sub-sections and careful consideration, it is believed that the problem causing the distorted directive gain pattern at 18 GHz for the truncated dual-band substrate-board case is the presence of more than just the radially-propagating leaky wave. The possibility of the presence of either space waves or surface waves is considered. Let us first consider the possibility of the presence of a space wave. If a significant space wave was present in the structure, then this would have been observed in the form of a bulbous shape in the E-plane radiation patterns for the infinite structure. However, it can be seen that no such shape occurs in the pattern of the infinite structure. This leads us to believe that the cause for the distorted radiation patterns is due to the presence of a surface wave in the truncated structure. Surface waves radiate power from discontinuities in a structure that interrupt the surface wave on the structure [53]. Here, in the dual-band truncated substrate-board design, the truncation of the boards and metal patches of the PRS and FSS layers serve as discontinuities. It is speculated that the planar dipole source in the upper cavity launches a surface wave and this launched surface wave encounters the truncated substrate board and metal patch discontinuities and thus bounces around inside the structure. This leads to radiation from the edges of the structure and from the patches, and in turn causes the distorted pattern at 18 GHz.

In order avoid surface waves, it is proposed as future work to base the substrate-board dual-band design on that of the hybrid model truncated air-cavity design of sub-section 4.2.3. In the hybrid model, it was observed that though the structure was truncated, the radiation patterns were not distorted. This implies that only radially propagating leaky waves were present in that structure. Hence, in order to avoid surface waves in the truncated substrate-board structure, it would be required to mimic the hybrid model air-cavity case by replacing the Arlon Diclad 527 substrate boards with supporting boards that have a relative permittivity very close to air. It is proposed to use a phenolic honeycomb material namely, HexWeb HRH – 10 as the supporting boards for the PRS and FSS metal patch layers. The advantage of this material is that extremely thin boards with high strength are readily available and are damage resistant under normal use. Another added advantage of this material is that its relative permittivity is very close to that of air. It is proposed to first etch the 2-D metal patch arrays of the PRS and FSS layers on thin laminate sheets, and then place these layers on the HexWeb HRH – 10 boards which would act as a means of support for these layers. The dual-band design procedure using the TEN and TRE would then be repeated and the iterative design procedure would then be applied to this new structure in an attempt to obtain optimized patterns at the dual-band frequencies.

4.4 Conclusion

In this chapter a truncated version of the proposed dual-band Fabry-Pérot resonant cavity antenna was analyzed using Ansys Designer. The effect of a decrease in PRS patch length on the broadside directivity was first studied, and the directive gain patterns were presented. A hybrid model was proposed in which the broadside directive gains obtained from Designer are nearly equal at the two design frequencies.

The truncated structure was then extended to a substrate-board design in which the PRS and FSS layers are placed on the surfaces of their respective supporting substrate boards. A good directive gain pattern was observed at 12 GHz, but not at 18 GHz. In an effort to improve the pattern at 18 GHz, the PRS and FSS layers were optimized by tweaking their patch lengths. It was found that this did not improve the pattern at 18 GHz. In a final attempt, an extra half-wavelength was added to the upper cavity of the structure. This resulted in a slightly improved pattern at 18 GHz, but lead to a detrimental effect on the pattern at 12 GHz.

After the series of tests, it is believed that the distorted pattern at 18 GHz occurs due to the presence of a surface wave on the substrate boards, which contaminates the leaky-wave on the structure. To overcome this problem, it is proposed as future work to use a phenolic honeycomb material in place of the Arlon Diclad boards as the supporting boards for PRS and FSS layers. The iterative design procedure would then be applied to this new structure in an attempt to obtain optimized radiation patterns at the two design frequencies.

Chapter 5

Conclusion

5.1 Conclusion

In this dissertation, a dual-band version of the Fabry-Pérot resonant cavity antenna (FPCA) was proposed. The structure uses a frequency selective surface (FSS) patch layer over a ground plane to form a composite artificial ground plane that replaces the single metal ground plane of the conventional structure.

A brief literature review in the advances of Fabry-Pérot structures was presented in Chapter 1. A conventional single-cavity Fabry-Pérot antenna was studied in Chapter 2. The method of calculating the far-field using reciprocity and the spectral-domain periodic moment method was explained in detail. The procedure for the calculation of the shunt susceptance that models the PRS layer in the TEN, and the calculation of the air cavity height using the TRE were provided. The comparison of the E-plane radiation patterns at 12 GHz and 18 GHz using the spectral-domain periodic moment method and the TEN were shown, and the agreement was very good.

The structure was then extended to one where the PRS layer was placed on a 60 mil Arlon Diclad 527 board. Two different cases based on the location of the PRS layer on the substrate board (on the top or bottom surface) were presented. A comparison of the E-plane radiation patterns using the aforementioned two methods was given, and it was speculated that the value of the shunt susceptance modelling the PRS layer in the TEN is required to be dependent on the incident angle to obtain good agreement between the patterns for the substrate-board case.

In Chapter 3, the proposed dual-band structure was presented. A structure using air cavities was first introduced. The structure consists of an upper cavity region (between an FSS and the PRS) and a lower cavity region (between the ground plane and the FSS). The main design principle of this dual-band Fabry-Pérot resonant cavity antenna is that the FSS layer in the structure has a resonance frequency at which it acts as a short circuit and hence behaves as a "virtual ground plane" at that frequency. The FSS is chosen so that at the upper-band frequency it behaves as a short circuit, and hence the upper cavity resonates at this frequency and behaves just as a regular single-cavity FPCA would at this frequency. At the lower-band frequency the entire composite cavity (the region between the ground plane and the PRS) resonates. A systematic procedure to obtain dual-band behavior was explained, and an iterative method to obtain optimum beam shapes and equal directivities as well as equal radiated broadside power densities at the two specified design frequencies was provided. The dual-band design was then extended to one where the PRS and FSS layers are placed on substrate boards. This design was studied, and an optimization of its E-plane radiation patterns at the two design frequencies was discussed.

In Chapter 4, truncated versions of the optimized dual-band structures of Chapter 3 were analyzed using the commercial EM software simulation tool Ansys Designer. The truncated air-cavity case was studied first. A method to obtain lower broadside directivities by decreasing the PRS patch lengths was explained. This was important since having too high of a directivity would result is too much of the leaky wave being reflected at the edges of the truncated structure, and this in turn would result in too much of a disparity between the infinite and truncated results. On the other hand, increasing the FSS patch length allows the FSS to be less sensitive to frequency variations that might be introduced by numerical meshing error in Ansys Designer. A hybrid design was thus introduced, where the PRS patch length was decreased by 15% while the FSS patch length was increased by 5% relative to the previous design. The hybrid design achieved nearly equal directivities (to within about 1.2 dB) at the two design frequencies of 12 and 18 GHz for the truncated structures after optimization of the PRS patch length.

The simulations were then performed on the truncated version of the optimized substrate-board dual-band design. It was found that a directive gain pattern was only obtained at 12 GHz. In an effort to improve the pattern at 18 GHz, an optimization of the PRS and FSS layers was performed along with the addition of an extra half-wavelength to the upper air cavity. However, it was found that these efforts did not improve the pattern at 18 GHz. It is believed that the distorted pattern at 18 GHz occurs due to the presence of a surface wave on the substrate boards, which contaminate the desired leaky-wave on the structure. To overcome this problem, it is proposed as future work to use a phenolic honeycomb material in place of the Arlon Diclad boards as the supporting boards for PRS and FSS layers. The iterative design procedure would then be applied to this structure in an attempt to obtain optimized radiation patterns at the two design frequencies for the truncated structure.

5.2 Future Work

As previously mentioned, it is proposed as future work to use the material HexWeb HRH – 10 as the supporting boards for the PRS and FSS layers in the truncated substrate-board dual-band structure. Once the structure is analyzed with the new material, it proposed to implement practical feed structures within the truncated dual-band design. A possible feeding method would be to place a microstrip patch antenna on the ground plane of the structure to feed the lower cavity at 12 GHz. The upper cavity could be fed at 18 GHz by a planar dipole printed on the top surface of the board supporting the FSS layer. This truncated structure with the practical feeds could be analyzed using Ansys Designer and HFSS.

As mentioned in Chapter 4, the main motivation behind analyzing a truncated structure of size 6 in $\times$ 6 in with Ansys Designer is the fabrication of a practical dual-band structure. Once the implementation of the new supporting boards along with the practical feed structures are analyzed using Ansys Designer and HFSS, and optimized patterns at the dual-band frequencies are obtained, it is proposed to fabricate this dual-band structure. In order to do this, we propose to collaborate with the Applied Electromagnetics Laboratory of the University of Manitoba in Winnipeg, Canada. The fabrication of the antenna along, with measurements of it, would take place at this laboratory and the measured results would be compared to those obtained from simulations.

References

[1] A. Hessel, “General Charactersitics of Traveling-Wave Antennas,” Chapter 19 of *Antenna Theory, Part 2*, Ed.; R. E. Colin and F. J. Zucker, New York, McGraw-Hill, 1969.

[2] T. Tamir, “Leaky-Wave Antennas,” Chapter 20 of *Antenna Theory, Part 2*, Ed.; R. E. Colin and F. J. Zucker, New York, McGraw- Hill, 1969.

[3] D. R. Jackson and A. A. Oliner, “Leaky-Wave Antennas,” Chapter 7 of *Modern Antenna Handbook*, Hoboken, C. Balanis, Editor, John Wiley & Sons, Inc., 2008.

[4] A. A. Oliner and D. R. Jackson, “Leaky-Wave Antennas,” Chapter 11 of *Antenna Engineering Handbook*, Ed.; R. C. Johnson, McGraw-Hill, 2007.

[5] L. O. Goldstone and A. A. Oliner, “Leaky-wave antennas - Part I: Rectangular waveguides,” *IRE Trans. Antennas Propagat.*, vol. 7, pp. 307–319, Oct. 1959.

[6] A. Ip and D. R. Jackson, “Radiation from cylindrical leaky waves,” *IEEE Trans. Antennas Propagat.*, vol. 38, pp. 482–488, Apr. 1990.

[7] D. R. Jackson, C. Caloz, and T. Itoh, “Leaky-Wave Antennas,” *Proceedings of the IEEE*, special issue on Antennas in Wireless Communications, K. M. Luk and K. F. Lee, Editors, vol. 100, No. 7, pp. 2194-2206, Jul. 2012.

[8] G. von Trentini, “Partially reflecting sheet arrays,” *IEEE Trans. Antennas Propagat*, vol. 4, pp. 666–671, Oct. 1956.

[9] A. P. Feresidis and J. C. Vardaxoglou, “High gain planar antenna using optimised partially reflective surfaces,” *IEE Proc. Microwave Antennas Propagat.*, vol. 148, pp. 345–350, Dec. 2001.

[10] C. Mateo-Segura, A. P. Feresidis and G. Goussetis, "Broadband leaky-wave antennas with double-layer PRS: analysis and design," *European Conf. on Antennas and Propagation (EuCAP)*, Apr. 11–15, 2011.

[11] F. Capolino and D. R. Jackson, "Directive Fabry-Pérot Cavity Leaky-Wave Antennas: History, Design and Theory," Short Course given at the IEEE AP-S Intl. Symp., Chicago, IL, Jul. 8–14, 2012.

[12] L. Moustafa and B. Jecko, "EBG structure with wide defect band for broadband cavity antenna applications," *IEEE AWPL*, vol. 7, pp. 693–696, Nov. 2008.

[13] Y. F. Lu and Y. C. Lin, "Design and implementation of broadband partially reflective surface antenna," *IEEE AP-S Intl. Symp.*, Spokane, WA, Jul. 3 - 8, 2011.

[14] A. P. Feresidis and J. C. Vardaxoglou, "A broadband high-gain resonant cavity antenna with single feed," *European Conf. on Antennas and Propagation (EuCAP)*, Nice, France, Nov. 6–10, 2006.

[15] Z. G. Liu, W. X. Zhang, D. L. Fu, Y. Gu and Z. C. Ge, "Broadband Fabry-Pérot resonator printed antennas using FSS superstrate with dissimilar size," *Microw. Opt. Technol. Lett.*, vol. 50, no. 6, pp. 1623–1627, Jun. 2008.

[16] C. Mateo-Segura, A. P. Feresidis and G. Goussetis, "Highly directive 2-D leaky wave antennas based on double meta-surfaces," *European Conf. on Antennas and Propagation (EuCAP)*, Barcelona, Spain, Apr. 12 –16, 2010.

[17] A. Foroozesh and L. Shafai, "Investigation into the effects of the reflection phase charactersitics of highly-reflective superstrates on resonant cavity antennas," *IEEE Trans. Antennas Propag.*, vol. 58, no. 10, pp. 3392–3396, Oct. 2010.

[18] M. A. Al-Tarifi, D. E. Anagnostou, A. K. Amert and K. W. Whites, "Multiple superstrates technique for a broadband cavity resonance antenna (CRA)," *IEEE AP-S Intl. Symposium*, Spokane, WA, Jul. 3–8, 2011.

[19] S. Wang, A. P. Feresidis, G. Goussetis and J. C. Vardaxoglou, "Low profile resonant cavity antenna with artificial magnetic conductor ground plane," *Electronics Letters*, vol. 40, pp. 405–506, Apr. 1, 2004.

[20] S. Wang, A. P. Feresidis, G. Goussetis and J. C. Vardaxoglou, "Artificial magnetic conductors for low-profile resonant cavity antennas," *IEEE AP-S Intl. Symposium*, Monterey, CA, USA, vol. 2, pp. 1423–1426, Jun. 20–25, 2004.

[21] A. P. Feresidis, G. Goussetis, S. Wang and Vardaxoglou, "Artificial magnetic conductor surfaces and their application to low-profile high-gain planar antennas," *IEEE Trans. Antennas Propag.*, vol. 53, no. 1, pp. 209–215, Jan. 2005.

[22] S. N. Burokur, R. Yahiaoui and A. de Lustrac, "Subwavelength resonant cavities fed by microstrip patch array," *IEEE Intl. Workshop on Antenna Technology*, Santa Monica, CA, USA, pp. 1–4, Mar. 2–4, 2009. .

[23] L. Zhou, H. Li, Y. Qin, Z. Wei and C. T. Chan, "Directive emissions from subwavelength metamaterial-based cavities," *IEEE Intl. Workshop on Antenna Technology*, pp. 191–194, Mar. 7–9, 2005.

[24] A. Ourir, A. de Lustrac and J.-M. Lourtioz, "All-metamaterial-based subwavelength cavities (λ/60) for ultrathin directive antennas," *Applied Physics Letters*, vol. 88, Feb. 2006.

[25] S. Wang, A. P. Feresidis, G. Goussetis and J. C. Vardaxoglou, "High gain subwavelength resonant cavity antennas based on metamaterial ground planes,"

IEE Proc. Microwaves, Antennas, and Propagation, vol. 53, no. 1, pp. 1–6, Feb. 2006.

[26] J. R. Kelly and A. P. Feresidis, “Low-profile high gain sub-wavelength resonant cavity antennas for wimax applications,” *European Conf. on Antennas and Propagation (EuCAP)*, Edinburgh, Scotland, U.K., Nov. 11–16, 2007.

[27] R. Yahiaoui, S. N. Burokur and A. d. Lustrac, “Enhanced directivity of ultra-thin metamaterial-based cavity antenna fed by multisource,” *Electronics Letters,* vol. 45, no. 16, pp. 814–816, Jul. 2009.

[28] Z. -G. Liu and R. Qiang, “Comparitive approach of Fabry-Pérot resonator antenna with PMC and PEC ground plane,” *IEEE AP-S Intl. Symposium,* Toronto, Ontario, Canada, Jul. 11–17, 2010.

[29] C. Mateo-Segura, G. Goussetis and A. P. Feresidis, "Sub-wavelength profile 2-D leaky-wave antennas with two periodic layers," *IEEE Trans. Antennas Propag.*, vol. 59, no. 2, pp. 416–424, Feb. 2011.

[30] J. Ju, D. Kim, W. Lee and J. Choi, “Low-profile Fabry-Pérot cavity antenna with a double-layered partially reflecting surface structure,” *Microwave and Optical Technology Letters,* vol. 53, no. 2, pp. 271–273, Feb. 2011.

[31] Y. Liu and X. Zhao, “High-gain ultrathin resonant cavity antenna,” *Microwave and Optical Technology Letters,* vol. 53, no. 9, pp. 1945–1949, Sep. 2011.

[32] A. Pirhadi, M. Hakkak, F. Keshmiri and R. K. Baee, “Design of compact dual band high directive electromagnetic bandgap (EBG) resonator antenna using artificial magnetic conductor,” *IEEE Trans. Antennas Propagat.*, vol. 55, no. 6, pp. 1682–1690, Jun. 2007.

[33] Z.-G. Liu and T. -H. Liu, “Comparative study of Fabry-Pérot resonator antenna with PMC and PEC ground plane,” *J. Progress in Electromagnetics Research B,* vol. 32, pp. 299–317, 2011.

[34] F. Costa and A. Monorchio, “Design of subwavelength tunable and steerable Fabry-Pérot/leaky wave antennas,” *J. Progress in Electromagnetics Research,* vol. 111, pp. 467–481, 2011.

[35] G. Lovat, P. Burghignoli and D. R. Jackson, “An investigation of directive radiation from ultra subwavelength-thick planar antennas with partially-reflecting surfaces,” *IEEE AP-S Intl. Symp.,* San Diego, CA, Jul. 5–12, 2008.

[36] J. Kelly, G. Passalacqua, A. P. Feresidis, F. Capolino, M. Albani and Y. C. Vardaxoglou, “Simulations and measurements of dual-band 2-D periodic leaky wave antenna,” in *Loughborough Antennas and Propagation Conf.*, Loughborough, England, pp. 293–286, Apr. 2–3, 2007.

[37] B. A. Zeb, Y. Ge, K. P. Esselle, Z. Sun and M. E. Tobar, “A simple dual-band electromagnetic band gap resonator antenna based on inverted reflection phase gradient,” *IEEE Trans. Antennas Propag.,* vol. 60, no. 10, pp. 4522–4529, Oct. 2012.

[38] D. Kim, “Novel dual-band Fabry-Perot cavity antenna with low-frequency separation ratio,” *Microwave and Optical Technology Letters,* vol. 51, no. 8, pp. 1869–1872, Aug. 2009.

[39] E. B. Lima, J. R. Costa and C. A. Fernandes, “FSS design for dual-band and low profile Fabry-Pérot antenna at Ka-band,” *European Conference on Antennas and Propagation (EuCAP),* The Hague, Netherlands, pp. 542–544, Apr. 6–11, 2014.

[40] Y. Ge and C. Wang, "A tri-band Fabry-Pérot cavity for antenna gain enhancement," *IEEE AP-S Intl. Symp.*, Orlando, FL, Jul. 7–12, 2013.

[41] B. A. Zeb, R. M. Hashmi, K. P. Esselle and Y. Ge, "The use of reflection and transmission models to design wideband and dual-band Fabry-Pérot cavity antennas," *Proc. URSI Intl. Symp. on Electromagnetic Theory*, Hiroshima, Japan, pp. 1084–1087, May 2013.

[42] G.-N. Tan, X.-X. Y. and B. Han, "A dual-polarized Fabry-Pérot cavity antenna at millimeter wave band with high gain," *IEEE 4th Asia-Pacific Conference on Antennas and Propagat.*, Kuta, Indonesia, pp. 621–622, Jun. 30–Jul. 3, 2015.

[43] B. A. Zeb, Y. Ge and K. P. Esselle, "A single-layer thin partially reflecting surface for tri-band directivity enhancement," *Asia Pacific Microwave Conference*, Kaohsiung, Taiwan, pp. 559–561, Dec. 4–7, 2012.

[44] P. Burghignoli, G. Lovat, F. Capolino, D. R. Jackson and D. R. Wilton, "Highly polarized, directive radiation from a Fabry-Pérot cavity leaky-wave antenna based on a metal strip grating," *IEEE Trans. Antennas Propag.*, vol. 58, no. 12, pp. 3873–3883, Dec. 2010.

[45] T. Zhao, *Analysis and Design of 2-D Periodic Leaky Wave Antennas using Metal Patches or Slots*, Ph.D. dissertation, University of Houston, 2003.

[46] D. R. Jackson and N. G. Alexópoulos, "Gain enhancement methods for printed circuit antennas," *IEEE Trans. Antennas Propag*., vol. 33, no. 9, pp. 976–987, Sep. 1985.

[47] H. D. Yang and N. G. Alexópoulos, “Gain enhancement methods for printed circuit antennas through multiple superstrates,” *IEEE Trans. Antennas Propag*., vol. 35, no. 7, pp. 860–863, Jul. 1987.

[48] R. Sauleau, P. Coquet, T. Matsui, and J.-P. Dan, “A new concept of focusing antennas using plane parallel Fabry-Pérot cavities with nonuniform mirrors,” *IEEE Trans. Antennas Propag*., vol. 51, no. 11, pp. 3171–3175, Nov. 2003.

[49] N. Guérin, S. Enoch, G. Tayeb, P. Sabouroux, P. Vincent, and H. Legay, “A metallic Fabry-Pérot directive antenna,” *IEEE Trans. Antennas Propag*., vol. 54, no. 1, pp. 220–224, Jan. 2006.

[50] T. Zhao, D. R. Jackson, J. T. Williams, Hung-Yu D. Yang, and A. A. Oliner, “2-D periodic leaky-wave antennas-part I: metal patch design,” *IEEE Trans. Antennas Propag*., vol. 53, no. 11, pp. 3505–3514, Nov. 2005.

[51] D. R. Jackson, P. Burghignoli, G. Lovat, F. Capolino, J. Chen, D. R. Wilton, and A. A. Oliner, “The fundamental physics of directive beaming at microwave and optical frequencies and the role of leaky waves,” *Proceedings of the IEEE on Metamaterials and Applications in the Microwave to Optical Regime*, G. V. Eleftheriades, Editor, vol. 99, no. 10, pp. 1780–1805, Oct. 2011.

[52] D. R. Jackson and N. G. Alexopoulos, “Gain enhancement methods for printed circuit antennas,” *IEEE Trans. on Antennas and Propagat.*, vol. 33, no. 9, pp. 976–987, Sep. 1985.

[53] F. J. Zucker, “Surface-Wave Antennas,” Chapter 10 of *Antenna Engineering Handbook*, Ed.; R. C. Johnson, McGraw-Hill, 2007.

Appendix

A.1 Spectral-domain Green's Function $\tilde{G}_{xx}$

The spectral-domain immitance (SDI) method is used to obtain the Green's function for the electric field in the x direction due to a periodic current in the x direction [50]. The TEN model for the single cavity structure is shown in Figure A.1.

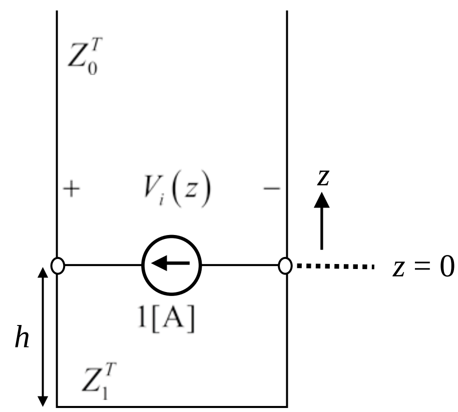

Figure A.1. The TEN model used to calculate the spectral-domain Green's function $\tilde{G}_{xx}$.

The Green's function $\tilde{G}_{xx}$ for $z = 0$ is given as

$$\tilde{G}_{xx}\left(k_x, k_y, 0\right) = -\frac{1}{k_t^2}\left[k_x^2 V_i^{TM}\left(0\right) + k_y^2 V_i^{TE}\left(0\right)\right], \tag{A.1}$$

where at $z = 0$, the voltage due to a 1 [A] parallel current is

$$\begin{aligned} V_i^T\left(0\right) = Z_{in} &= Y_{in}^{-} \\ &= \left(Y_{in}^{+} + Y_{in}^{-}\right)^{-1} \\ &= \left[Y_0^T - jY_1^T \cot\left(k_{z1}h\right)\right]^{-1}. \end{aligned} \tag{A.2}$$

Here T denotes either TM or TE polarization. The characteristic admittances for the two regions are

$$Y_0^{TM} = \frac{\omega\varepsilon_0}{k_{z0}}, \tag{A.3}$$

$$Y_0^{TE} = \frac{k_{z0}}{\omega\mu_0}, \tag{A.4}$$

$$Y_1^{TM} = \frac{\omega\varepsilon_1}{k_{z1}}, \tag{A.5}$$

and

$$Y_1^{TE} = \frac{k_{z1}}{\omega\mu_1}, \tag{A.6}$$

where

$$k_{z0} = \left(k_0^2 - k_x^2 - k_y^2\right)^{1/2} \tag{A.7}$$

and

$$k_{z1} = \left(k_1^2 - k_x^2 - k_y^2\right)^{1/2}. \tag{A.8}$$

In order to calculate $\tilde{G}_{xx}\left(k_{xp}, k_{yq}, -h_d\right)$, the voltage must be translated to the location of the source dipole. Let us consider the dipole to be at a distance h_d from the 1 [A] current source as shown in Figure A.2.

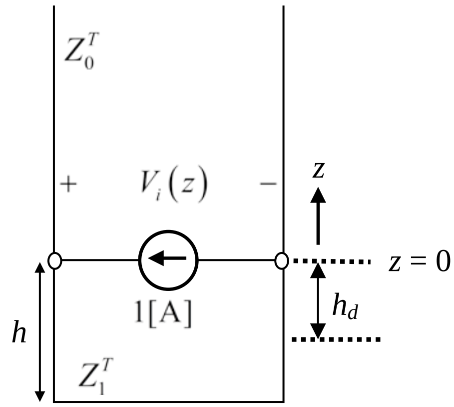

Figure A.2. The TEN model used to calculate the spectral-domain Green's function $\tilde{G}_{xx}\left(k_{xp}, k_{yq}, -h_d\right)$.

The voltage at the dipole is given as

$$V_i^T\left(-h_d\right) = V_i^T\left(0\right)\frac{\sin\left(k_{z1}\left(h-h_d\right)\right)}{\sin\left(k_{z1}h\right)}. \tag{A.9}$$

With this voltage, we may find $\tilde{G}_{xx}\left(k_{xp}, k_{yq}, -h_d\right)$.

A.2 Spectral-domain Green's Function $\tilde{G}_{xx}$ for the Single Cavity Substrate-Board Case

The spectral-domain Green's function for the substrate-board case of Chapter 2 is derived here. We first consider the PRS case (a) where the PRS layer is on the top surface of the substrate board. The TEN model for the PRS case is shown in Figure A.3.

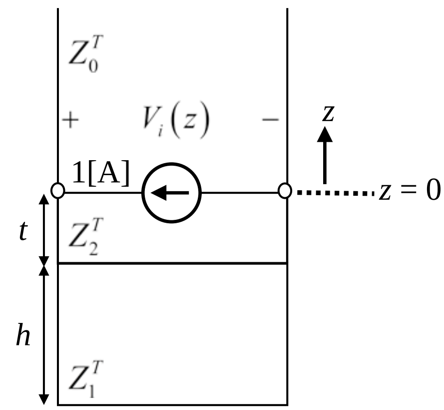

Figure A.3. The TEN model used to calculate the spectral-domain Green's function $\tilde{G}_{xx}$ for the PRS case (a).

The Green's function for this case is as again given by Equation (A.1). The voltage due to the 1 [A] current source is

$$\begin{aligned} V_i^T(0) &= Z_{in} = Y_{in}^{-1} \\ &= \left(Y_{in}^{+} + Y_{in}^{-}\right)^{-1}, \end{aligned} \tag{A.10}$$

where

$$Y_{in}^{+} = Y_0^T \tag{A.11}$$

and

$$Y_{in}^{-} = Y_2^T \left[\frac{-jY_1^T \cot(k_{z1}h) + jY_2^T \tan(k_{z2}t)}{Y_2^T + Y_1^T \cot(k_{z1}h)\tan(k_{z2}t)} \right]. \tag{A.12}$$

The characteristic impedances are given in Equations (A.3) to (A.6). Hence, from Equation (A.1) and Equations (A.10) to (A.12), we may find the spectral-domain Green's function for the PRS case (a).

Let us now consider the PRS case (b) where the PRS layer is placed on the bottom surface of the substrate board. The TEN model for this case is shown in Figure A.4.

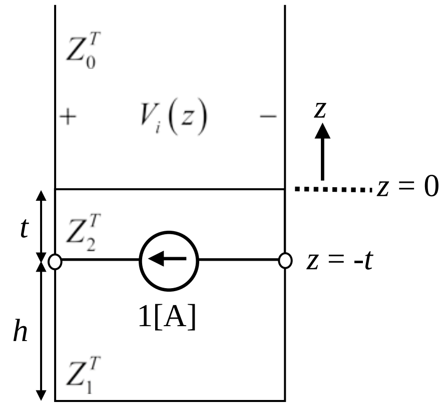

Figure A.4. The TEN model used to calculate the spectral-domain Green's function $\tilde{G}_{xx}$ for the PRS case (b).

It is observed that the 1 [A] current source is now placed at $z=-t$ and the voltage at $z=-t$ due to the current source is given as

$$\begin{aligned} V_i^T(-t) &= Z_{in} = Y_{in}^{-1} \\ &= \left(Y_{in}^{+} + Y_{in}^{-}\right)^{-1}, \end{aligned} \tag{A.13}$$

where

$$Y_{in}^{+} = Y_2^T \left[\frac{Y_0^T + jY_2^T \tan\left(k_{z2}t\right)}{Y_2^T + jY_0^T \tan\left(k_{z2}t\right)} \right] \tag{A.14}$$

and

$$Y_{in}^{-} = -jY_1^T \cot\left(k_{z1}h\right). \tag{A.15}$$

Hence, by substituting Equation (A.13) into Equation (A.1), we may find the spectral-domain Green's function for the PRS case (b).

We may generalize the Green's function for the substrate-board case as follows. If we consider the embedding distance of the periodic patch layer to be t_p, such that for the

PRS case (a) $t_p = 0$ and for the PRS case (b) $t_p = t$, then the generalized form of the Green's function for the substrate board case is given as

$$\tilde{G}_{xx}\left(k_{xp}, k_{yq}, -t_p\right) = -\frac{1}{k_t^2}\left[k_x^2 V_i^{TM}\left(-t_p\right) + k_y^2 V_i^{TE}\left(-t_p\right)\right]. \tag{A.16}$$

The generalized form of the voltage is given as

$$V_i^T\left(-t_p\right) = \left(Y_{in}^+\left(t_p\right) + Y_{in}^-\left(t_p\right)\right)^{-1}. \tag{A.17}$$

Here,

$$Y_{in}^+\left(-t_p\right) = Y_2^T\left[\frac{Y_0^T + jY_2^T \tan\left(k_{z2}t_p\right)}{Y_2^T + jY_0^T \tan\left(k_{z2}t_p\right)}\right] \tag{A.18}$$

and

$$Y_{in}^-\left(-t_p\right) = Y_2^T\left[\frac{-jY_1^T \cot\left(k_{z1}h\right) + jY_2^T \tan\left(k_{z2}\left(t - t_p\right)\right)}{Y_2^T + Y_1^T \cot\left(k_{z1}h\right)\tan\left(k_{z2}\left(t - t_p\right)\right)}\right]. \tag{A.19}$$

Again, to find $\tilde{G}_{xx}\left(k_{xp}, k_{yq}, -h_d\right)$, the voltage at the dipole location must be calculated. If we consider the dipole to be located at a distance h_d below the bottom surface of the substrate board, then the voltage at the dipole location in terms of the embedding distance t_p is

$$V_i^T\left(-h_d\right) = \frac{V_i^T\left(-t_p\right)\left(1 + \Gamma_L\right)}{e^{jk_{z2}\left(t - t_p\right)} + \Gamma_L e^{-jk_{z2}\left(t - t_p\right)}} \frac{\sin\left(k_{z1}\left(h - h_d\right)\right)}{\sin\left(k_{z1}h\right)}. \tag{A.20}$$

From Equation (A.20), we may find $\tilde{G}_{xx}\left(k_{xp}, k_{yq}, -h_d\right)$.

A.3 Calculation of the Shunt Susceptances Modeling the PRS and FSS Layers

Let us first consider the PRS case (a) where the PRS layer is placed on the top surface of the substrate board. The TEN model for this single cavity substrate-board case is shown in Figure A.5.

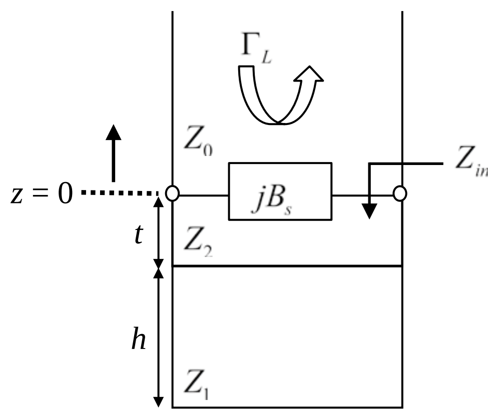

Figure A.5. The TEN model for the single cavity substrate-board PRS case (a).

From Figure A.5, we see that the net load impedance Z_L at $z = 0$ seen from above looking down is the parallel combination of the shunt load jB_s and the input impedance Z_{in}, and is given by

$$Z_L = \frac{1}{jB_s + Y_{in}}, \tag{A.21}$$

where

$$Z_{in} = \frac{1}{Y_{in}} = Z_2 \left[\frac{jZ_1 \tan(k_{z1}h) + jZ_2 \tan(k_{z2}t)}{Z_2 - Z_1 \tan(k_{z1}h)\tan(k_{z2}t)} \right]. \tag{A.22}$$

The voltage at $z=0$ due to an incident plane wave, where voltage models E_x for the (0,0) Floquet wave, is given by

$$V(0)=E_x^{inc}\left(1+\Gamma\right)+\frac{1}{ab}\sum_{n=1}^{N}A_n\tilde{G}_{xx}\left(k_{x0},k_{y0},0\right)\tilde{B}_n\left(k_{x0},k_{y0}\right)e^{-j\left(k_{x0}x+k_{y0}y\right)} \quad . \text{(A.23)}$$

The layer reflection coefficient Γ of the above equation is provided in Equation (2.30) of Chapter 2 and is calculated for broadside incidence. Once $V\left(0\right)$ is computed, we may relate it to the reflection coefficient Γ_L of Figure A.5. Assuming the incident voltage (E_x field) is unity, we have

$$V\left(0\right)=1+\Gamma_L \quad . \qquad \text{(A.24)}$$

Once Γ_L is obtained, we may relate it to the net load impedance Z_L as

$$Z_L=Z_0\left(\frac{1+\Gamma_L}{1-\Gamma_L}\right). \qquad \text{(A.25)}$$

Substituting Equation (A.21) into Equation (A.25), the shunt susceptance B_s is found to be

$$B_s=-jY_0\left(\frac{1-\Gamma_L}{1+\Gamma_L}\right)+jY_{in}\,. \qquad \text{(A.26)}$$

In order to calculate the shunt susceptance modeling the periodic patch array in PRS case (b), let us consider the TEN model of Figure A.6.

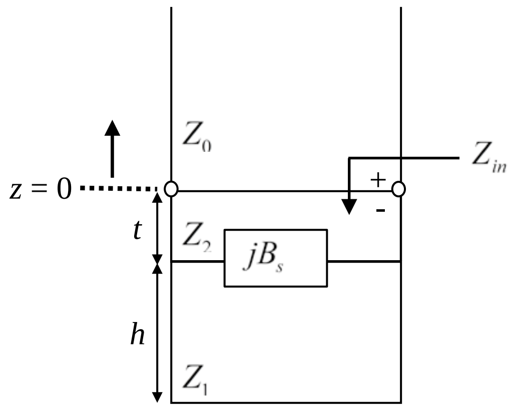

Figure A.6. The TEN model for the single cavity substrate-board PRS case (b).

The voltage $V(0)$ at $z = 0$ is again in the form of Equation (A.23), and again voltage represents the E_x field of the (0,0) Floquet mode. From this voltage, and taking the incidence voltage $V_{inc} = 1\,[\mathrm{V}]$, we may calculate the reflection coefficient Γ^+ at $z = 0^+$ from

$$V(0) = 1 + \Gamma^+ . \tag{A.27}$$

Once Γ^+ is calculated, the net load impedance Z_L at $z = 0$ may be calculated as

$$Z_L = Z_0 \left[\frac{1+\Gamma^+}{1-\Gamma^+} \right]. \tag{A.28}$$

Since impedance is continuous, the net load impedance Z_L is equal to the input impedance Z_{in} as shown in Figure A.6. Knowing Z_{in}, we may calculate the reflection coefficient Γ^- at $z = 0^-$ as

$$\Gamma^- = \frac{Z_{in} - Z_2}{Z_{in} + Z_2} . \tag{A.29}$$

Once Γ^- is calculated, we may relate it to the load reflection coefficient Γ_{L1} just above the shunt susceptances at $z = -t^-$ as

$$\Gamma^- = \Gamma_{L1} e^{-j2k_{z2}t} \ . \tag{A.30}$$

Once Γ_{L1} is calculated, we may find the net load impedance Z_{L1} at $z = -t^-$ as

$$Z_{L1} = Z_2 \left[\frac{1+\Gamma_{L1}}{1-\Gamma_{L1}} \right]. \tag{A.31}$$

It may be seen that Z_{L1} is in the form

$$Z_{L1} = \frac{1}{jB_s - jY_1 \cot\left(k_{z1}h\right)}. \tag{A.32}$$

Substituting Equation (A.32) into Equation (A.31), we find the shunt susceptance B_s to be

$$B_s = -j \left[\frac{1-\Gamma_{L1}}{1+\Gamma_{L1}} \right] Y_2 + Y_1 \cot\left(k_{z1}h\right) \ . \tag{A.33}$$